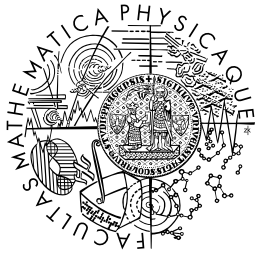

FACULTY
OF MATHEMATICS
AND PHYSICS
Charles University

DOCTORAL THESIS

RNDr. Lukáš Beran

Optical and magneto-optical studies of ferrimagnetic garnets for photonic and spintronic applications

Intitute of Physics of Charles University

Supervisor of the doctoral thesis:	RNDr. Martin Veis, PhD.
Study programme:	Physics
Study branch:	Quantum Optics and Optoelectronics

Prague 2020

I declare that I carried out this doctoral thesis independently, and only with the cited sources, literature and other professional sources.

I understand that my work relates to the rights and obligations under the Act No. 121/2000 Sb., the Copyright Act, as amended, in particular the fact that the Charles University has the right to conclude a license agreement on the use of this work as a school work pursuant to Section 60 subsection 1 of the Copyright Act.

In ..... date ..... signature of the author

First and foremost I would like to thank to my wife Lucy, who stood by my site despite all the aspects of living with Physicist, and chose to rise our son with be, even though he might one day follow my footsteps and choose the same field of study.

I also cannot forget all the students, friends and colleagues from Institute of Physics of Charles University as well as DMSE at MIT. They not only made this work possible through their help and hard work, but I would most likely left academia years ago if there was not for their friendship and support.

Many thanks go to prof. C. A. Ross who took me under her wings during my stays at MIT. It was a privilege to work under her guidance and it was her, thanks to whom I never felt homesick even while being so far away.

At last, but not least, I would like to thank my supervisor Martin Veis, who took the whole journey starting with my first days at Charles University with me. Even though we have been together though good times as well as the bad ones, he was always the one I knew I could ask for help or advice.

There are many others, who would deserve to be named, and those all I would like to thank for being part of my life.

Název práce: Studie optických a magnetooptických vlastností ferrimagnetických granátů pro fotonické a spintronické aplikace

Autor: RNDr. Lukáš Beran

Katedra: Fyzikální ústav Univerzity Karlovy

Vedoucí disertační práce: RNDr. Martin Veis, PhD., Fyzikální ústav Univerzity Karlovy

Abstrakt: Tato doktorská práce se věnuje přípravě a systematické charakterizaci fyzikálních vlastností tenkých vrstev železitých granátů s potenciálním využitím ve fotonických a spintronických zařízeních. Zkoumané vzorky byly připraveny pomocí metalo-organické dekompozice a pulzní laserové depozice. Studie se zaměřila na strukturní a magnetickou charakterizaci spolu s optickými a magnetooptickými vlastnostmi. Získané experimentální výsledky byly dále srovnány s teoretickými výpočty. Aplikační potenciál granátů pro fotonická zařízení byly diskutovány na základě určeného faktoru jakosti (Figure of Merit). Vysoké hodnoty byly dosaženy pro monokrystalácké filmy Ce dopovaného yttritého železitého granátu a polykrystalické vrstvy Bi dopovaného yttritého železitého granátu na křemíkovém substrátu. Dále byly připraveny vrstvy nových granátů vzácných zemin se snahou dosáhnout kolmé magnetické anizotropie. To se podařilo pro tři různé materiály, které doposud nebyly zkoumány ve formě tenkého filmu. Teplotní závislost fyzikálních vlasntostí vybraných granátů byla zkoumána v rozsahu od 15 do 340 K. Tato měření odhalila změnu magnetické aniziotropie při nízkých teplotách a blíže zkoumala magnetooptickou odezvu v blízkosti kompenzační teploty. Závěrem bylo provedeno teoretické modelování magnetooptické odezvy s cílem vysvětlit její mikroskopický původ a oddělit příspěvky jednotlivých magnetických podmříží.

Klíčová slova: Ferrimagnetický granát Magnetooptická spektroskopie Pulzní laserová depozice Tenké vrstvy Metalo-organická dekompozice

Title: Optical and magneto-optical studies of ferrimagnetic garnets for photonic and spintronic applications

Author: RNDr. Lukáš Beran

Department: Intitute of Physics of Charles University

Supervisor: RNDr. Martin Veis, PhD., Institute of Physics of Charles University

Abstract: This doctoral thesis is devoted to fabrication and systematic characterization of physical properties of thin films of iron garnets with potential applications in photonic and spintronic devices. Investigated samples were prepared by metallo-organic decomposition and pulsed laser deposition. The study was focused on structural and magnetic characterizaiton along with optical and magneto-optical properties. Obtained experimental results were further confronted with theoretical calculations. The application potencial of garnets for photonic devices was discussed based on determined Figure of Merit (Faraday rotation to optical loss ratio). High values were achieved for single crystal thin film of Ce doped yttrium iron garnet on galium gadolinium garnet substrate as well as for pollycrystalline Bi doped yttrium iron garned on silicon substrate. Furthermore, new rare-earth garnets were prepared with attempt to achieve perpendicular magnetic anisotropy of these film. This was achieved for three different materials, which were not studied in the form of thin films before. Temperature denepndence of pyhysical properties of selected garnets were probed in region from 15 to 340 K. These measurements revealed changes of mangetic anisotropy at low temperatures and further studied magneto-optical response in the vicinity of the compensation temperature. Finally, theoretical modeling of magneto-optical response was performed to explain its microscopic origin and separate the contribution of individual magnetic sublattices.

Keywords: Ferrimagnetic garnets Magneto-optical spectroscopy Pulsed laser deposition Thin films Metallo-organic decomposition

Contents

Part I

Introduction

On daily bases we are witnesses of marvels that modern research and engineering bring to our lives. One of the most progressing fields is definitely consumer electronics. Due to its rapid progress, both science world and industry, call for new, better, faster and more reliable devices. Even though conventional electronics managed to satisfy their demands for many decades, there are reports it is reaching its physical limits and the device performance cannot be improved any further [1]. Therefore, other fields like spintronics or photonics are getting more attention. Novel spintronic approaches demonstrated the ability to overcome the limits of classical electronics by using different physical phenomena resulting in faster and more energy efficient devices [2].

Spintronics aims to use the spins of electrons as carriers of information to avoid Joule's heat caused by Ohmic losses and target higher operational frequencies due to fast spin dynamics. Already reported functional devices such as Spin Hall Effect Transistor [3] could one day replace their conventional counterparts. It also introduced concepts, that are already industrial standards. One of the examples is usage of giant magnetoresistance phenomenon [4] which led to an increase in data storage capacity by more than one order of magnitude.

Photonics on the other hand tries to use completely different physical concept by utilizing light [5]. Information is converted into light pulses that are carried around via optical fibers. Similarly modern computers also starts to use optical communication to speed up data transfer between peripheral components [6] (Fig. 1). The next step is performing of logical operations directly on these optical signals. Carrying such operations solely in the optical domain would lead to great improvement of communication networks, because conversion of signal for processing are both, time and energy consuming. The present state of research is very far from full optical computing, but there are many smaller tasks, that would bring great benefits. For example, telecommunication networks require simple operations as multiplexing, packet synchronization or address recognition.

Material engineering has already demonstrated the possibility to fabricate integrated photonic logic gates [7]. These devices based on interference of optical signals are possible due to progress in on-chip integration of optical filters, resonators and modulators. They exhibit excellent performance as standalone devices; however, their integration into more complex devices is very problematic. It is due to the back reflections on each optical element in the system that disrupts the interference process in the gates. One of the ways to overcome this problem is usage of magneto-optical isolators based on nonreciprocal propagation.

Optical isolator is a component widely used in laser industry. Its purpose is to prevent the propagation of light in backward direction. Table-top lasers usually work with beam diameters ranging from millimeters to centimeters. Therefore, commercially available devices are based on bulk magneto-optical crystals of similar dimensions. The basic concept of such devices utilizes polarization filtering and its rotation as schematically shown in Fig. 2. The proper functionality of the device requires a nonreciprocal propagation in the rotator. Therefore, optically anisotropic media, commonly used for light polarization control, cannot be used for the construction of optically isolating device and magneto-optical rotators are used.

The first element of the magneto-optical isolator is a polarizer. In the case of unpolarized light, arbitrary orientation can be chosen, but otherwise it is set to

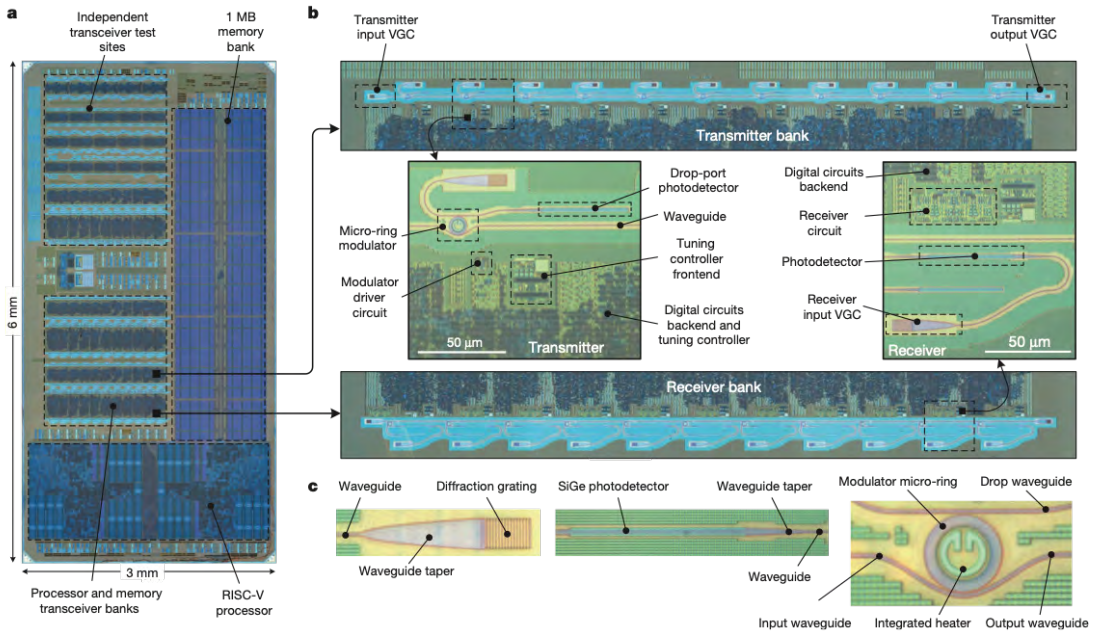

Figure 1: Schematic of single-chip microprocessor with components communicating between them through optical signal [6].

match the polarization of the source. In further description is polarization passed through this polarizer considered along x axis. The next element of isolator is magneto-optical rotator that changes the angle of polarization plane by 45 degrees in clockwise direction. The polarizer at the output is set to mach this plane and therefore the light is passed through. The light coming from the other direction has to pass through the output polarizer. Therefore, the light on the right side of the rotator is linearly polarized at 45 degrees from x axis. The light propagating through the rotator in backward direction sees the present magnetic field in opposite direction and therefore, the induced rotation is anti-clockwise. This results with its polarization plane along the y axis and it is not passed through the polarizer at the input.

Integration of such device on photonic chip has been found difficult. Usage of the concept described above is unfeasible, because coupling light into magneto-

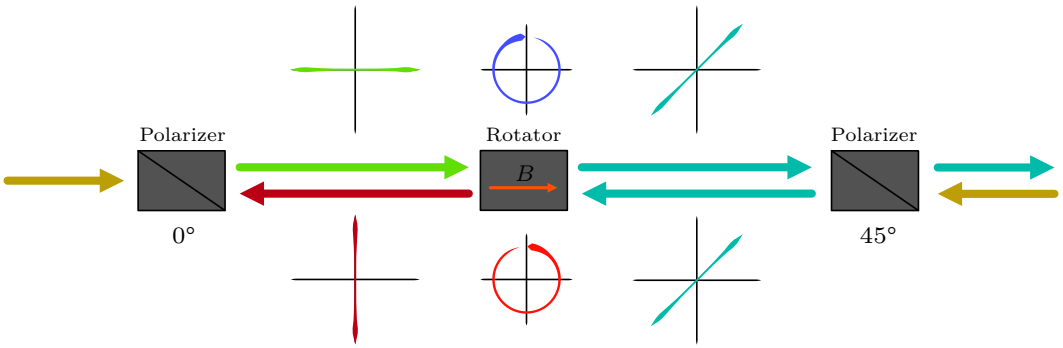

Figure 2: Schematic of optical isolator based on two prisms and magneto-optical rotator. The top shows polarization states of light propagating to the right. The polarization states of light propagating to the left are shown at the bottom.

Figure 3: Picture of Andradite ($Ca_3Fe_2Si_3O_{12}$), garnet commonly used in jewelry [8].

optical medium from a waveguide is not as simple and effective as with light in free space. Furthermore, classical materials used for optical isolator (quartz, garnets) are hard to prepare on silicon substrate. That often leads to fabrication of a material without sufficient magneto-optical response for a working device. Therefore, it is vital for the future development in this field to seek new materials and deposition techniques that would provide reliable and efficient optical isolators.

This thesis covers several materials from class of iron garnets. Garnets are vastly large group of materials with general formula of $X_3Y_2Z_3O_{12}$, where X, Y, Z can be chosen from substantial palette of elements. Garnets found in the nature are mostly silicon based. They are commonly used in jewelry due to their nice color and significant hardness. Typical representative used for such purposes is Andradite (Fig. 3). The material with Y and Z sites occupied by iron is called iron garnet. Since magnetic moments of these two sublattices align anti-parallelly, the resulting material is in character ferrimagnetic. The well known representative is yttrium iron garnet ($Y_3Fe_5O_{12}$) (YIG). This material is one of the most examined magnetic systems, but even though it is known for a long time, its application is still very common. The first reason is the perfection of its manufacturing process. The second are its unique magnetic properties. It is a material with the narrowest known ferromagnetic resonance line as well as the lowest Gilbert damping. These attributes make it very favorable material in microwave and spintronic applications. Furthermore, due to its dielectric character, it has very low optical absorption up to 3 eV. Moreover, introduction of rare earth element into YIG lattice was found to modify its structural, magnetic and magneto-optical properties even further. Nowadays, Bi and Ce doped YIG are well established magneto-optical materials, but their preparation in the form of thin films is still very extensive field of engineering.

The thesis is organized into five part. The first part contain the general motivation and structure of the thesis. Following theoretical background covers description of light, matter and their interaction. It introduces terms and mathematical apparatus used further in the thesis. The third part describes used experimental methods. It starts with deposition techniques used for preparation of studied samples. Afterwards, it covers methods used for their characterization.

This includes X-ray diffraction (XRD), magnetometry, spectroscopic ellipsometry and magneto-optical spectroscopy. The main focus is given to the optical techniques as they present the main experimental apparatus used throughout this thesis. The main fourth part contains the results of the thesis. Its four chapters correspond to different motivations behind the study of garnet systems. The chapter focusing on Figure of Merit of Ce and Bi doped YIG is devoted to perfection of theses materials for its applications as magneto-optical medium in optical isolators. Following chapter demonstrates the tuning of magnetic anisotropy of thin films of rare-earth (RE) garnets that is an important property for many spintronic applications. The third chapter focuses on temperature dependence of physical properties of chosen garnets. The last chapter describes modeling of magneto-optical response of $Tb_3Fe_5O_{12}$ using microscopic model based on semi-classical approach. The resulting model is used for study of magnetic sublattices present in the garnet structure. The final part contains summary of presented results and their conclusions.

Part II

Theoretical background

This thesis focuses on optical and magneto-optical properties of ferrimagnetic garnets and therefore techniques using light as a probe tool are widely used. There are two ways to approach the description of light, as a wave or as a particle. Spectroscopic methods used throughout this work focus on the visible part of electromagnetic spectra with some exceed to near infrared (IR) and ultraviolet (UV) and therefore it is sufficient to adopt the wave picture. The classical field theory based on Maxwell's equations allows description of light as an electromagnetic wave as well as its interaction with solid matter. This part summarizes the fundamentals of electromagnetic theory forming the necessary basis for this work. Since it contains only basics it is advised to seek further details in books like [9, 10].

1. Description of light

1.1 Wave equation

The beginning of approach to light as an electromagnetic wave was established by James Clerk Maxwell in 1873 with Maxwell's equations. To avoid the singular character of charges and their associated current, macroscopic electrodynamics uses charge densities ρ and current densities $\vec{j}$. Using SI units and the differential form, macroscopic Maxwell's equations are

$$\nabla \times \vec{E} = -\frac{\partial \vec{B}}{\partial t}, \tag{1.1}$$

$$\nabla \times \vec{H} = \frac{\partial \vec{D}}{\partial t} + \vec{j}, \tag{1.2}$$

$$\nabla \cdot \vec{D} = \rho, \tag{1.3}$$

$$\nabla \cdot \vec{B} = 0, \tag{1.4}$$

where $\vec{D}$ denotes the electric displacement, $\vec{E}$ the electric field, $\vec{H}$ the magnetic field, $\vec{B}$ the magnetic induction, ρ the electric charge density and $\vec{j}$ the current density. This set of equations without further constrains contains 16 unknowns. Considering symmetry of studied system, this number can be greatly reduced. In the case of linear, isotropic, homogenous and source-free media, the electromagnetic field is entirely defined by two scalar fields. Since this work focuses on magneto-optical effects, that break the symmetry of such system, this reduction of unknowns cannot be used.

The electromagnetic properties of a medium are described by macroscopic polarization $\vec{P}$ and magnetization $\vec{M}$ through relations

$$\vec{D} = \varepsilon_0 \vec{E} + \vec{P}, \tag{1.5}$$

$$\vec{H} = \mu_0^{-1} \vec{B} - \vec{M}, \tag{1.6}$$

where ε_0 and μ_0 denotes the permittivity and the permeability of vacuum, respectively. These equation do not introduce any conditions on the medium and therefore they are always valid.

Inserting equations 1.5 and 1.6 into Maxwell's equations and their further combination yields the inhomogeneous wave equations

$$\nabla \times \nabla \times \vec{E} + \frac{1}{c_0^2} \frac{\partial^2 \vec{E}}{\partial t^2} = -\mu_0 \frac{\partial}{\partial t} \left(\vec{j} + \frac{\partial \vec{P}}{\partial t} + \nabla \times \vec{M} \right), \tag{1.7}$$

$$\nabla \times \nabla \times \vec{H} + \frac{1}{c^2} \frac{\partial^2 \vec{H}}{\partial t^2} = \nabla \times \vec{j} + \nabla \times \frac{\partial \vec{P}}{\partial t} + \mu_0 \frac{\partial \vec{M}}{\partial t}. \tag{1.8}$$

From analogy with general form of wave equation, term $(\varepsilon_0 \mu_0)^{-1/2}$ was replaced with constant c_0 that is known to be speed of light in vacuum.

Maxwell's equations describe the electromagnetic fields that are generated by currents and charges in matter without further explanation of their origin. Therefore, they must be supplemented by relations that describe the response of

matter to the fields. These relations are introduced via tensor quantities in the form

$$\vec{D} = \varepsilon_0 \hat{\varepsilon} \vec{E}, \tag{1.9}$$

$$\vec{B} = \mu_0 \hat{\mu} \vec{H}, \tag{1.10}$$

$$\vec{j_c} = \sigma \vec{E}, \tag{1.11}$$

where $\hat{\varepsilon}$ in the permittivity tensor, $\hat{\mu}$ the permeability tensor, and $\vec{j_c}$ denotes conduction current density, making the last equation equivalent to Ohm's law. It is further convenient to work with total current density

$$\vec{j_t} = \vec{j_s} + \vec{j_c} + \frac{\partial \vec{P}}{\partial t} + \nabla \times \vec{M}. \tag{1.12}$$

The current density $\vec{j}$ was split into source current density $\vec{j_s}$ and conduction current density $\vec{j_c}$. The other two terms are recognized as the polarization current density and the magnetization current density, respectively. Since the materials presented in this work are dielectric, ρ and $\vec{j_c}$ are considered zero, which further simplify the solution. Using new notation with material relations reduces the wave equation 1.7 to

$$\left(\nabla^2 - \frac{1}{c^2} \frac{\partial^2}{\partial t^2} \right) \vec{E} = 0, \tag{1.13}$$

where c denotes the speed of light in the medium

$$|\vec{c}|^2 = \frac{1}{\hat{\mu}\hat{\varepsilon}} \approx \frac{1}{\hat{\varepsilon_r} \varepsilon_0 \mu_0}. \tag{1.14}$$

Last approximation assumes $\hat{\mu} = \mu_0$, that can be used for the photon energies of visible light. Similar derivation can be done for equation 1.8.

As a solution of 1.13, an electromagnetic field can be written in a form of a superpositions of monochromatic fields in the form

$$\vec{E} = \vec{E_0} \exp\left\{ i(\omega t - \vec{k} \cdot \vec{r}) \right\}, \tag{1.15}$$

where $\vec{E_0}$ is the amplitude, ω the angular frequency, t the time, $\vec{r}$ the position vector, and $\vec{k}$ the wave vector. Wave vector $\vec{k}$ is defined as

$$\vec{k} = \vec{s} \cdot \frac{\omega}{c}, \tag{1.16}$$

where $\vec{s}$ is unit vector in direction of propagation of the wave. Notation is further simplified with the introduction of refractive index through definition

$$n = \frac{c_0}{c}. \tag{1.17}$$

To utilize this notation, the wave vector in vacuum is defined as follows

$$k_0 = \vec{s} \cdot \frac{\omega}{c_0}. \tag{1.18}$$

Inserting the new notation into the solution 1.15 provides the commonly used form

$$\vec{E} = \vec{E_0} \exp\left\{ i \left(\omega t - n\vec{k_0} \cdot \vec{r} \right) \right\} \tag{1.19}$$

Applying of this solution on Maxwell's equations yields relations

$$\vec{k} \cdot \vec{E} = 0, \tag{1.20}$$

$$\vec{k} \cdot \vec{B} = 0, \tag{1.21}$$

$$\vec{s} \times \vec{E} = c\vec{B}. \tag{1.22}$$

This set of equations shows that vectors $\vec{s}$, $\vec{E}$ and $\vec{B}$ form orthogonal system. Therefore, any electromagnetic wave is always transversal. The third equation also provides the relation

$$\vec{E_0} = c\vec{B_0}, \tag{1.23}$$

binding the amplitudes of the electric and the magnetic part of the wave. Schematic of an electromagnetic wave propagating through space is depicted in Fig. 1.1. In this scenario the wave comes from the medium with refractive index of n_1 to the more optically dense of n_2. Therefore, one can notice the change of spacing between planes of the same phase indicating different propagation speed.

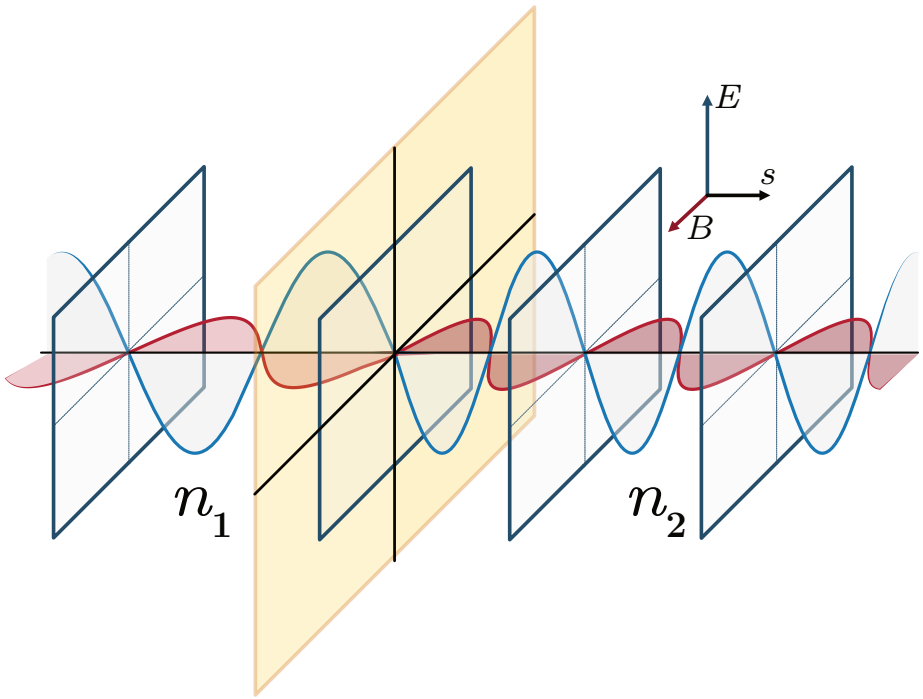

Figure 1.1: Linearly polarized harmonic wave propagating through two media of different refractive indexes.

1.2 Polarization

Polarization is an intrinsic property of every vectorial wave. It describes the geometrical orientation of the oscillation. It carries information about the direction

of vector $\vec{E}$ (or $\vec{B}$) while propagating through the system. Without prejudice to generality, we will focus on electromagnetic waves described by solution 1.19 propagating along z axis. As the wave propagates through system, the end point of the vector of electric intensity periodically follows a simple trajectory. The projection of this trajectory on a plane perpendicular to the direction of propagation is in the most general case an ellipse. This fact can be mathematically derived as stated in Ref. [11].

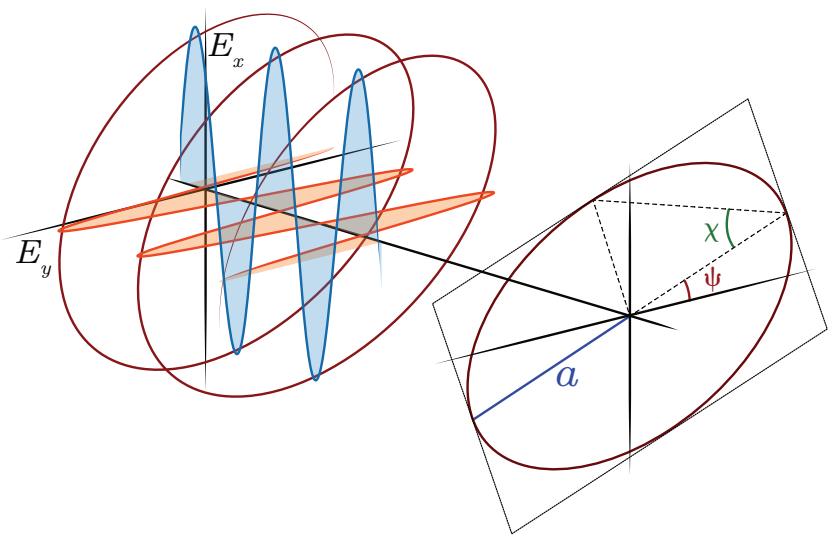

Figure 1.2: Schematic of light polarization and definition of angles used for its description. The depicted parameters are length of main semi-axis a, azimuth ϕ, and ellipticity χ.

This ellipse is determined by phase difference ζ and amplitude ratio between wave components in x and y direction. Neglecting the state of the wave at specific time, this curve can be described by three parameters of choice. This work will use length of main semi-axis a, azimuth ϕ and ellipticity χ. Their definition is shown in Fig. 1.2 and their values can range between

$$a \in [0, \infty], \tag{1.24}$$

$$\psi \in \left[-\frac{\pi}{2}, \frac{\pi}{2}\right], \tag{1.25}$$

$$\chi \in \left[-\frac{\pi}{2}, \frac{\pi}{2}\right], \tag{1.26}$$

where the sign of χ contains information about the helicity of the wave. The most significant polarization states are the ones where the ellipse reduces to a line or forms a circle as shown in Fig. 1.3. These states are called linearly and circularly polarized states, respectively. Linearly polarized light has its plane of polarization that does not change while propagating through isotropic medium and vector $\vec{E}$ never leaves this plane. Circularly polarized light forms in space a symmetrical helix. This helix can be right of left handed giving names to two different circularly polarized states.

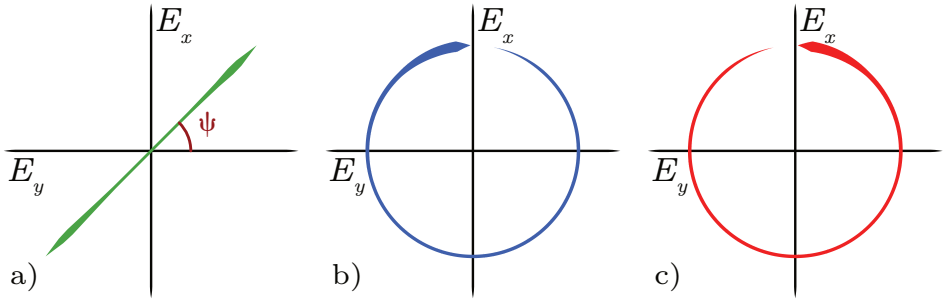

Figure 1.3: Schematic of significant polarization states. a) Linear polarization, b) Right-handed circular polarization, c) Left-handed circular polarization.

1.3 Jones formalism

This section is dedicated to introduction into mathematical apparatus that will be needed for the part III of this work. It starts with a brief introduction of Jones formalism, that is used for description of the optical system and light propagation through it.

Optical experiments used throughout this work use fully polarized light and focus on the polarization changes caused by passing through the apparatus. It is therefore favorable, to use mathematical formalism capable of easy description of the polarization state of electromagnetic wave.

Jones vector

The foundation stone of the formalism containing the information about the light is the Jones vector. It is constructed from the vector of electric intensity by the definition

$$\vec{J} = \begin{pmatrix} E_{0x} \\ E_{0y} \exp\{i\zeta\} \end{pmatrix} \tag{1.27}$$

This gives us starting Jones vector in the base of linearly polarized light with plane of polarization in the direction of x and y axes. This vector can describe any arbitrary polarization state. The list of examples is listed in Tab. 1.1. The base formed from linearly polarized light in direction of x and y axes is not the only possible choice, but arbitrary polarization states can be chosen. Transformation among bases follows the standard operations of linear algebra described for example in Ref. [12].

Jones matrix

Linear algebra states that relation between two n-dimensional vectors is described by $n \times n$ matrix. Such matrix is used to describe any optical element in the system. Since the Jones vector consists of complex numbers, so will the Jones matrix. In general, this matrix is written as

$$\mathbb{M} = \begin{pmatrix} m_{11} & m_{12} \\ m_{21} & m_{22} \end{pmatrix}. \tag{1.28}$$

Linearly polarized in x-axis	$\begin{pmatrix} 1 \\ 0 \end{pmatrix}$
Linearly polarized at 45°	$\frac{\sqrt{2}}{2}\begin{pmatrix} 1 \\ 1 \end{pmatrix}$
Right-handed circular polarization	$\frac{\sqrt{2}}{2}\begin{pmatrix} 1 \\ -i \end{pmatrix}$
Left-handed circular polarization	$\frac{\sqrt{2}}{2}\begin{pmatrix} 1 \\ i \end{pmatrix}$

Table 1.1: Jones vectors for significant polarization states.

	linear base	circular base
polarizer at angle α	$\begin{pmatrix} \cos^2\alpha & \sin\alpha\cos\alpha \\ \sin\alpha\cos\alpha & \sin^2\alpha \end{pmatrix}$	$\frac{1}{2}\begin{pmatrix} 1 & e^{2i\alpha} \\ e^{-2i\alpha} & 1 \end{pmatrix}$
$\delta-$ waveplate at x axis	$\begin{pmatrix} e^{i\frac{\delta}{2}} & o \\ 0 & e^{-i\frac{\delta}{2}} \end{pmatrix}$	$\frac{1}{2}\begin{pmatrix} \cos\frac{\delta}{2} & i\sin\frac{\delta}{2} \\ i\sin\frac{\delta}{2} & \cos\frac{\delta}{2} \end{pmatrix}$
Polarization rotator by θ	$\begin{pmatrix} \cos\theta & -\sin\theta \\ \sin\theta & \cos\theta \end{pmatrix}$	$\frac{1}{2}\begin{pmatrix} e^{i\theta} & 0 \\ 0 & e^{-i\theta} \end{pmatrix}$

Table 1.2: Jones matrixes of common optical elements.

The Jones vector after passing through this element is obtained through matrix multiplication

$$\vec{J_f} = \mathbb{M}\vec{J_i}, \tag{1.29}$$

where $\vec{J_i}$ and $\vec{J_f}$ are initial and final state, respectively. An example of commonly used Jones matrices is listed in Tab. 1.2.

The sample is, depending on geometry, represented by Jones reflection or transmission matrix. In general form, they are written as

$$\mathbb{S}_r = \begin{pmatrix} r_{ss} & r_{sp} \\ r_{sp} & r_{pp} \end{pmatrix}, \quad \mathbb{S}_t = \begin{pmatrix} t_{ss} & t_{sp} \\ t_{sp} & t_{pp} \end{pmatrix}, \tag{1.30}$$

where r_{ij} and t_{ij} denotes Jones reflection and transmission coefficients, respectively.

Optical system usually consists of several optical elements. We can easily describe such situation with multiplication of matrices of each element in order

$$\mathbb{M} = \mathbb{M}_n \dots \mathbb{M}_1. \tag{1.31}$$

The resulting matrix works the same way with Jones vectors as was described in equation 1.29.

An intensity of light described by the Jones vector $\vec{J_f}$ is calculated through relation

$$I = \vec{J_f}^{\,\dagger} \cdot \vec{J_f}. \tag{1.32}$$

This step is necessary for obtaining a real measurable quantity.

1.4 Yeh formalism

Yeh's formalism is used for description of the propagation of light though anisotropic multilayers. It was first introduced to describe propagation of light in anisotropic non-absorbing layered media. The extension for absorbing media and magneto-optical effects was introduced later in 1986 [13]. It is based on a solution of the wave equation for anisotropic medium. Resulting four eigenmodes form the base of vectors $\vec{E_0}$ used in this formalism to describe electric field. Therefore, it also works with 4×4 matrices to describe any change of these vectors. This apparatus will be used for both, calculating of the magneto-optical response and extraction of the permittivity tensor from measured data.

Lets consider a set of m layers that are parallel to z axis. Each layer have thicknesses of t_i and permittivity of $\hat{\varepsilon}^{(i)}$. The incident light is described by wave vector $\vec{k_0}$. For the description of propagation through such system, it is necessary to describe changes at the interfaces as well as propagation through individual layers. This is done for nth layer through matrices $\mathbb{D}^{(n)}$ and $\mathbb{P}^{(n)}$, respectively. With this notation the relation between vectors of electric field is written as

$$\mathbb{D}^{(n-1)}\vec{E}_0^{(n-1)}(z_{n-1}) = \mathbb{D}^{(n)}\mathbb{P}^{(n)}\vec{E}_0^{(n)}(z_n). \tag{1.33}$$

For the purpose of shorter notation in description of these matrices, reduced wave vector it introduced by definition

$$\vec{\bar{N}} = \frac{c}{\omega}\vec{k}. \tag{1.34}$$

The matrix $\mathbb{P}$ is called propagation matrix and its elements are written as

$$\mathbb{P}_{ij}^{(n)} = \delta_{ij} \exp\left\{ i\frac{\omega}{c}\bar{N}_{3j}^{(n)} t_n \right\}, \tag{1.35}$$

where $\bar{N}_{3j}^{(n)}$ denotes the third component of reduced wave vector of the jth eigenmode in the nth layer. Changes at the interfaces are described by dynamic matrix $\mathbb{D}$. Its origin is based on boundary conditions at the interfaces and the elements are calculated as

$$\mathbb{D}_{1j}^{(n)} = -\varepsilon_{12}(\varepsilon_{11} - \bar{N}_2^2) + \varepsilon_{11}(\varepsilon_{12} + \bar{N}_2\bar{N}_{3j}), \tag{1.36}$$

$$\mathbb{D}_{2j}^{(n)} = \bar{N}_{3j}^{(n)}[-\varepsilon_{12}^{(n)}(\varepsilon_{33}^{(n)} - \bar{N}_2^2) + \varepsilon_{13}(\varepsilon_{32}^{(n)} + \bar{N}_2\bar{N}_{3j}^{(n)}] = \bar{N}_{3j}^{(n)} D_{1j}^{(n)}, \tag{1.37}$$

$$\mathbb{D}_{3j}^{(n)} = (\varepsilon_{33}^{(n)} - \bar{N}_2^2)(\varepsilon_{11}^{(n)} - \bar{N}_2^2 - \bar{N}_{3j}^{(n)^2}) - \varepsilon_{13}^{(n)}\varepsilon_{31}^{(n)}, \tag{1.38}$$

$$\begin{aligned}\mathbb{D}_{4j}^{(n)} = -(\varepsilon_{11}^{(n)} - \bar{N}_2^2 - \bar{N}_{3j}^{(n)^2})(\bar{N}_2^{(n)}\varepsilon_{32}^{(n)} + \bar{N}_{3j}^{(n)}\varepsilon_{33}^{(n)}) \\ +\bar{N}_{3j}^{(n)}\varepsilon_{13}^{(n)}\varepsilon_{31}^{(n)} + \bar{N}_2^{(n)}\varepsilon_{31}^{(n)}\varepsilon_{12}^{(n)}\end{aligned} \tag{1.39}$$

Derivation of these equation can be found in Ref. [14]. Equation 1.33 can be further rearranged using inverse dynamic matrix

$$\vec{E}_0^{(n-1)}(z_{n-1}) = [\mathbb{D}^{(n-1)}]^{-1}\mathbb{D}^{(n)}\mathbb{P}^{(n)}\vec{E}_0^{(n)}(z_n) = \mathbb{T}_{n-1,n}\vec{E}_0^{(n)}(z_n) \tag{1.40}$$

introducing transfer matrix $\mathbb{T}_{n-1,n}$. This form is often used to shorten and simplify the notation. We can also further chain the relation 1.40 to obtain

$$\vec{E}_0^{(0)}(z_0) = \left[\Pi_{n=1}^{m+1}\mathbb{T}_{n-1,n}\right]\vec{E}^{(m+1)}(z_m) = \mathbb{M}\vec{E_0}^{(m+1)}(z_m). \tag{1.41}$$

In the last step, the matrix $\mathbb{M}$ was introduced. This matrix relates the electric fields in front and behind the structure.

The matrix $\mathbb{M}$ can be used to derive Jones reflection and transmission matrices. Considering common optical experiment, where the sample is illumination only from one side, the elements of vector of electric intensity behind the sample must follow

$$E_{02}^{(m+1)} = E_{04}^{(m+1)} = 0. \tag{1.42}$$

This simplifies the equation 1.41 to

$$\begin{pmatrix} E_{01}^{(0)}(z_0) \\ E_{02}^{(0)}(z_0) \\ E_{03}^{(0)}(z_0) \\ E_{04}^{(0)}(z_0) \end{pmatrix} = \begin{pmatrix} M_{11} & M_{12} & M_{13} & M_{14} \\ M_{21} & M_{22} & M_{23} & M_{24} \\ M_{31} & M_{32} & M_{33} & M_{34} \\ M_{41} & M_{42} & M_{43} & M_{44} \end{pmatrix} \begin{pmatrix} E_{01}^{(m+1)}(z_0) \\ 0 \\ E_{03}^{(m+1)}(z_0) \\ 0 \end{pmatrix}. \tag{1.43}$$

Further relations are derived by decomposition of this matrix equation into set of linear equations. Comparing notation used in this chapter with the one used for Jones formalism, one obtains relation

$$\begin{pmatrix} r_{ss} & r_{sp} \\ r_{ps} & r_{pp} \end{pmatrix} = \begin{pmatrix} r_{12} & r_{32} \\ -r_{14} & -r_{32} \end{pmatrix} \tag{1.44}$$

and similar relation can be also found for transmission coefficients

$$\begin{pmatrix} t_{ss} & t_{sp} \\ t_{ps} & t_{pp} \end{pmatrix} = \begin{pmatrix} t_{11} & t_{31} \\ t_{13} & t_{33} \end{pmatrix} \tag{1.45}$$

Inserting decomposition of equation 1.43 into these relations yields Jones reflection coefficients

$$r_{ss} = \left(\frac{E_{02}^{(0)}(z_0)}{E_{01}^{(0)}(z_0)} \right)_{E_{03}^{(0)}(z_0)=0} = \frac{M_{21}M_{33} - M_{23}M_{31}}{M_{11}M_{33} - M_{13}M_{31}}, \tag{1.46}$$

$$r_{ps} = -\left(\frac{E_{04}^{(0)}(z_0)}{E_{01}^{(0)}(z_0)} \right)_{E_{03}^{(0)}(z_0)=0} = -\frac{M_{41}M_{33} - M_{43}M_{31}}{M_{11}M_{33} - M_{13}M_{31}}, \tag{1.47}$$

$$r_{pp} = -\left(\frac{E_{04}^{(0)}(z_0)}{E_{03}^{(0)}(z_0)} \right)_{E_{01}^{(0)}(z_0)=0} = -\frac{M_{11}M_{43} - M_{41}M_{13}}{M_{11}M_{33} - M_{13}M_{31}}, \tag{1.48}$$

$$r_{sp} = \left(\frac{E_{02}^{(0)}(z_0)}{E_{03}^{(0)}(z_0)} \right)_{E_{01}^{(0)}(z_0)=0} = \frac{M_{11}M_{23} - M_{21}M_{13}}{M_{11}M_{33} - M_{13}M_{31}} \tag{1.49}$$

and transmission coefficients

$$t_{ss} = \left(\frac{E_{01}^{(m+1)}(z_m)}{E_{01}^{(0)}(z_0)} \right)_{E_{03}^{(0)}(z_0)=0} = \frac{M_{33}}{M_{11}M_{33} - M_{13}M_{31}}, \tag{1.50}$$

$$t_{ps} = \left(\frac{E_{03}^{(m+1)}(z_m)}{E_{01}^{(0)}(z_0)} \right)_{E_{03}^{(0)}(z_0)=0} = \frac{-M_{31}}{M_{11}M_{33} - M_{13}M_{31}}, \tag{1.51}$$

$$t_{pp} = \left(\frac{E_{03}^{(m+1)}(z_m)}{E_{03}^{(0)}(z_0)} \right)_{E_{01}^{(0)}(z_0)=0} = \frac{M_{11}}{M_{11}M_{33} - M_{13}M_{31}}, \tag{1.52}$$

$$t_{sp} = \left(\frac{E_{01}^{(m+1)}(z_m)}{E_{03}^{(0)}(z_0)} \right)_{E_{01}^{(0)}(z_0)=0} = \frac{-M_{13}}{M_{11}M_{33} - M_{13}M_{31}}. \tag{1.53}$$

Knowledge of $\mathbb{M}$ presents clear relation between the permittivity tensor of studied sample and the measured data from experiment. As mentioned above, this information can be used to either obtain the permittivity tensor or calculate theoretical magneto-optical response of arbitrary layered structure under various conditions.

2. Description of matter

The materials studied within this work were prepared in the form of singlecrystalline or polycrystalline thin films. One might ask, why is crystallinity so important? Important electronic properties of solids are best expressed in crystals. Since the interaction of light with matter is mediated by electrons, crystallinity has significant impact on both, optical and magneto-optical properties.

An ideal crystal is formed by stacking identical building blocks to fill the whole space. These blocks can be from single atoms to complex groups of molecules. The crystal is therefore three-dimensional periodic array of these block, apart from any imperfections and impurities that may accidentally be included or built into the structure. Even thought, it is a macroscopic object, its building block are so small, they cannot be optically resolved. That is the reason, why their structure could not be well studied until the discovery of X-ray diffraction. Laue was the first to develop the theory predicting the diffraction of X-ray radiation occurring by periodic array of atoms and his colleges afterwards demonstrated first experimental observations of X-ray diffraction by crystals. This technique required the wavelength of used radiation to be comparable to the size of building block and therefore X-ray radiation was necessary for its working. Since that time, many advanced techniques for investigation of solid matted were developed; however, X-ray diffraction remains the most commonly used technique.

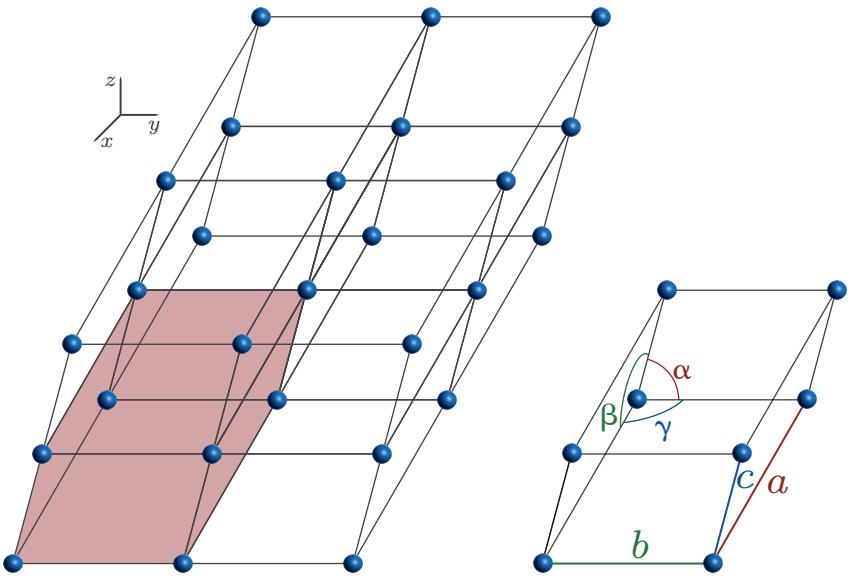

Figure 2.1: Schematic of one possible choice of unit cell and parameters used for its description. (a, b, c) denotes the lengths of cell edges and (α, β, γ) the angles between them.

2.1 Lattice parameters

The smallest building block forming a crystal is called a unit cell. Based on the unit cell, one can fully describe geometry of the system by six lattice parameters.

The most commonly used are lengths of cell edges (a, b, c) and appropriate angles between them (α, β, γ). Since the unit cell forms its own cartesian coordinate system, one can also use fractional coordinates (x_i, y_i, z_i) for description of position inside the cell. One example of possible choice of unit cell with its coordinate system is depicted in Fig. 2.1.

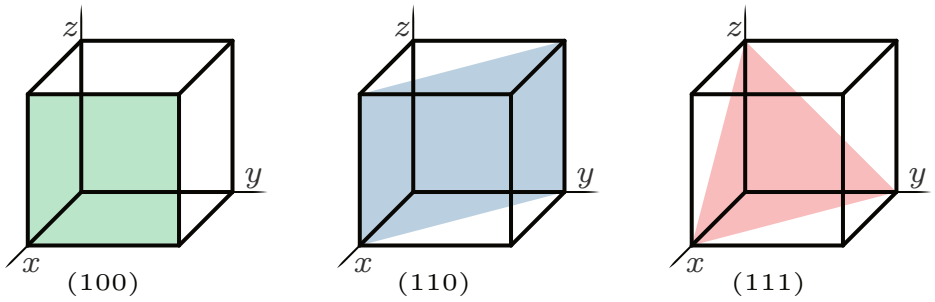

Figure 2.2: Charts of Miller indices further used in this work.

2.2 Miller indices

Oftentimes, it is more convenient for description of crystal to focus on planes in the crystal instead of single atoms. Therefore, Miller indices are introduced written as (hkl). This notation denotes the planes defined by vector $h\vec{b_1} + k\vec{b_2} + l\vec{b_3}$, where $\vec{b_i}$ are base vector of reciprocal space lattice. Further details about definition of reciprocal space can be found in Ref. [15]. The Miller indices used in this work are shown in Fig. 2.2.

2.3 Magnetism

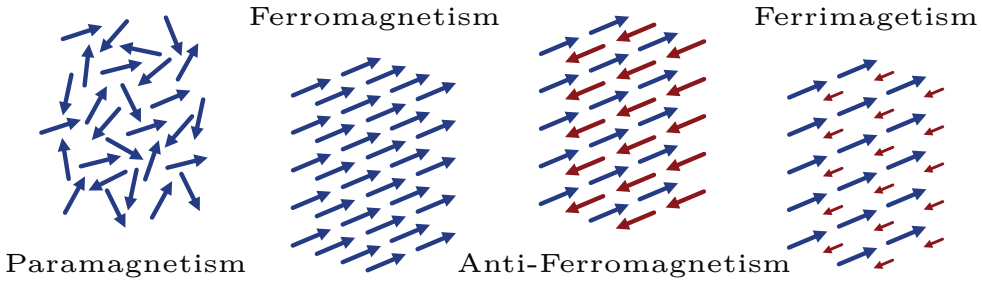

Figure 2.3: Schematic of qualitative types of magnetic orderings in the crystal. Second color denotes presence of another magnetic sublattice.

The history of magnetism is as old as history of science itself. The ability of certain materials to attract ferrous object puzzled the curious minds for over two millennia. Even though the first fabrications of permanent magnets dates back to ancient China, its physical origin was not understood until the 19th century. The

first clue was discovered by Hans-Christian Oersted. He observed, that wire carrying electrical current produced magnetic field deflecting a compass needle, finding existence of relation between magnetism and electricity. This breakthrough led to the series of discoveries leading to the unified theory of electromagnetism, formulated by James Clerk Maxwell. However, the explanation of magnetic properties of solid matter emerged even after the foundation of quantum mechanics and relativity. Based on electron configuration, magnetic materials are resolved into several qualitatively different types of magnetism as shown in Fig. 2.3. These categories are closely connected to the response of material to the external magnetic field. The materials presented in this work are ferrimagnets and therefore the further text will focus on materials with spontaneous magnetization. This phenomenon occurs in materials that have more than one unpaired valence electron. These electrons therefore tends to interact with each other inducing strong parallel or anti-parallel alignments. Such material remains magnetized even in the absence of an external magnetic field. The spontaneous magnetization, due to the alignment of atomic magnetic moments, depends on temperature. The critical point, where magnetization drops to zero, is called the Curie temperature T_C. At this point, magnetic ordering is broken by the phonon interaction and the material becomes paramagnetic. This temperature strongly depends on the material. While magnetic metals have the Curie temperature above 1000 K, in case of magnetic semiconductors it typically lies below 100 K.

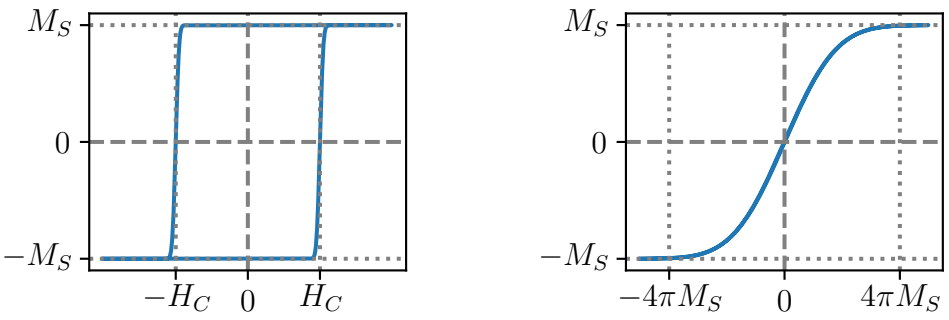

(a) Easy-axis

(b) Hard-axis

Figure 2.4: Typical magnetization hysteresis loops for magnetization (a) easy-axis and (b) hard-axis with external magnetic field applied in their directions.

Ferromagnetism

In case of exchange interaction favouring the parallel alignment, the material is called ferromagnetic. Its essential characteristic is the irreversible nonlinear response of magnetization to an external magnetic field. This behavior manifest in magnetization hysteresis loop such as ones in Fig. 2.4. Difference between these curves will be explained further below. Typical ferromagnetic metal, such as iron or cobalt, can reach values of magnetization, the magnetic dipole moment per unit volume of material, in the order of 1000 kA/m.

Antiferromagnetism

In an antiferromagnet, the atomic moments form two equivalent, but oppositely oriented magnetic sublattices. The resulting net magnetization is equal to zero and their magnetic state remains intact even while in presence of very large external magnetic fields. Antiferromagnets also poses phase transition, occurring at the Néel temperature, when the moments begin to order.

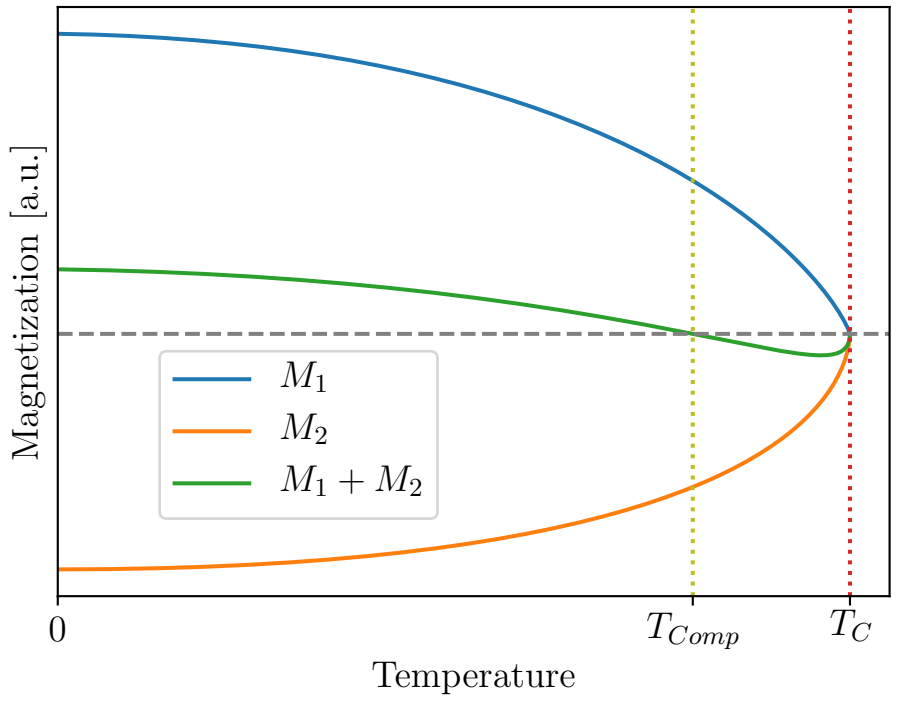

Figure 2.5: Temperature dependence of magnetization of typical ferrimagnet with compensation temperature. M_1 and M_2 denotes contribution of individual magnetic sublattices. $M_1 + M_2$ is resulting net magnetization.

Ferrimagnetism

Ferrimagnetism occurs in materials with at least two magnetic sublattices that are uneven and prefer anti-parallel orientation. Therefore, ferrimagnets posses spontaneous net magnetization that is usually much smaller than in the case of ferromagnets (garnet $M_S \approx 150$ kA/m). This behavior is commonly found in magnetic oxides such as garnets. Competition of magnetic sublattices also introduces possibility of very specific temperature dependence of magnetization. Similarly to ferromagnets, moment of each magnetic sublattice lowers while reaching to Currie temperature; however, each of them with difference pace. This behavior can results in the presence of another specific temperature called compensation temperature T_{Comp}, where these moments reach the same size (Fig. 2.5). Above this temperature, there is also change of dominant magnetic sublattice causing opposite alignment of magnetic sublattices in the external magnetic field as shown in Fig. 2.6. This change is caused by tendency of net magnetic moment, that has

same direction as dominant sublattice, to align parallelly with the external magnetic field. It is worth noting, that magnetic moments of sublattices can be in theory aligned with arbitrary angle between them.

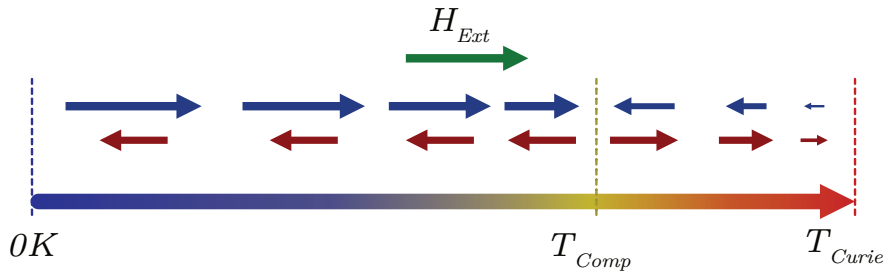

Figure 2.6: Effect of external magnetic field on orientation of magnetic sublattices of ferrimagnet with compensation temperature T_{Comp} at different temperatures.

Magnetic anisotropy

In spontaneous magnetic materials, the direction of magnetization is usually constrained along one or more easy-axes. Due to association of magnetism with circulating electron currents, time reversal symmetry requires the same energy of state with opposite orientation of magnetization. This tendency is represented by the anisotropy energy

$$E_a = K_a \sin^2 \theta, \tag{2.1}$$

where K_a is the anisotropy constant for axis a and θ is the angle between the direction of magnetization and the axis a. Anisotropy constant consists of three terms

$$K_a = K_{sh}^a + K_{el}^a + K_{cr}^a, \tag{2.2}$$

where the terms are called in order the shape anisotropy, the magnetoelastic anisotropy and the magnetocrystalline anisotropy. Magnetocrystalline anisotropy is determined by symmetry of the crystal and usually favors one of the crystallographic directions. The contribution of shape anisotropy is based on the geometry of the system. It originates from boundary conditions of Maxwell's equations that minimize the amount of magnetic flux leaving the material. In the case of thin films, the shape anisotropy has the smallest contribution for in-plane direction. The last, magnetoelastic anisotropy, is defined as

$$K_{el}^a = \lambda_a \sigma_a, \tag{2.3}$$

where λ_a is the magnetostriction coefficient and σ_a the strain applied in the direction of axis a. After resolving of all contributions into anisotropy energy in main crystallographic directions, easy-axis will lay in direction of its minima. Typical magnetization loops of ferromagnetic or ferrimagnetic materials that are the result of uniaxial anisotropy are shown in Fig. 2.4. The magnetization easy-axis typically has non-zero magnetization in remanence M_r as well as coercivity field H_C. The magnetization hard-axis is used to determine anisotropy field,

where the magnetization reaches the values of M_S in this direction. At this point, all magnetic moments are forced by the external magnetic field to lay in the direction of magnetization hard-axis.

In the case of thin films, it is common to address direction of magnetic anisotropy relatively to the surface of the sample. Therefore, the film with the magnetization easy-axis perpendicular to the surface of the film is said to exhibit perpendicular magnetic anisotropy (PMA).

3. Interaction of light and matter

3.1 Permittivity tensor

Chapter 1 demonstrated that interaction of light in visible spectral region and matter can be macroscopically described by permittivity tensor $\hat{\varepsilon}$. This 3×3 tensor has in general 9 independent elements. However, one can use particular symmetries of the problem to significantly reduce their number. From a microscopic theory studying general properties of relaxation function one can deduce Onsager reciprocity relations that apply to the permittivity tensor. They imply requirement of time reversal symmetry on permittivity tensor that reduces its form into

$$\hat{\varepsilon_r} = \begin{pmatrix} \varepsilon_{11} & \varepsilon_{12} & \varepsilon_{13} \\ -\varepsilon_{12} & \varepsilon_{22} & \varepsilon_{23} \\ -\varepsilon_{13} & -\varepsilon_{23} & \varepsilon_{33} \end{pmatrix} \tag{3.1}$$

Materials studied in this work are in the presence of no external fields optically isotropic. In such cases, the rotation symmetry reduces the number of independent elements even further to

$$\hat{\varepsilon_r} = \begin{pmatrix} \varepsilon_1 & 0 & 0 \\ 0 & \varepsilon_1 & 0 \\ 0 & 0 & \varepsilon_1 \end{pmatrix} \tag{3.2}$$

This form of tensor could be reduced to a scalar. However, it required the absence of any external source. Therefore, it could not be used for magneto-optical effects.

3.2 Nonreciprocal Birefringence

The presence of an external field causes breaking of symmetry and the propagation of light starts to differ upon reversing of the direction of propagation. We will focus solely on effects caused by magnetic field and hence the phenomenon is called magnetic birefringence. Similarly to two standard bases for description of polarization of light, we distinguish birefringence occurring in bases of linearly and circularly polarized light. This approach is very convenient, because the symmetry allows in each case only certain order of perturbation caused by the external magnetic field. Change of propagation of linearly polarized light called magnetic linear dichroism (MLD) exhibits quadratic dependence on external magnetic field. Even though this effect is lately having more attention due to its possible applications for probing of antiferromagnetic materials, its amplitude is very small. One example of study of this phenomenon is in Ref. [16]. The main focus of this work were changes in propagation of light with circular polarizations that are linear in magnetization and called magnetic circular birefringence (MCB). As the name suggests, MCB is the property of a medium with two distinct propagation constants [17, 18], raising from different arrangement of internal dipole moments in a medium.

The propagating light is influenced by combined quantum orbital and spin angular momenta of the individual ions. Since an orbiting electron creates both,

an electric- and a magnetic-dipole moment, it is important to keep in mind its dual nature. In the permittivity case, the electric-dipole aspect of the orbital momentum produces the interaction, but the essential alignment of the individual dipoles for a collective result is accomplished by magnetic alignment. When we look at pure magnetic-dipole case, the optimal interaction is achieved when $\vec{B}$ of light is transverse to the axis of the magnetization vector $\vec{M}$ in the material.

The spectral dependency of permeability and permittivity is caused by respective magnetic- and electric-dipole interaction with a propagating electromagnetic wave. Since the direct magnetic-dipole contributions are negligible at optical frequencies, we can further focus only on electric-dipole transitions and, similarly to previous sections, set $\mu_r = 1$.

Considering the external magnetic field a small perturbation of the system, an element of permittivity tensor can be written as

$$\varepsilon_{ij} = \varepsilon^0_{ij} + K_{ijk}M_k + G_{ijkl}M_kM_l, \tag{3.3}$$

where ε^0_{ij} are unperturbed components, M_k components of magnetization vector, K_{ijk} and G_{ijkl}, are elements of the linear and the quadratic magneto-optical tensor, respectively. Study of G is not in the focus of this work and therefore it is neglected in the further text. Without prejudice to generality, the magnetization vector direction will be chosen along the z axis. This geometry is usually called polar. The other choices of magnetization along one of the Cartesian axis are called longitudinal and transversal. Schematic of these geometries is depicted in Fig. 3.2. With this choice, the system preserves its rotation symmetry along z direction and the permittivity tensor has to contain this symmetry. Furthermore, time reversal symmetry has to remain even in the case with non-zero magnetization and therefore

$$\varepsilon_{ij}(\vec{M}) = \varepsilon_{ji}(-\vec{M}). \tag{3.4}$$

Considering these symmetries, only one independent element of the permittivity tensor becomes non-zero. Due to various historical reasons, several sign conventions are used among different works. However, this work use the notation with permittivity tensor for polar configuration written as

$$\hat{\varepsilon_r} = \begin{pmatrix} \varepsilon_1 & i\varepsilon_2 & 0 \\ -i\varepsilon_2 & \varepsilon_1 & 0 \\ 0 & 0 & \varepsilon_1 \end{pmatrix}. \tag{3.5}$$

3.3 Optical transitions

Throughout this work, we will study spectral dependencies of permittivity tensor. These spectra comes from the interaction of matter with light via different microscopic mechanisms which can be electronic transitions, photon interactions, excitons, etc. The diagonal term of the permittivity can be in the first approximation described with classical phenomenological models.

Lorentz model

Even though this classical model is based on a very basic model of atom, it often yields very good description of the observed optical dispersion. It tends to loose its

accuracy at some specific situations, but that can be solved with introduction of corrections as will be shown below. This model was later replaced after foundation of quantum mechanics; however, quite surprisingly the dispersion relation of two level system is the same, if we consider only low-intensity light. The quantum mechanics provides more detailed explanation of parameters present in the model beyond the scope of this work.

The considered system is a classical model of atom consisting of a nucleus and one electron. This electron is bound to the nucleus by combination of atomic and Coulombs forces that can be imagined as spring of stiffness κ attached between them. Without prejudice to generality, the nucleus is positioned in the center of the coordinate system and considered static. The electron of effective mass m_e is assumed very close or at the minima of its potential and it starts from semi-static state. Therefore, the first two terms in the Taylor expansion are sufficient for the description of driving force in the equation of motion. Since the atom is much smaller than wavelength of the light, the simple notation for its electric intensity is written as

$$\vec{E} = \vec{E_0} \exp\left\{i\omega t\right\}. \tag{3.6}$$

The model suspects, that external electric field will cause displacement of the electron, that will give a rise to macroscopic polarization $\vec{P}$, that can be described as

$$\vec{P} = -Nq\vec{y}, \tag{3.7}$$

where N is the number of protons in nucleus, q the unit charge and $\vec{y}$ denotes the displacement of the electron from equilibrium position. Further notation is shortened by introduction of plasma frequency through definition

$$\omega_p^2 = \frac{Nq^2}{m\varepsilon_0}. \tag{3.8}$$

Using introduced notation, the equation of motion for the system can be written as

$$\frac{d^2\vec{P}}{dt^2} + \gamma_e \frac{d\vec{P}}{dt} + \omega_0^2 \vec{P} = \varepsilon_0 \omega_p^2 \vec{\vec{P}}, \tag{3.9}$$

where γ_e describes the dumping of electron's motion and $\omega_0^2 = \frac{\kappa}{m_e}$ was used. Since this is well known form of differential equation for harmonic oscillator, the result can be sought in the form of

$$\vec{P}(\omega, t) = \vec{P}(\omega) \exp\left\{i\omega t\right\}. \tag{3.10}$$

Solving this equation yields the polarization

$$\vec{P}(\omega) = \frac{\varepsilon_0 \omega_p^2}{(\omega_0^2 - \omega^2) + i\gamma_e \omega} \vec{E_0}. \tag{3.11}$$

Comparison of this equation with definition of polarization through relative permittivity

$$\vec{P} = \varepsilon_0 \left(\hat{\varepsilon_r} - 1\right) \vec{E_0}. \tag{3.12}$$

provides description of dispersion of the diagonal term of permittivity tensor

$$\varepsilon_1 = 1 + \frac{\omega_p^2}{\omega_0^2 - i\omega\gamma_e - \omega^2}. \tag{3.13}$$

This dispersion relation of single electron is depicted in Fig. 3.1. In the most of materials, there is more than only one optically active electron. Moreover, every electron can behave differently. Therefore, the overall optical response can be described as

$$\varepsilon_1 = 1 + \sum_j \frac{a_j \omega_{pj}^2}{\omega_{0j}^2 - i\omega\gamma_{ej} - \omega^2}, \tag{3.14}$$

where a_j is called the oscillator strength. The plasma frequency can also differ between the electrons.

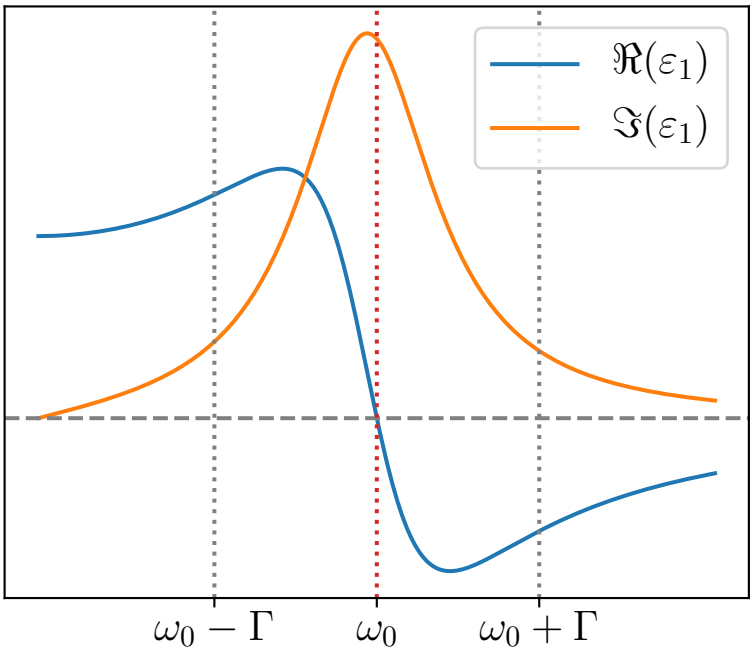

Figure 3.1: Real and imaginary part of spectral dependence of diagonal element, ε_1, of permittivity tensor of transition described by Lorentz oscillator situated at energy E_0 with broadness of Γ.

Tauc-Lorentz model

In the vicinity of absorption edge, the Lorentz model starts to significantly differ from experimental data. Therefore, Tauc-Lorentz model was developed to address this problem. It introduces only one extra parameter of ω_g and different behavior below and above this energy. For energies below bandgap is imaginary part of ε_1 set zero. For the energies above the correction looks like

$$\Im(\varepsilon_1)(\omega) \propto [(\omega - \omega_g)^2/\omega^2] \tag{3.15}$$

Real part of ε_1 is usually calculated through Kramers-Kronig relations. Further details with more possible corrections can be found in Ref. [11].

3.4 Magneto-optical transitions

Microscopic origin of spectral features in off-diagonal part of the permittivity tensor, ε_2, can be explain by the effect of magnetic field on the band structure. Due to spin-orbital coupling, present Zeeman field causes splitting of degenerated states of non-zero angular momentum. For the simplicity, splitting of only one state will be considered. There are two possible scenarios depending on the band structure. They are, splitting of the excited state as shown in Fig. 3.3a or splitting of the ground state as in Fig. 3.3b. We associate these models with name double and single transition, respectively. In both cases, there are two transitions for each polarization mode that has small difference in energies caused by Zeeman splitting. These modes are exclusive to one polarization state due to the selection rules [19].

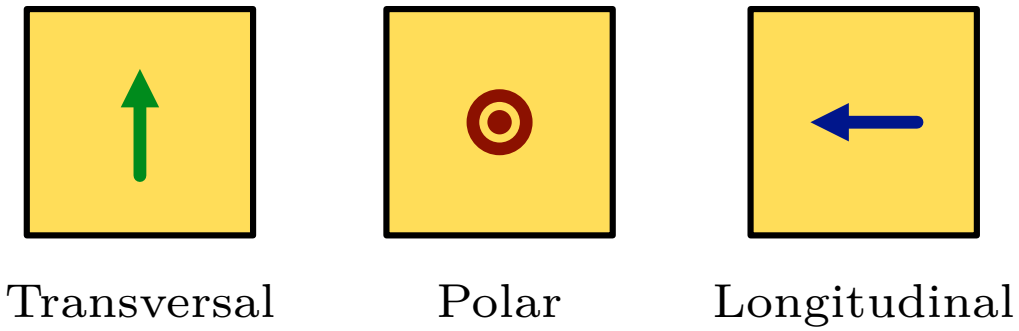

Figure 3.2: Schematic of geometries of applied external magnetic field orientation used for measurement of Kerr effect with their names. Transversal geometry denotes magnetization in-plane of the sample and perpendicular to the plane of incidence, polar has magnetization pointing out-of-plane of sample surface and longitudinal has the magnetization parallel to samples surface as well as plane of incidence.

The spectral dependencies of off-diagonal terms of permittivity originating from magneto-optical transitions are derived in Refs.[19, 20]. In the case of single transition (paramagnetic) the formula describing the spectral dependence is written as

$$\varepsilon_2(E) = \varepsilon_2'(E) - i\varepsilon_2''(E) \tag{3.16}$$

$$\varepsilon_2'(E) = AE\frac{E_0^2 - E^2 - \Gamma^2}{(E_0^2 - E^2 + \Gamma^2)^2 + (2E\Gamma)^2} \tag{3.17}$$

$$\varepsilon_2''(E) = A\frac{\Gamma(E_0^2 + E^2 + \Gamma^2)}{(E_0^2 - E^2 - \Gamma^2)^2 + (2E\Gamma)^2} \tag{3.18}$$

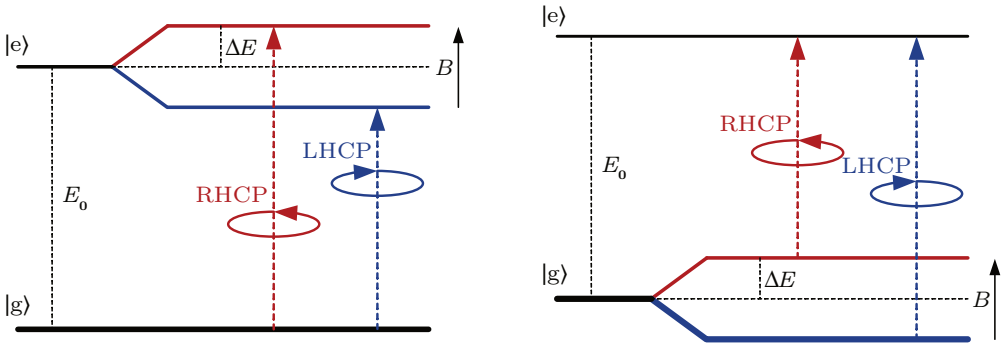

(a) Double (diamagnetic) transition (b) Single (paramagnetic) transition

Figure 3.3: Diagrams of magneto-optical transitions. (a) Double (paramagnetic) transition has splitting of the energy levels on the excited level. (b) Single (diamagnetic) transition has the splitting of the energy levels on the ground state.

For the double transition (diamagnetic) it has the form

$$\varepsilon_2(E) = \varepsilon_2'(E) - i\varepsilon_2''(E) \tag{3.19}$$

$$\varepsilon_2'(E) = A\frac{(E_0 - E)^2 - \Gamma^2}{((E_0 - E)^2 + \Gamma^2)^2} \tag{3.20}$$

$$\varepsilon_2''(E) = 2A\frac{(E_0 - E)\Gamma}{((E_0 - E)^2 + \Gamma^2)^2} \tag{3.21}$$

In both cases, A will be addressed as strength of the transition, Γ its broadness and E_0 its central energy. In chapter 11, A is treated as one fitting constant. However, it has several terms contributing to its value. The strength of the transition is proportional to

$$A \approx \omega_p^2 f \xi L, \tag{3.22}$$

where ω_p is the plasma frequency defined above, ξ is the separation between the levels caused by spin-orbit coupling, f is number of contributing atoms per unit volume and L is the Lorentz-Lorenz local filed correction which equals $[(n^2 + 2)/3]$. Examples of spectral shapes of individual transitions are shown in Fig. 3.4. The important phenomenon connected with double transition is the effect of Boltzmann population at split levels. This introduces strong temperature dependance into the formula, making Γ proportional to $1/k_BT$. This behavior is shown in Fig. 3.5. This phenomenon presents useful tool for experimental distinguishing between types of transitions.

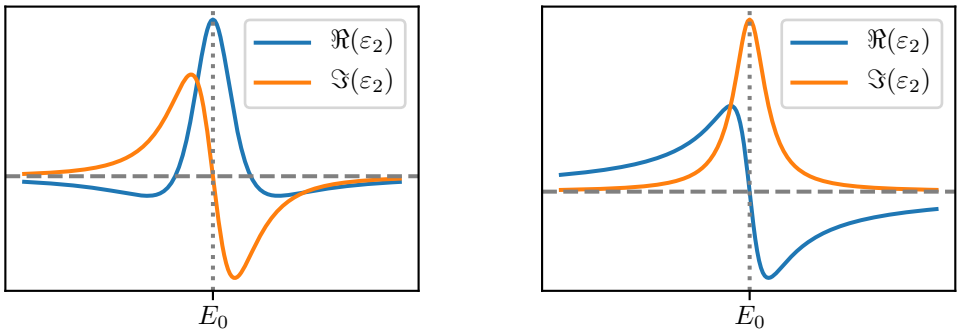

(a) Double transition (b) Single transition

Figure 3.4: Real and imaginary part of spectral dependence of off-diagonal element, ε_2, of permittivity tensor of (a) double transition and (b) single transition situated at energy E_0.

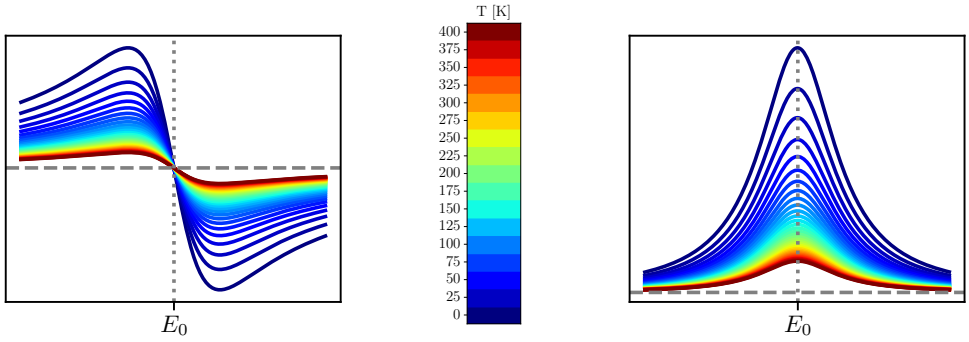

(a) $\Re(\varepsilon_2)$ (b) Scale (c) $\Im(\varepsilon_2)$

Figure 3.5: (a) Real and (c) imaginary part of temperature dependence of spectral dependency of off-diagonal element, ε_2, of permittivity tensor of the single transition.

Part III

Experimental methods

This part covers experimental methods and techniques. At the beginning, it provides the brief introduction to studied material system, its characteristics and key features. Afterwards, there is a description of deposition techniques used for preparation of thin films further studied in this thesis. Lastly, there is summary of experimental techniques. It starts with means of structural analysis and principles of X-ray diffraction. That is followed by introduction to magnetometry used for characterization of magnetic properties. The last chapter of this part is dedicated to optical and magneto-optical techniques with focus on measurement of polarization. At first, it introduces measured quantities used throughout the rest of the thesis. Following section describes the principles of spectroscopic ellipsometry. The last section is dedicated to magneto-optical spectroscopy. Its theoretical concept is explained, followed by description of setup used for the measurements of results presented in part IV.

4. Ferrimagnetic garnets and their preparation

Preparation of samples is arguably the most essential part of the experiment. It is very hard to measure a physical phenomenon, if the studied system does not have the required quality. Since nowadays experimental research tends to focus on even smaller and weaker effects and perturbations, the factor of the sample quality is often the difference between a successful and unsuccessful experiment.

There are many available techniques for material preparation with differences in resulting volume, crystallographic quality, precision of stoichiometry and many other aspects. This chapter focuses on the description of two different techniques which were used for the preparation of the investigated samples.

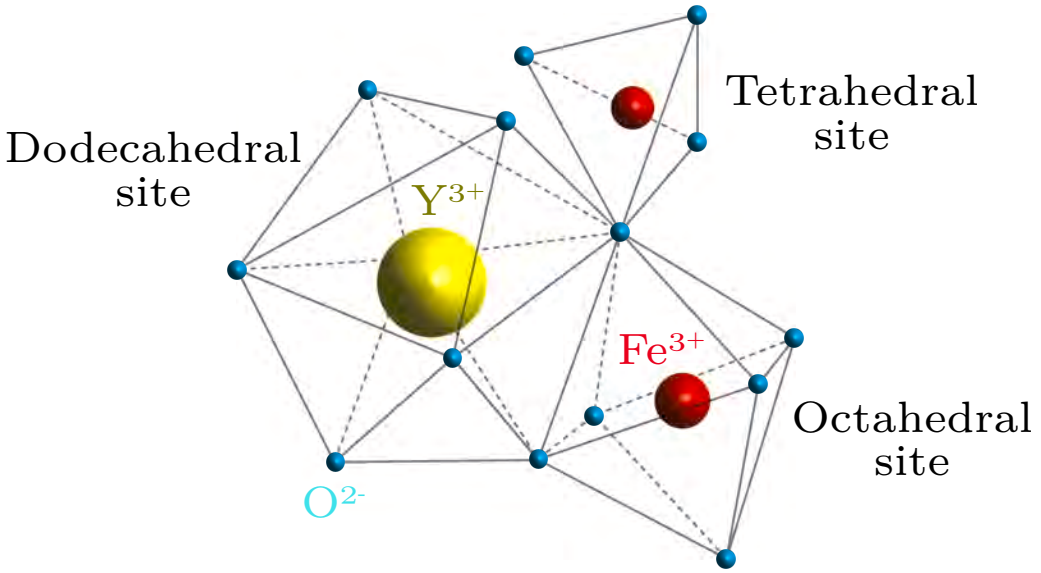

Figure 4.1: Schematic of crystallographic structure of a yttrium iron garnet. Sublattices filled with iron are octahedral and tetrahedral (red dots) and yttrium sits in dodecahedral site (yellow dot). Neighboring oxygens are denoted by blue dots.

4.1 Garnet structure

Ferrimagnetic garnets are members of larger group of magnetic oxides. Among the others, the garnets are chemically and structurally the most stable of ferrimagnetic oxides. The first attempts to synthesize these materials date back to 1956 to Bertaut and Forrat [21]. There were many others following thanks to whom the garnets are nowadays one of the most thoroughly investigated family of materials. The general formula is $X_3Y_2Z_3O_{12}$. The three cation sites are called dodecahedral (X), octahedral (Y) and tetrahedral (Z). Example of material forming such structure is YIG whose crystallographic unit cell is shown in Fig. 4.1.

In comparison to spinels, the principal symmetry axes of octahedral and tetrahedral sites do not conform to the cubic cell axes ⟨100⟩, ⟨111⟩ and ⟨110⟩. The only trigonal axis present in the system is at octahedral site aligned with ⟨111⟩ direction [22]. The other significant difference is the ratio of 3:2 in the favor of tetrahedral site over octahedral. This results in tetrahedral sublattice being dominant contributor to magnetization. Therefore, magnetoelastic properties can be varied over a very wide range.

Other aspect in which garnets overcome spinels are dielectric properties. This can be easily explained by oxidation state of all atoms being 3^+; therefore, they are much less susceptible to forming Fe^{2+}. Its magnetocrystalline anisotropy and magnetostriction are also worth mentioning. Probably the strongest factor, that makes garnets so versatile materials is multitude of possible substituents for all three sites that can be used to tailor magnetic, optical and magneto-optical properties.

The base unit for magnetic garnets is YIG. The basic substituents are Al^{3+} and Ga^{3+} that both reduce its magnetic properties. For the increase of magnetization, the larger ions like In^{3+} or Sc^{3+} can be used. However, these atoms occupy almost exclusively octahedral sites and therefore it is impossible to achieve concentration higher that 0.5 per formula unit. Additionally, they also cause decrease of Curie temperature. In the field of magneto-optics, the most important substituent is definitely Bi^{3+}. Even though this atom achieves enormous increase of magneto-optical response, due to its size, it does not freely substitute for Y^{3+}. There are techniques that achieved fully substituted films; however, they rarely exceed micrometer thickness [23].

Another option is the usage of elements from lanthanide group that substitute at dodecahedral site. These materials have so characteristic properties they form their own group called RE garnets. They are specific for presence of f shell electrons, that couple with d electrons on irons. The first studies of this family were reported by Bertaut and Pauthenet [24, 25]. Due to this coupling, the ferrimagnetic character of the garnet is greatly altered. The most significant feature is the appearance of compensation temperature, that is not present in garnets without magnetic element in dodecahedral sites. These garnets also exhibit much stronger magnetization at low temperatures. Another interesting attribute of RE garnets is introduction of optically and magneto-optically active transition that are at specific energies characteristic to used element.

4.2 Metallo-organic decomposition

The technique of metallo-organic decomposition (MOD) was used for its simplicity and easy usage in further industrial application [26]. That is due to no need for vacuum or going through a gel or powder step. It is very easy to scale and produce high quality thin films of inorganic material with very precise stoichiometry. These films can be grown on various substrates and their thickness is practically not limited.

Simple schematic of the process is shown in Fig. 4.2. The starting materials are metallo-organic compounds of desired elements dissolved in an appropriate solvent. These solutions are mixed together in precise ratio depending on desired stoichiometry of final film. This formula is applied in the form of droplet on heated

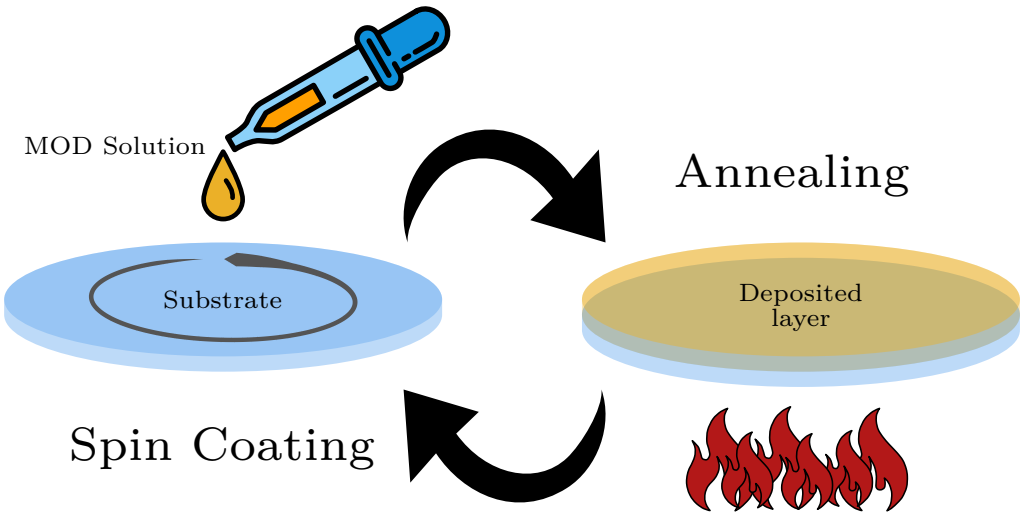

Figure 4.2: Diagram of preparation of thin film by metallo-organic decomposition.

substrate that is spinning. Spinning ensures homogeneous spread of solution through the whole sample. In the first phase, there is evaporation of the solvent. Afterwards, metallo-organic compounds decompose and produces the final film. Resulting layer is only few nanometers thick; therefore, the whole process is often repeated to obtain desired thickness.

The leading factor driving the quality of the film is the starting formula. The ratio of used compounds determines the final stoichiometry, but also the choice of proper metallo-organic material and solvent has great influence on grain size and crystallinity of the sample. The other parameters are temperature of the substrate and speed of its rotation. Whereas the first influences the speed of layer growth and crystallization, the second sets the thickness of deposited layer and its homogeneity.

Even though the quality of sample after deposition is very high, it can be further improved. Most common is annealing of the sample in oxygen rich atmosphere. Depending on the aim of the study, different reactive gasses can be used. More details about garnet preparation with MOD can be found in Ref. [27].

4.3 Pulsed laser deposition

History of pulsed laser deposition (PLD) reaches back to the 1960s. The first attempts to deposit thin layers through laser evaporation followed shortly after construction of the first ruby laser. However, resulting films could hardly compete to well established chemical vapour deposition or molecular beam epitaxy (MBE). The breakthrough came twenty years later with deposition of high quality films of $YBa_2Cu_3O_7$ [28]. These films of high temperature superconductive material were even better than the ones prepared by competing methods. Afterwards, this technique was favorable choice for preparation of various oxide materials such as garnets and perovskites. Further improvement in laser technology that occurred in 1990s led to spread of this method to wider portfolio of materials. Nowadays, PLD is not limited only to oxides, but it can be used for growth of

thin metallic films as well. The main features of PLD is the ability to grow high quality epitaxial films with great stoichiometry transfer and surface quality.

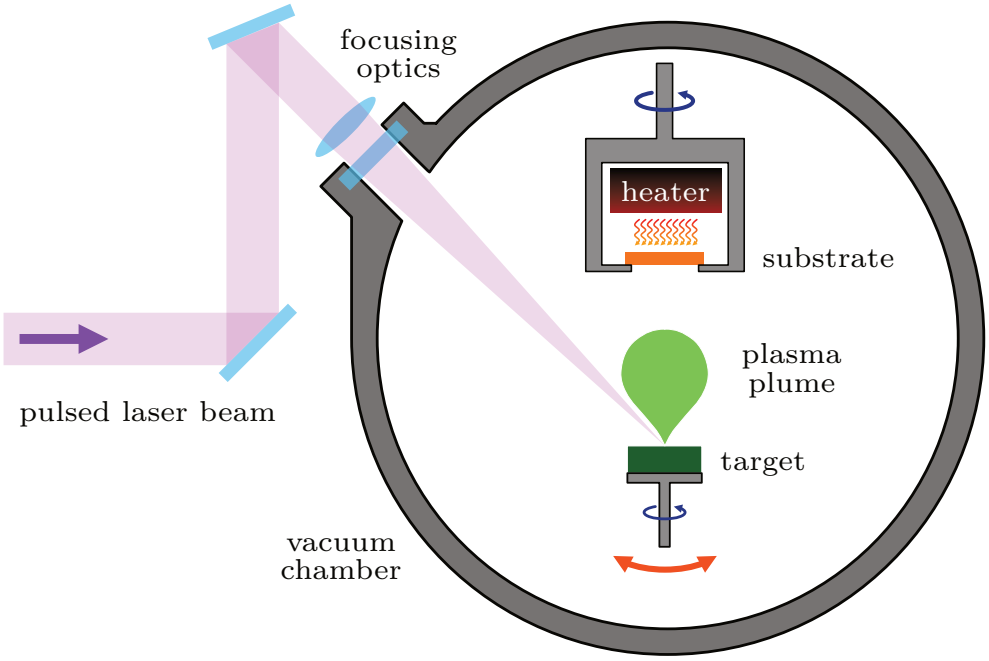

Figure 4.3: Schematic of pulsed lased deposition system. Target (green square) sits on moving carousel. Laser is focused on the surface of the target and its path is marked by violet area. Starting plasma plume is shown above the target. Substrate is sitting above the target in rotating holder in the vicinity of a radiative heater.

The basic schematic of deposition system is shown in Fig. 4.3. The main component of the PLD machine is vacuum a chamber 4.4b. Since the commonly grown materials are oxides, it does not require as high grade of vacuum as for example MBE, but pressures bellow 10^{-5} Torr are favorable to ensure removal of possible contamination of the film. In the vacuum chamber, substrate is positioned on a holder that can be rotated to ensure better homogeneity. Right below the substrate, there is a target of desired material in the form of polycrystalline bulk. This target is usually one inch in diameter and few millimeters thick. Depending on the geometry of the system, it can be also placed on moving platform for uniform ablation of the target as shown in Fig. 4.4b. High power laser is focused through outer window right on the surface of the target. The most commonly used lasers are KrF excimer lasers with power of about 4W. These are instruments of choice for their wavelength in UV region and possibility to produce short nanosecond pulses of power about 400 mJ in single pulse. This power is crucial for proper formation of plasma that occurs after impact of the pulse on the target. The plume propagates from the target towards the substrate, where condensation of transported material occurs. The substrate is often heated to achieve better migration of atoms on the surface. For YIG is the heating temperature around 400 °C. One plume of plasma transport only handful

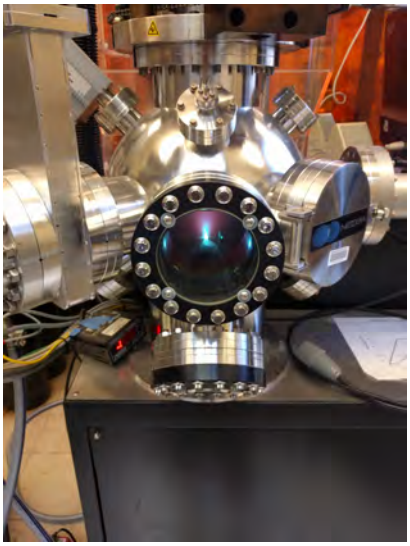

(a) PLD chamber during deposition.

(b) The interior of PLD chamber.

Figure 4.4: Pictures of PLD chambers used for preparation of samples. (a) Chamber during the deposition with the visible part of plasma plume above the target. (b) Inside of the deposition chamber. Target holders are situated in the bottom. Substrate is placed in the holder above them. The heater is retracted on the top. The metal plate on the left is the substrate shutter in the loading position.

of atoms; therefore, the ablation process must be repeated many times to achieve single crystallographic layer. For example, deposition of one nanometer of YIG takes around one thousand shots.

The deposition procedure start with loading of substrate and targets into the chamber. Most PLD systems are not limited to deposition from only one material per round and have the option to move between the targets when desired. Carousel moves the active target to place under the substrate where the laser hits. Initial pump down removes unwanted gasses from the chamber and also cleans the substrate from volatile compound from the surface that will evaporate. Afterwards, working gas is introduced into the system. Typical depositions in pure oxygen atmosphere use pressure of 5 to 600 mTorr, depending on the deposition. Then the substrate is ramped up to the desired deposition temperature. It is vital to introduce the gas before the heating up of the substrate to prevent temperature shock that could cause cracking. Once the temperature stabilizes and the laser is heated up, deposition can be started. It is common to clean the targets prior the deposition process with few thousands shots, while substrate shutter is kept closed. This step is called pre-ablation. Afterwards, substrate shutter is opened and deposition begins. Laser usually runs at two to ten hertz; therefore, the deposition step takes few hours. Due to small amount of transported material per shot, there are two ways to utilize presence of multiple targets in the chamber. The first one is growing of heterostructures keeping only one active target for each layer. The other is fast switching between targets, usually called co-deposition, that allows fabrication of material from two or even more different targets. For example YIG ($Y_3Fe_5O_{12}$) can be deposited from target of yttrium oxide (Y_2O_3) and iron oxide (Fe_2O_3). This also allows further control of stoichiometry of deposited film. When the desired number of shots hit the

targets, substrate temperature is slowly ramped down, while the sample remains in oxygen atmosphere. This step can be thought as a simple annealing process that slightly improves the quality of the film. Once the sample reaches room temperature it can be removed from the chamber and the deposition is done.

Target preparation

The most common technique for preparation of ceramic targets is so called Sintering method. This process can be demonstrated on preparation of YIG target. The starting raw materials are oxides of desired elements. In the case of YIG, the powders are Fe_2O_3 and Y_2O_3. These powders are mixed in right ratio for the garnet stoichiometry and placed after mixing with water in ball mill for several hours to achieve good homogeneity of the substance. Afterwards, the powder is dried out and pressed into shape of desired target as shown in Fig. 4.5a. As a next step, the material is placed in tube furnace and heated to 1150 °C. Afterwards, it is kept there for five hours. This process is called Calcining. The forming of garnet from reactants happens through intermediate compound with a perovskite structure and chemical formula $YFeO_3$ [29]. This reaction occurs at lower temperature than the formation of garnet; therefore, after calcining the target consists mostly of this material. Target after removing from furnace is shown in Fig. 4.5b. Afterwards, the target is broken down to a powder again and whole process from milling is repeated. To even further improve the target quality, the calcining can be repeated several times. The last baking is called sintering and the temperature in this case is 1350 °C. This process is longer than calcining and lasts about ten hours. The final product is depicted in Fig. 4.5c and its XRD pattern is in Fig. 4.6. The black color of the target suggests the oxygen vacancies in the garnet structure. Before first deposition, the target is mechanically polished and preablated with the laser.

(a) Raw (b) Calcined (c) Sintered

Figure 4.5: Pictures of PLD targets after different steps of fabrication. (a) Raw mixture of powders after ball milling and drying pressed into the shape of a target. (b) Target after first calcining. Green color indicates formation of perovskite structure. (c) Target after sintering. The black color is caused by oxygen vacancies caused by shortage of oxygen in the furnace during the process at high (1350 $°C$) temperatures.

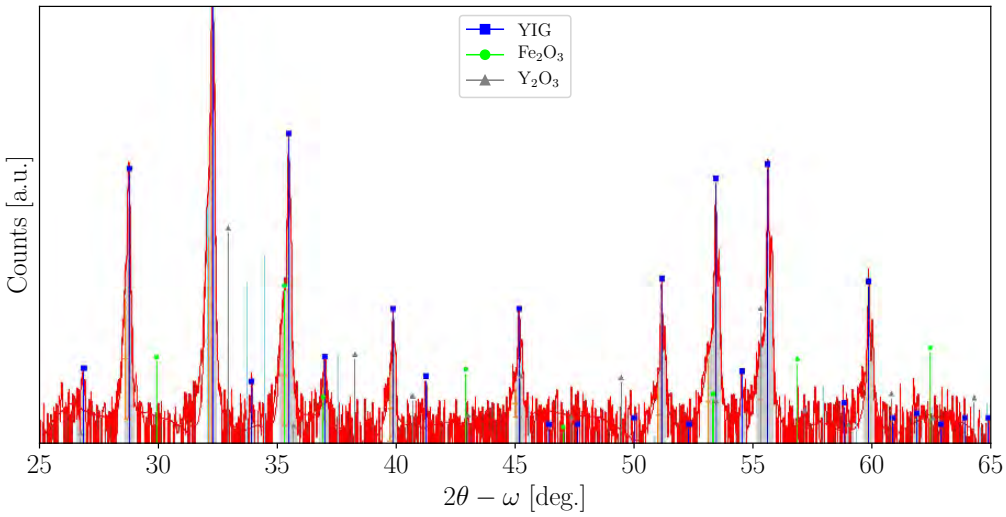

Figure 4.6: XRD pattern of fabricated polycrystalline YIG target. Blue squares mark garnet peaks. Green circles and grey triangles show positions of phases of raw materials that are not present.

5. X-ray diffraction

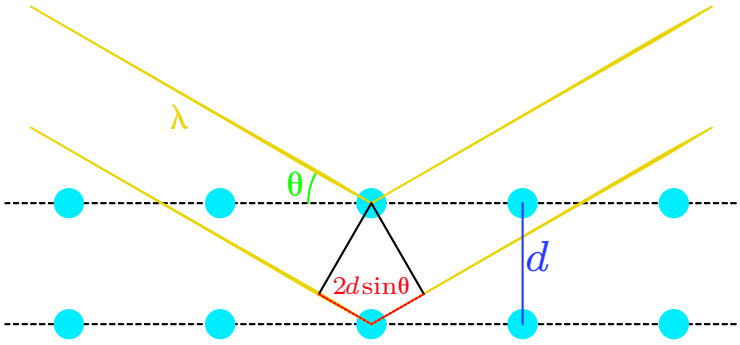

Figure 5.1: Schematic of Bragg condition.

Information about crystallographic structure is the first information one seek to ensure quality of prepared sample. Since the information about position of every single atom in a film is not available, one has to seek other ways to describe the structure. It was the periodicity of the system what allowed to L. Bragg and his father W. H. Bragg to observer patterns of reflected X-rays. They further investigated that these patterns dependent on crystal orientation and wavelength of used radiation. They managed to model these patterns using standard diffraction when they placed series of gratings on each other. The final Bragg's law

$$2d \sin\theta = n\lambda, \tag{5.1}$$

where d is the distance between atoms, θ the angle of incidence, n an integer and λ the used wavelength, is a base equation of XRD describing condition, that has to be met to observer diffraction peak at specific angle. Graphical visualization is depicted in Fig. 5.1. Observation of diffraction maxima allows reconstruction of crystallographic structure through various scans. We will focus on techniques used on thin films grown on well oriented substrate.

The $2\theta-\omega$ (sometimes $\theta-2\theta$) scan is basic symmetrical scan for probing crystallographic planes parallel to the surface of the sample. In the case of epitaxial film on cubic crystal, the most visible features are narrow intensive peaks originating from used substrate. The signal from the film can be found in the vicinity of these peaks as much smaller and broader features. In case of very small lattice mismatch, one might observe only shoulder on the substrate peak. If the film was amorphous, there would be nothing to observe. In the case of truly epitaxial film, diffraction scan shows series of peaks appearing on both side of the film peak. These peaks are called thickness fringes and originate from interference of reflected X-rays from interface between the film and the substrate. These fringes can be used for calculation of thickness of the film. The position on the film peak determines the lattice constant of the film in the direction perpendicular to the surface.

There are several scenarios, how a film grows on top of a substrate. Considering the film and the substrate are from different material and therefore they

have different lattice constant, their combination occur in two ways as shown in Fig. 5.2. Since the substrate consist of significantly higher number of atoms, atomic forces spreading to the film have huge influence on the position of its atoms. The worst case scenario is so high lattice mismatch between the substrate and the film materials, that resulting forces will not allow atoms to sit in proper places and the resulting film will be amorphous. On the other hand, when the lattice mismatch is near zero, position of atoms in the plane of surface is strongly determined by the position of substrate atoms and atomic layers of the film mach exactly the substrate. This case is called fully strained layer. If the film material tends to form a cubic crystal, one can expect slight tetragonal distortion since the volume of unit cell must remain the same. Somewhere between these two cases is fully relaxed film. Lattice layers of substrate and film match only at several unit cells, but interplay of atomic forces still does not break the crystal. In real sample, the actual state of crystal depends on many parameters. For example, thicker films will at some point relax, because influence of substrate lowers further away from the interface.

To determine the strain state of a the film, one needs information about atomic layers spacing in more directions. This information cannot be obtained from symmetrical scan and therefore asymmetrical scans are required. Since this thesis is not focused on structural analysis, their theory will not be further explained. Through performing series of these scans, one can map part of the reciprocal space around the substrate peak. This reciprocal space map (RSM) carries various information. For the rest of this work, only the information about the strain state will be required. That can be determined by comparing the position of the substrate and the film peak. If they lay on the same in-plane reciprocal coordinate q_x, there is lattice match in that direction as shown in Fig. 5.2 and the film is therefore fully strained. Any deviation from this position points to the relaxation.

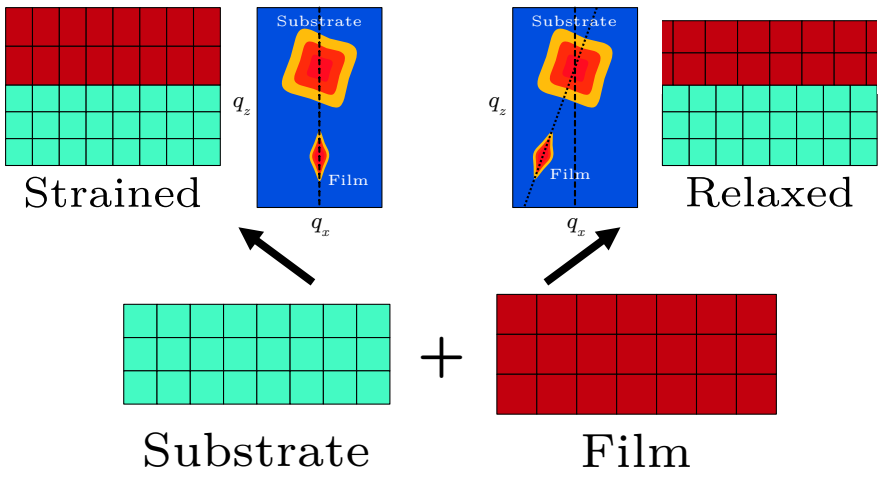

Figure 5.2: Schematic of formation of fully strained and relaxed films and their corresponding RSMs. Strained film is indicated by in-plane lattice matching marked by dashed line in q_x.

6. Magnetometry

Measurements of magnetization of samples presented in this work were performed with vibrating sample magnetometer (VSM). This device was invented in 1955 at MIT Lincoln Laboratory and allows measurement of magnetization of sample while applying external magnetic field. The original design consists of two sets of coils oriented along the same axis as depicted in Fig. 6.1a. The first pairs is used for application of external field. The second set senses the magnetization of studied sample. Maxwell's equation 1.2 require change of magnetic field to induce electrical current in sense coils. That is achieved by vibrating with the sample holder. Sample on the top of the holder then makes well defined motion of steady frequency. Therefore, detection coil picks up AC signal of the same frequency. The calibration of signal is performed by measuring of sample of well defined magnetization, for example a nickel disk.

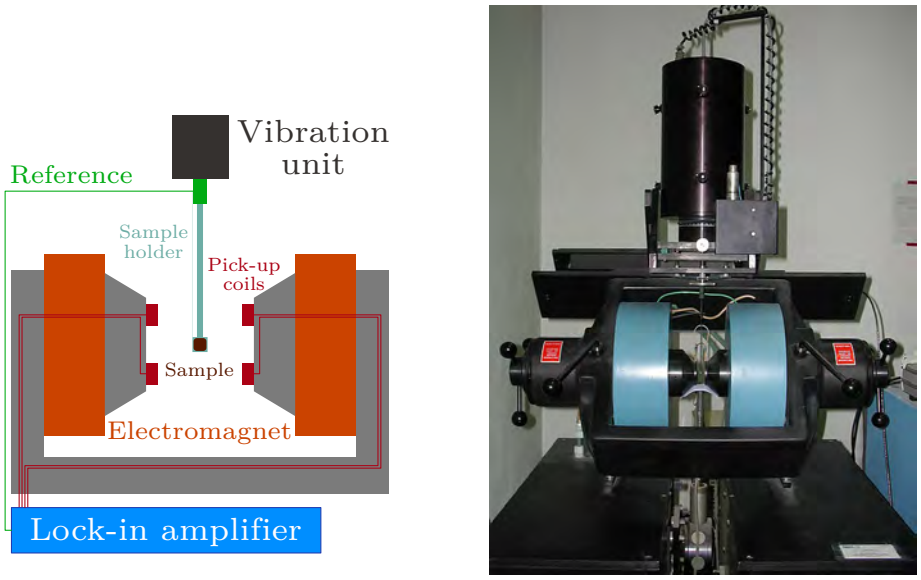

(a) Schematic (b) Picture

Figure 6.1: (a) Schematic of VSM showing positions of the coils. Sample is positioned in their center on sample holder, that is inserted in vibrating unit. (b) Picture of VSM used for the measurements.

7. Optical and magneto-optical characterization

7.1 Measured quantities

Optics is very old discipline and with that comes one very unfortunate situation. Throughout the time, various quantities and sign conventions were introduced to describe the experimental measurements. Chapter 1.2 introduced quantities used for description of polarization at specific state. However, these parameters are not convenient and hence not commonly used for description of its change. Next few paragraphs contain definitions of the quantities used in this work and briefly explain their meaning.

Spectroscopic ellipsometry works with change of ratio between s and p waves; therefore, the quantity it uses for its description is defined as

$$\rho = \frac{r_{pp}}{r_{ss}} = \tan\Psi \cdot \exp\{i\Delta\}. \tag{7.1}$$

Parameters r_{pp} and r_{ss} were introduced before as Jones reflection coefficients. Since ρ is a complex number, the second part of the equation writes ρ, that is a complex number, in its geometrical representation using new parameters Ψ and Δ. These parameters have no dimension and through this work their notation is in degrees rather than radians.

The field of magneto-optics focuses on conversion of one polarity to another. The presence of magnetic field also introduces another naming challenge due to various possible configurations. The effects are distinguished based on the way light interacts with the system by their corresponding discoverers. This means that effects in transmission are called Faraday and the ones in reflection are named Kerr. It is worth mentioning, that these names are commonly used only for effects linear in magnetization. Therefore, there is only one geometry for Faraday effect with magnetization pointing along the direction of light propagation. In the case of the Kerr effect, there are two other parameters for its exact determination. For orientation of magnetic field, it is common to use naming already introduced in previous chapter and depicted in Fig. 3.2. The second parameter is the incident polarization, which can be either s or p wave. This is very significant especially for longitudinal effect, where these two scenarios can differ in more than one order of magnitude of effect. This work contains only measurements of polar Kerr and Faraday effect at normal or nearly normal incidence. Due to symmetry of these effects, there is no change with polarization of incident light. The distinguishing of s and p waves also looses in this geometry its meaning.

The quantity used for description of magneto-optical effect in called magneto-optical angle Φ. An example of its definition for the case of the polar Kerr effect is

$$\Phi_{Kp} = \frac{r_{sp}}{r_{pp}}. \tag{7.2}$$

This angle is usually very small number and therefore it is common to use further

approximation

$$\Phi_{Kp} \approx \theta_{Kp} - i\epsilon_{Kp}, \tag{7.3}$$

where θ_{Kp} denotes the Kerr rotation and ϵ_{Kp} the Kerr ellipticity. These quantities have also the dimension of angle and in further text, usage of degrees instead of radians is favored.

Finally, when speaking about Faraday effect, it is common to use magnetic circular dichroism (MCD) instead of ellipticity. These two quantities; however, differ only in the multiplication factor of -1.

Another attribute of material used in this work is Figure of Merit (FoM), that is defined as Faraday rotation over optical absorption. It is a parameter often used to describe material suitable for optical rotator. It is due to its description of modulation performance while taking in account the lost signal as well. Motivation is simple, since excellent rotator is useless if the information is lost during the process.

The value of FoM is calculated, using unit deg./dB, via definition

$$\mathrm{FoM} = \frac{\theta_F}{10\log_{10} e\alpha} \approx \frac{\theta_F}{4.343\alpha}, \tag{7.4}$$

where θ_F is the Faraday rotation and α the optical absorption. Optical absorption can be calculated using permittivity through

$$\alpha = \frac{4\pi\sqrt{2(\Re(\varepsilon_1) + |\varepsilon_1|)}}{\lambda\Im(\varepsilon_1)}. \tag{7.5}$$

Finally, inserting this equation with $\lambda = \frac{hc_0}{E}$ into 7.4 yields

$$\mathrm{FoM} = \frac{\hbar c_0}{20\sqrt{2}\log_{10} e} \frac{\theta_F \Im(\varepsilon_1)}{E\sqrt{\Re(\varepsilon_1) + |\varepsilon_1|}} \approx 16.070 \frac{\theta_F \Im(\varepsilon_1)}{E\sqrt{\Re(\varepsilon_1) + |\varepsilon_1|}}, \tag{7.6}$$

where $\hbar$ is the reduced Planck constant and E the photon energy.

7.2 Spectroscopic ellipsometry

All the ellipsometric measurements presented throughout this work were performed on commercially available system Woollam RC2. This system is build on the modulation technique applying two rotating compensators. The compensators are rotating at angular speeds of ω_1 and ω_2, respectively. The mechanical rotation of compensators is kept synchronized at a ratio $p : q$ meaning

$$\omega_1 = p\omega,$$
$$\omega_2 = q\omega.$$

Periodical modulation of polarization leads to presence of desired quantities in measured signal at specific frequencies. With this configuration, all sixteen elements of Muller matrix can be extracted from the signal. Derivation of each element of Muller matrix is beyond the scope of this work, but it is explained in Ref. [30].

Synchronous operation of both compensators allows high accuracy of data acquisition in a very short time window. Furthermore, ability to measure the whole Muller matrix allows more advanced analysis than standard ellipsometry [31]. RC2 is equipped with two CCD detectors covering very wide spectral range from extended UV to near infrared (193 - 2500 nm). The spatial detector allows collection of the whole spectrum at once. The system also has various customization options like focusing probes (spot size 200 μm) or translation stage for spatial mapping of the sample.

Woollam company provides software for data processing and modeling. This program, called CompleteEASE, comes with various options for modelling optical response of layered structures. The simplest ones utilize Fresnel equations with tabulated values of refractive index for very precise determination of layer thickness. More advanced ones use phenomenological models described in chapter 3.3 and allow further study of the origin of optical response. Further information is well described in Ref. [32].

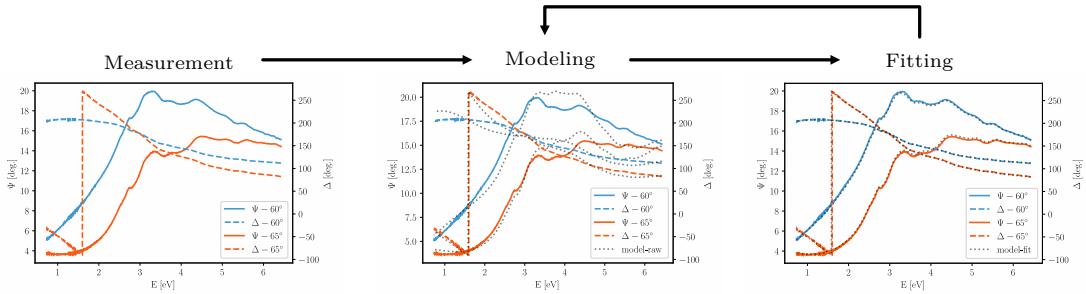

Figure 7.1: Schematic of ellipsometry data processing. The first charts depicts experimental data. The second chart shows comparison of the experimental data with predictions of used model. The last chart shows the agreement of experimental data with the model after the fitting procedure.

Modeling of measured ellipsometric angles Ψ and Δ consists of few simple steps depicted in Fig. 7.1. The experimental data are compared with prediction calculated from the model of studied structure. This model consists of optical properties and thicknesses for each layer of the sample. The starting model is usually based on knowledge obtained from other scientific methods or sample preparation. The precision of the model is further improved by varying its parameters. This process is recursively repeated until satisfactory match is reached. The final model provides information about layer thicknesses and optical properties. Furthermore, it can be extended to include surface roughness, inhomogeneities or other physical properties. Since the solution space grows significantly with each additional fitting parameter, it is vital to collect data from various angles of incidence and broad spectral range to decouple correlations between its parameters. The modelling procedure can be also provided with additional experimental measurements such as optical transmission.

7.3 Magneto-optical spectroscopy

The main instrument used throughout this work was magneto-optical spectrometer based on rotating analyzer technique. This setup has gone through many alternations and improvements through the years. This chapter will therefore describe its actual state and mention some of its changes with their motivation.

Concept

The signal on conventional detector is proportional to intensity of incident light; therefore, additional optical elements must be employed to introduce dependence on the polarization required for its measurement. The state of light as well as used optical elements are in this section described using Jones formalism that was introduced in chapter 1.3.

The purpose of an experimental setup is determination of change of polarization introduced by the sample rather than reading the actual polarization state. Therefore, its design focuses on finding of elements of Jones matrix of the sample. Depending on the geometry of an experiment, it can be either in reflection or transmission. Furthermore, the optical and magneto-optical response of the studied system is often strongly dependent on incident angle and photon energy of incoming light. Therefore, the result of the measurement can be complex function of angle and photon energy.

Nearly crossed polarizers technique

This simple technique demonstrates the minimal configuration required for the sensing of the change of polarization and expected dependencies observable in the signal.

Jones formalism cannot work with unpolarized light that is coming from the conventional lamps. Therefore, the starting point is considered the light source with polarizer right after its output. This polarizer can be positioned at an arbitrary angle ψ, measured from x axis and therefore the Jones vector right after it has the form

$$\vec{J} = \sqrt{I_0} \begin{bmatrix} \cos\psi \\ \sin\psi \end{bmatrix}. \tag{7.7}$$

Considering detector sensing this light, measured intensity is always I_0 independent on orientation of the polarizer. This shows that the detector is by itself insensitive to the polarization state of incident light. To introduce the polarization dependency, additional polarizer is introduced. Considering its position at angle χ, the Jones vector after passing through is written as

$$\vec{J} = \sqrt{I_0} \begin{bmatrix} \cos^2\chi & \sin\chi\cos\chi \\ \sin\chi\cos\chi & \sin^2\chi \end{bmatrix} \begin{bmatrix} \cos\psi \\ \sin\psi \end{bmatrix} = \begin{bmatrix} \cos\chi(\cos\chi\cos\psi + \sin\chi\sin\psi) \\ \sin\chi(\cos\chi\cos\psi + \sin\chi\sin\psi) \end{bmatrix} \tag{7.8}$$

Intensity calculated from this vector after use of trigonometric relations equals to

$$I = I_0 \cos^2(\psi - \chi) \tag{7.9}$$

The measured intensity depends on the relative position of the polarizers. Therefore, without prejudice to generality, the first polarizer can be considered fixed

along the x axis ($\psi = 0$). With notation using $\alpha = \chi + 90°$ the intensity reduces to

$$I = I_0 \sin^2 \alpha, \tag{7.10}$$

that is also known as Malus's law. The change of measured signal can be shown by inserting polarization rotator between the polarizers. With introduced rotation by angle ϕ the intensity get a form

$$I = I_0 \sin^2 (\alpha + \phi) \tag{7.11}$$

The system is sensitive to change of polarization caused by additional element and hence could be used for its measurement. The rotator can be replaced by general reflection matrix of sample to prove this point. After the substitution, the intensity is written as

$$I = I_0 \left(r_{ps}^2 \cos^2(\alpha) + \Re(r_{ps} r_{ss}) \sin(2\alpha) + r_{ss}^2 \sin^2(\alpha) \right) = \tag{7.12}$$

$$= I_0 R \left(|\Phi_{Ks}|^2 \cos(\alpha) + \Re(\Phi_{Ks}) \sin(2\alpha) + \sin^2(\alpha) \right), \tag{7.13}$$

where the definition of Kerr angle Φ_{Ks} and reflection coefficient $R = r_{ss}^2$ were used in the second part of the equation. This relation contains dependence on $\Re(\Phi_{Ks})$ only and therefore the measurement does not contain complete information about change of polarization caused by the sample. This can be solved by additional modulation of the polarization using waveplate of retardance δ. Furthermore, additional approximations can be used. Φ is general very small number and therefore the term containing $|\Phi|^2$ can be neglected. It is also convenient to use notation showed in 7.3. These adjustments simplify the relation for intensity to

$$I = I_0 R \left(\sin^2 \alpha + (\theta \cos \delta - \epsilon \sin \delta) \sin 2\alpha \right). \tag{7.14}$$

This equation shows, that complete information about magneto-optical response is obtained from two measurements with different δ. The obvious choice is $\delta = 0$ when only the Kerr rotation is measured. Without the prejudice to generality, this choice will be used in the further text.

To simplify the usage of this technique and required calibration, α is chosen very small (hence nearly crossed polarizers). This choice allows further approximations $\sin^2(\alpha) \approx 0$ and $\sin \alpha \approx \alpha$. Moreover, in the real measurement setup, the transmission of used optical elements cannot be considered perfect anymore. Result of these steps is intensity on the detector with linear dependence on magneto-optical effect

$$I = TR\alpha\theta = A\theta, \tag{7.15}$$

where the reflection of sample R, the transmission of optical elements T and choice of α were put into single constant A. This constant is determined through calibration procedure described by

$$A = \frac{I(\alpha + \varsigma) - I(\alpha)}{\varsigma}, \tag{7.16}$$

where ς is small known angle.

This technique was used for measurements of magnetic hysteresis loops of Faraday rotation presented in chapters 8.4 and 10.1.

Rotating analyzer technique

It is possible to use the equation 7.14 without further approximation and utilize the dependency on the α. This approach is more measurement intensive, but it has been proved to provide very precise results [33, 34]. In this case, instead of keeping α fixed, series of measurements for different angles α are performed. Obtained angular dependency is fitted with the function based on 7.14

$$I = A\sin^2(\alpha) + B\sin(2\alpha) + C, \tag{7.17}$$

where C was introduced to include the dark current in the detector and effect of the depolarization in the system. The fitted function can be viewed as revolution of signal in sinus functions. Therefore, the fitted parameters correspond to Fourier coefficients of orthogonal functions. Therefore, all parasitic signals that do not have angular dependency on α are filtered out. The measurement does not require any additional calibration, since the magneto-optical effect is

$$\Phi = \frac{B}{A} \tag{7.18}$$

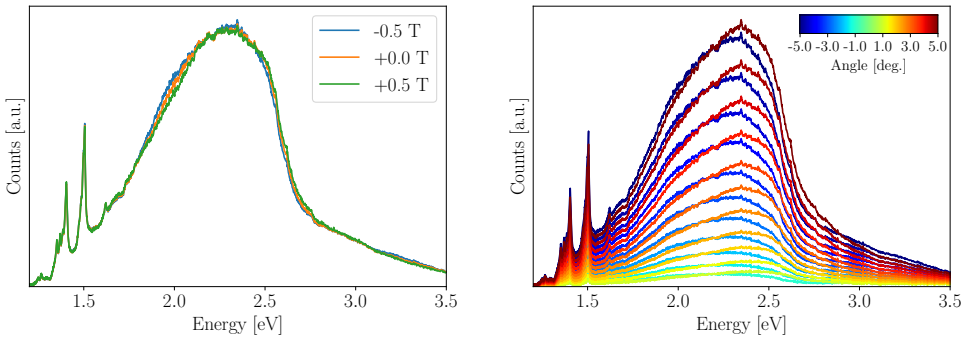

(a) Change of Magnetic Field. (b) Change of position of Analyser.

Figure 7.2: Raw signal on the detector during (a) different applied external magnetic fields and (b) different positions of analyzer at field of 0.5 T.

Signal fitting

For better understanding of this technique next few paragraphs present an example of the measured signal and its processing. It is vital to keep in mind, that measured angles are very small. Therefore, the change of magnetization of the sample also leads to very small change of intensity on the detector. This can be well seen in Fig. 7.2a. Even though some regions of spectra exhibit relatively large change, the difference is mostly in the order of ‰. The whole measurement set for field of 0.5 T is shown in Fig. 7.2b. The asymmetry on spectra demonstrates the presence of other contributions into change of polarization state that show strong spectral dependence. These effect are further removed through usage of symmetry of magneto-optical effects in magnetization. The fitting procedure is applied on data set shown in Fig. 7.3a that depicts acquired data for 2 eV. This figure demonstrates the agreement of the fit of equation 7.17 with experimental

data for various applied magnetic fields. This procedure is performed for every measured pixel resulting in the spectrum. As the last step, the symmetry of the linear magneto-optical effect in magnetization is used

$$\Phi(\vec{B}) = \frac{\varpi(\vec{B}) - \varpi(-\vec{B})}{2}, \tag{7.19}$$

where $\varpi(B)$ denotes angle measured at the external magnetic field of B. The final spectrum of Faraday rotation is shown in Fig. 7.3b.

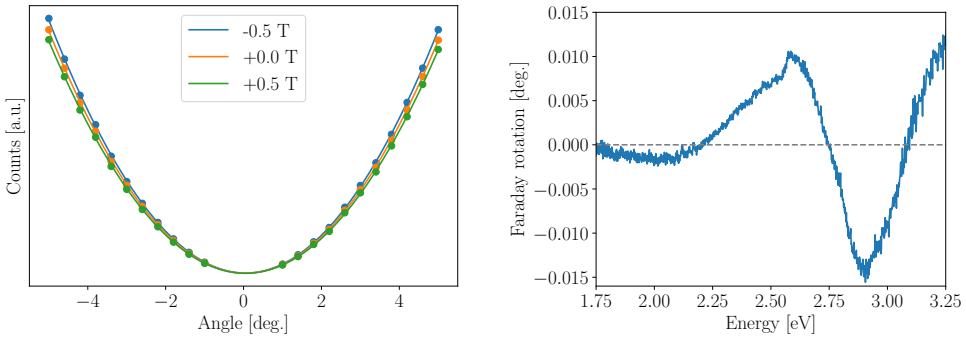

(a) Raw data for 2 eV. (b) Spectrum of Faraday rotation.

Figure 7.3: (a) Data used for fitting of magneto-optical effect at 2 eV at different applied magnetic fields. (b) Resulting spectral dependence of Faraday rotation from fitting of the raw data.

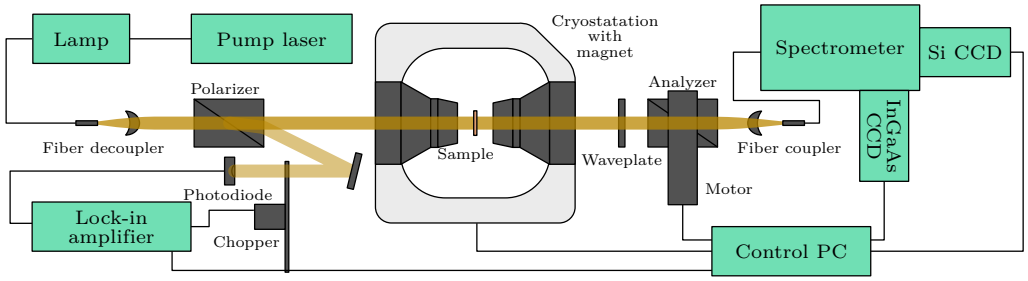

Figure 7.4: Schematic of magneto-optical spectrometer. Starting from left, it consists of light source, focusing optics, polarizer, cryostat with electromagnet with sample inside, waveplate, rotating analyzer, collection optics and spectrometer. Photodiode in the system is used for the correction of lamp intensity fluctuations.

Experimental realization

Schematic of the system is shown in Fig. 7.4. Starting from left side, we can divide the setup into three block: light source, sample and detection part.

Light source

The choice of optical source for the setup is based on two key aspects it has to satisfy. It is the desired spectral coverage and required time stability. In many

scenarios, multiple light sources has to be combined to fulfil both aspect in the whole desired spectral range. Optical elements used in the setup must be also taken in account, since their transmission may further limit measurable spectral region. The main source for the setup is EQ-99XFC laser driven light source from Energetiq (Hamamatsu company). The concept of this lamp is quite simple. It adds up on the Xe arc lamp. However, instead of creating plasma through current running through the bulb, it focuses continuous wave laser beam in the middle of the electrodes. Resulting plasma has even greater brightness and it is well localized. The lamp has significantly higher output power than regular arc lamp, longer life time and superior spectral shape that lacks specific peaks common to arc lamps. The light is coupled into optical fibre and delivered right into the system. There is series of optical elements ensuring good collimation and further focusing beam onto the sample. These elements are strictly made from UV fused silica that have good transmission in UV region up to 190 nm. Last optical element of the block is a prism polarizer. An α-BBO crystal in rochon configuration provides excellent transmission in wide spectral range reaching to UV region and also provides high divergence of outputting polarized beams. The direct beam continues towards the sample. The second one is after modulation collected with photodiode and used for measurement of lamp stability and correction of its fluctuation. Even though overall stability of used lamp is declared below 0.5 %, measurement of stability over longer time scales show sudden jumps of intensity giving peak to peak error of almost 3 % that had significant influence on measurements. Therefore, correction with photodiode sensing the secondary beam was introduced. This led to significant reduction of signal fluctuation as shown in Fig. 7.5.

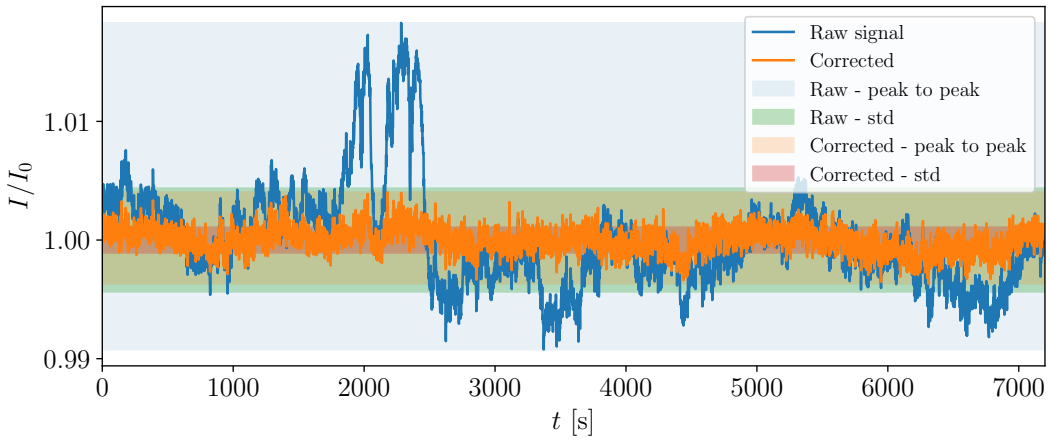

Figure 7.5: Chart of signal stability on the detector, before and after correction using the photodiode in the system. Colored areas mark the errors of the measurement.

Sample

Light coming into this block is already well focused on the sample and linearly polarized. The schematic in Fig. 7.4 shows the configuration for measurement

of Faraday effect; however, other geometries can be also measured. The sample itself is placed in cryostation from Montana Instruments that is equipped with its own electromagnet. The cryostat allows temperature control of the sample down to 10 K, while providing external magnetic field. This magnet allows application of field in only one direction; therefore, the setup has to be slightly modified for the measurement at different geometries as shown in Fig. 7.6. The applied field depends on used gap in the chamber and can go up to 940 mT. Such high field exceeds beyond the chamber and induce birefringence on other optical elements in the vicinity. Therefore, it is vital to keep them in proper distance to minimize this effect. Unfortunately, chamber windows are in close proximity of the magnet. They can be removed for measurements at room temperature, but otherwise they have to be accounted for.

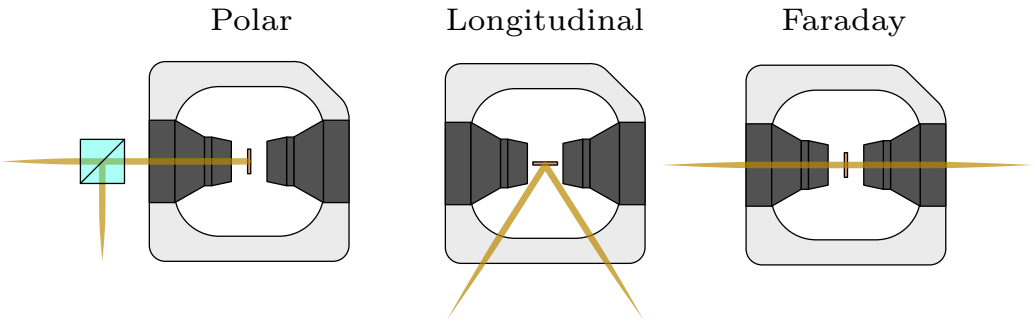

Figure 7.6: Schematics of optical paths around the cryostat for the measurement of different magneto-optical effects.

Detection part

The beam is further processed after leaving the sample space. Optionally, there is a waveplate for measurement of ellipticity. Afterwards, there is another polarizing prism placed in rotating stage. The system alters between positioning systems from Thorlabs and Owis company that both guarantee precision of few μdegree. Finally, there is coupling optics and fiber leading to spectrometer. The spectrometers used for measurement are from Andor company (Shamrock 500i, 328i). These highly automated systems equipped with CCD cameras allow measurement of various spectral window depending on used grating. The most commonly used grating cover spectral region of Si (190 - 1100 nm) in four measurements with spectral resolution below $\frac{1}{3}$nm. In addition, Shamrock 500i is equipped with second InGaAs camera that allows measurements down to 2500 nm.

Part IV

Experimental results

Due to wide spread of studied problematics, this part is split into four chapters based on studied problematic. The first chapter focuses on optimization of growth process and transfer to Si substrate of Ce and Bi doped YIG with the aim for improvement of their FoM and therefore applicability in the devices. Next chapter presents the analysis of new garnet films prepared with perpendicular magnetic anisotropy. Even thought this work focuses of their optical and magneto-optical properties, they were also used in other spintronic studies [35, 36, 37]. The third chapter contains the study of temperature dependence of physical properties of presented garnets. Specifically, it explains possibility of reorientation of magnetic anisotropy in the thin films and magneto-optical response near the compensation temperature. The last chapter concludes with demonstration of modeling of magneto-optical spectra of $Tb_3Fe_5O_{12}$. It starts with building of the macroscopic model and demonstration of its performance under various physical conditions. Lastly, the model is used for study behavior of magnetic sublattices and their contribution into magneto-optical response.

8. Garnets with high FoM for photonic applications

8.1 $Bi_xY_{3-x}Fe_5O_{12}$ on $Gd_3Ga_5O_{12}$

One of the materials with the highest magneto-optical response remains even decades after its first synthesis bismuth doped yittrium iron garnet (Bi:YIG). In this material, introduction of this heavy element leads to significant increase of spin-orbit coupling resulting in over ten times higher magneto-optical response than in pure YIG [19]. Unfortunately preparation of layers with high Bi content still remains a challenge. This section covers films with up to full Bi substitution prepared by MOD.

Samples

For the purpose of the study of Bi content in the films, four films of $Bi_xY_{3-x}Fe_5O_{12}$ with concentrations (x = 1.5, 2, 2.5, 3) were prepared using metallo-organic decomposition described in detail in chapter 4.2. All films were grown on gadolinium galium garnet ($Gd_3Ga_5O_{12}$) (GGG) substrates with (100) orientation. Carboxylates solution used for the deposition had concentration of 3-4 %. It was spin-coated on substrates with 3000 rpm for the duration of one minute [38]. This process was followed by drying at 100 °C for 30 minutes. Decomposition was performed at 450 °C for another 30 minutes resulting in amorphous oxide layer. This process was repeated 4 to 5 times to achieve desired film thickness. Nominal thicknesses of studied films were between 160 and 200 nm. Finally, samples were annealed at 700 °C for duration of 3 hours to crystallize the films.

Magneto-optical properties

Spectra of polar magneto-optical Kerr effect (MOKE) are shown in Fig. 8.1. The region below 3 eV shows the effect of interference within the films caused by their transparency at these energies. Different periodicity of the oscillations is due to different thicknesses of the films. Besides, the spectra are dominated by two maxima at 3.4 and 4.0 eV in rotation, and at 3.3 and 4.4 eV in ellipticity. These features are characteristic for Bi:YIG [20, 39]. Beyond that, the increase of Bi content further magnifies the effect of spin-orbit coupling resulting in increase of amplitude of magneto-optical Kerr effect. Furthermore, there is no change of spectral shape other than the interference that would point to changes in electronic structure.

Spectra of Faraday effect depicted in Fig. 8.2 show significance of Bi doping near the band gap. Going from half substitution of Bi up to fully substituted film results in about three times higher magneto-optical response. Similarly to polar MOKE, there is no change of spectral shape caused by different content of Bi. The measurements in transmission geometry are not so influenced by the effect of the interference and therefore, it was not observed in the measured spectra. Magnetic hysteresis loops of Faraday rotation depicted in Fig. 8.3 show negligible

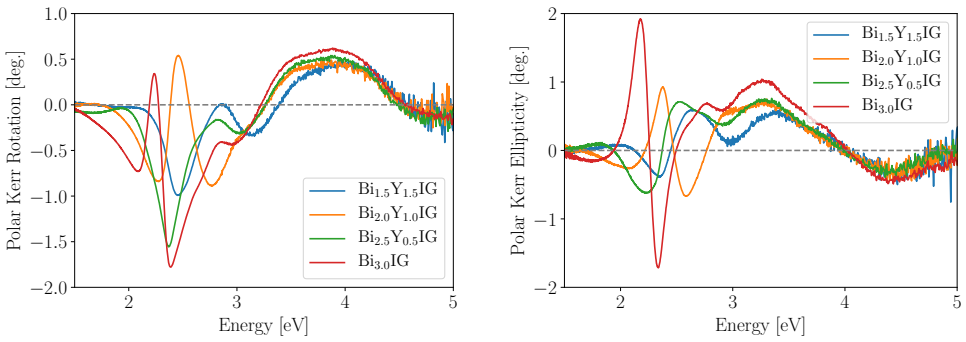

(a) Polar Kerr rotation (b) Polar Kerr ellipticity

Figure 8.1: Spectral dependence of polar MOKE of Bi:YIG films with various Bi content on GGG substrates.

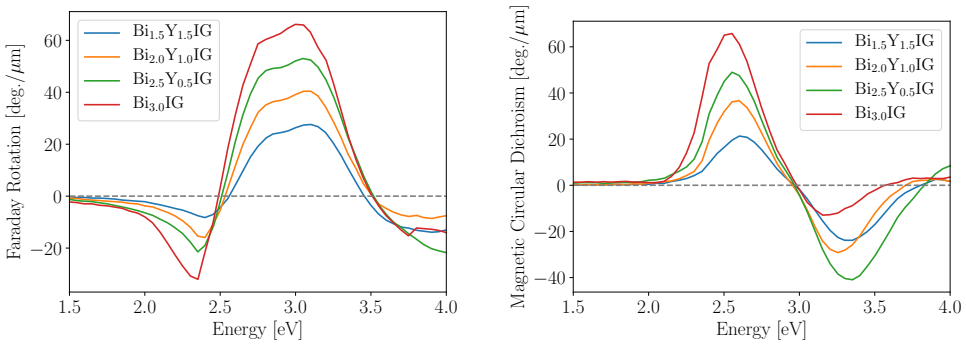

(a) Faraday rotation (b) MCD

Figure 8.2: Spectral dependence of Faraday (a) rotation and (b) MCD of Bi:YIG films with various Bi content on GGG substrates.

change of magnetic anisotropy caused by higher concentration of Bi. Moreover, all the films exhibit out-of-plane hard magnetization axis.

In conclusion, the garnet films deposited by MOD have excellent magneto-optical response, that is comparable to other deposition techniques [20, 39]. Therefore, MOD presents a very promising technique for further industrial implementation of garnets due to its simplicity and possible scalability. At last, MOD can be used for preparation of fully substituted BiIG, that is not possible by other techniques like sputtering or PLD.

8.2 $Ce_1Y_2Fe_5O_{12}$ on $Gd_3Ga_5O_{12}$

Garnets as dielectric materials show very low absorption at telecommunication wavelength 1550 nm that even exceeds the properties of silicon. Unfortunately, YIG has only weak magneto-optical response in near IR region. However, this can be improved by selective doping. In this section, Ce is used for its specific transition in this spectral region.

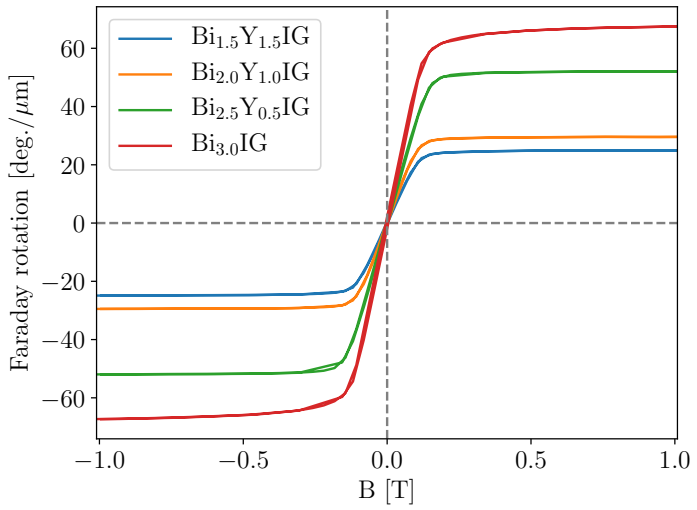

Figure 8.3: Magnetic hysteresis loops of Faraday rotation of Bi:YIG films with various Bi content on GGG substrates measured at 3 eV.

Samples

Films of cerium doped yittrium iron garnet (Ce:YIG) were grown on double-side polished GGG substrates with (100), (110) and (111) orientations using PLD described in chapter 4.3. The target used for the growth had composition of $Ce_1Y_2Fe_5O_{12}$ based on ratio of raw materials used for its fabrication. The base pressure and oxygen pressure during the deposition were $5 \cdot 10^{-6}$ and 5 mTorr, respectively. The laser was running with repetition frequency of 10 Hz and pulse power of 400 mJ. During the deposition, the substrates were kept at temperature of 650°C and cooling rate afterward was $10°C \cdot min^{-1}$. Resulting films were 80 nm thick as was determined by X-ray reflectivity (XRR) and confirmed with spectroscopic ellipsometry.

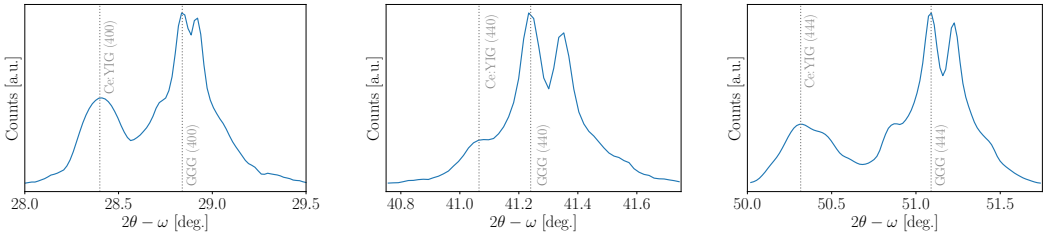

(a) GGG (100) (b) GGG (110) (c) GGG (111)

Figure 8.4: XRD patterns of Ce:YIG (80 nm) films on (a) GGG (100), (b) GGG (110), and (c) GGG (111) substrates. Y_2O_3 or CeO_2 peaks were not found. All the films are single phase garnets. Substrate and film peaks are indicated by dashed lines.

Structural properties

Structural analysis was performed by means of XRD. Figure 8.4 shows $2\theta - \omega$ scans for all substrate orientations. One can see, that peak separation between the film and the substrate is less than 0.5°, hence the lattice constants in out-of-plane direction were very similar. Broader diffraction peak of film on (110) substrate orientation suggested its lower crystallographic quality. In general, XRD patterns and therefore crystallinity was very similar to previously reported observations [40]. There was no evidence of secondary phases.

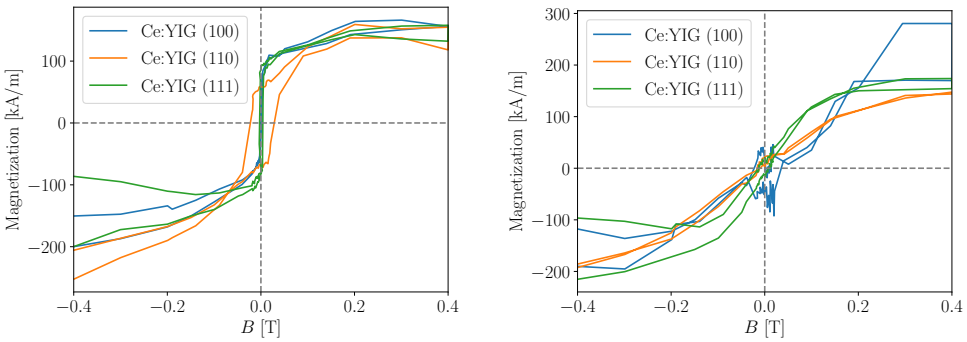

(a) In-plane (b) Out-of-plane

Figure 8.5: Room temperature magnetic hysteresis loops of Ce:YIG (80 nm) films on GGG (100), GGG (110), and GGG (111) substrates. Field was applied (a) in-plane and (b) out-of-plane to the film plane. All films exhibit in-plane magnetization easy-axis.

Magnetic properties

Measurements of magnetization loops are depicted in Fig. 8.5. The films showed saturation magnetization of $M_S = (150 \pm 15)$ kA/m that is consistent with previous reports [41, 42]. Noise in the measurements originated from high paramagnetic contribution of substrate that was subtracted. Nevertheless, the magnetization hard-axis was clearly along the out-of-plane direction and the easy-axis lies in-plane of the sample. Saturation field highly depended on substrate orientation and ranges between 0.2 and 0.8 T, which was estimated from extrapolation of measured data. More detailed analysis is shown in paragraph about magneto-optical properties. The film on GGG (110) showed for in-plane magnetization significantly higher coercivity and different shape that was caused by pinning of domain wall motion. This is in agreement with lower crystallographic quality of the sample causing pinning of domain wall on defects.

Furthermore, detailed angular dependency of magnetic properties was measured as shown in Fig. 8.6. The direction of easy magnetization axis followed the symmetry of the crystal and hence there were hints of 4-fold and 2-fold rotation symmetry in case of (100) and (110) substrate orientation, respectively. The film on GGG (111) was in-plane isotropic.

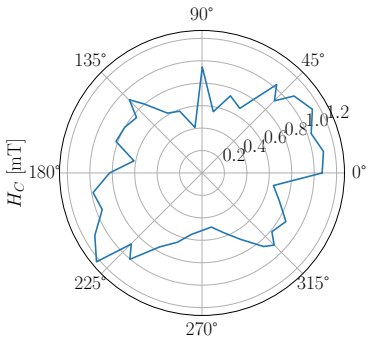

(a) In-plane H_C of Ce:YIG (100)

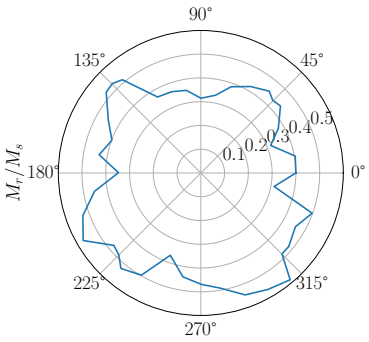

(b) In-plane M_r/M_S of Ce:YIG (100)

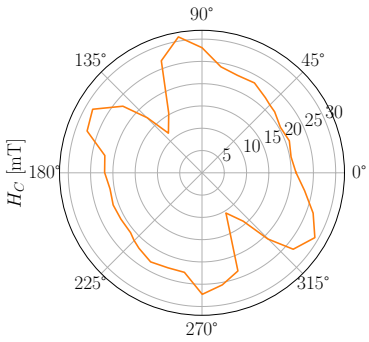

(c) In-plane H_C of Ce:YIG (110)

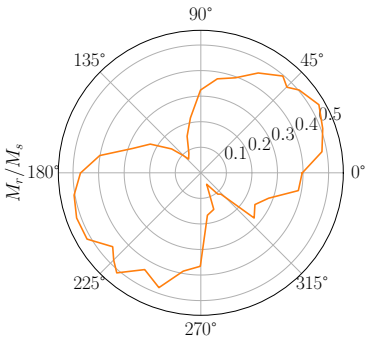

(d) In-plane M_r/M_S of Ce:YIG (110)

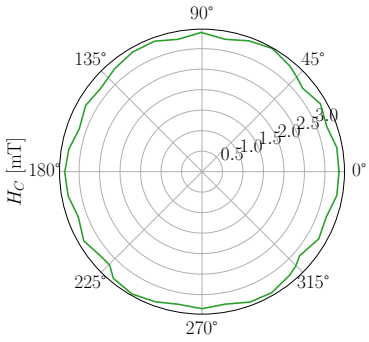

(e) In-plane H_C of Ce:YIG (111)

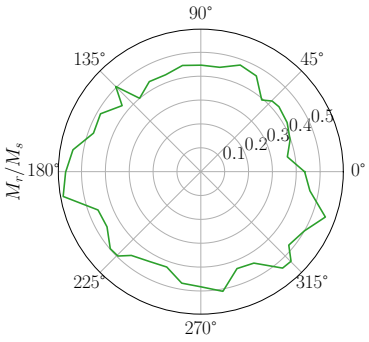

(f) In-plane M_r/M_S of Ce:YIG (111)

Figure 8.6: (a, c, e) Angular dependence of in-plane H_C for Ce:YIG (80 nm) on GGG (100), GGG (110), and GGG (111). (b, d, f) Angular dependence of in-plane squareness (defined as remanence over saturation; M_r/M_S) of Ce:YIG (80 nm) on GGG (100), GGG (110), and GGG (111). The film on GGG (100) shows 4-fold symmetry, the film on GGG (110) shows 2-fold symmetry, and the film of GGG (111) is isotropic.

Optical properties

Optical transmission of samples before and after the deposition process was measured as shown in Fig. 8.19. All substrates showed the same bandgap of $E_g = 5.344$ eV. GGG also had sharp absorption peaks at E = 4.504 eV, 4.035 eV, 3.972 eV due to intrinsic electronic transitions of Gd. These absorption peaks belong to the 4f transitions of Gd^{3+} ions from the ^8S ground state to ^6I, $^6P_{5/2}$ and $^6P_{7/2}$, respectively [43, 44]. These energy transitions originate from spin-orbit

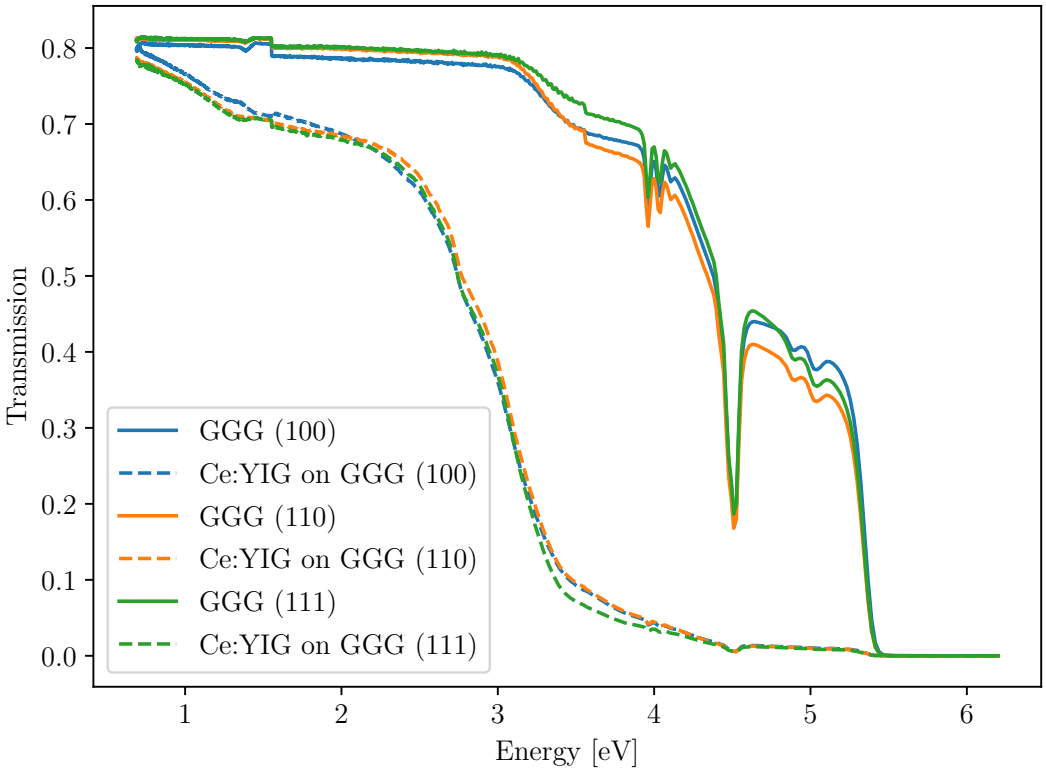

Figure 8.7: Room temperature optical transmission in visible and near IR spectral region of Ce:YIG (80 nm) films on GGG (100), GGG (110), and GGG (111) substrates. Absorption peaks of the GGG substrates near 4.504 eV, 4.035 eV, and 3.972 eV originate from the intrinsic electronic transitions of Gd^{3+} ions (from the ^8S ground state to ^6I, $^6P_{5/2}$ and $^6P_{7/2}$). Step near 1.5 eV is due to change of the detector.

and crystal field splitting. The transmission spectra indicate that Ce:YIG has an indirect band-gap similar to GGG, but with a stronger absorption tail reaching into the visible region. There is also a weak but non-zero difference between the absorption of substrates with different orientations.

The spectral dependencies of the diagonal term of permittivity tensor ε_1 obtained from spectroscopic ellipsometry in combination with Fourier transmission measurements in infrared region are shown in Fig. 8.8. The spectra are similar to the ones obtained for YIG bulk single crystals as well as thin films [45, 46, 47, 48]. The presence of Ce in the material has main influence in the spectral region between 1 and 2 eV. An elevated absorption around 1.4 eV is well seen in the imaginary part of ε_1 spectra. This absorption arises from intra-ionic electric-dipole transitions of the Ce^{3+} ions. These transitions are also observable in absorption spectra in Fig. 8.7.

Magneto-optical properties

Faraday magneto-optical spectra and hysteresis loops were measured with spectrometer based on the azimuth modulation technique [49]. Fig. 8.9 shows loops of Faraday rotation at wavelengths 780 nm (1.6 eV) and 1550 nm (0.8 eV). In

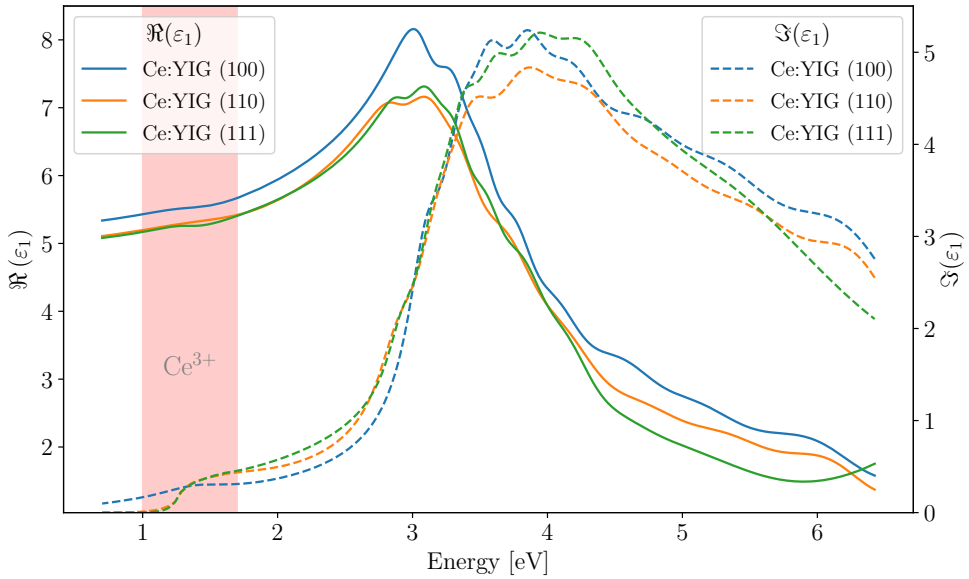

Figure 8.8: Spectral dependence of diagonal elements of permittivity tensor, ε_1, of Ce:YIG (80 nm) films on GGG (100), GGG (110), and GGG (111) substrates. Spectral region marked by red background indicates spectral features originating from intra-ionic electric-dipole transitions of the Ce^{3+} ions.

comparison to magnetometry measurements, these loops had much better ratio of signal originating from the films over substrate contributions. Therefore, they carry more precise information about magnetic anisotropy of the samples. The anisotropy fields for different substrate orientations were determined to be

$$\begin{aligned} H_K^{(100)} &= 0.8 \text{ T}, \\ H_K^{(110)} &= 0.5 \text{ T}, \\ H_K^{(111)} &= 0.2 \text{ T}. \end{aligned}$$

In comparison with previously reported values [50], sample on (111) oriented substrate is close to the expectation based on shape anisotropy. The other samples on the other hand exceed these values which suggest the influence of magnetocrystalline or magnetoelastic anisotropies. The amplitude of Faraday rotation is substantial considering the small thicknesses of the films. In numbers, the (111) film reached Farday rotation (FR) of 3 deg./μm at 780 nm (1.6 eV) and -0.58 deg./μm at 1550 nm (0.8 eV). These values exceed reports from both bulk and thin film Ce-substituted YIG [41, 51, 52, 53, 54, 55]. X-ray photoelectron spectroscopy (XPS) studies of similar systems demonstrated presence of atoms in different that 3+ oxidation states [36, 56]. These ions in the garnet structure could cause changes in the band structure shifting energies of specific transitions of Ce towards lower energies and therefore enhancing the magneto-optical effect at 0.8 eV as was observed.

The spectra of Faraday effect corrected for contributions of the substrates are depicted in Fig. 8.10. Observed spectral shape is similar to the one reported on thicker samples with high Ce^{3+} content [57, 58, 59]. Similarly to optical

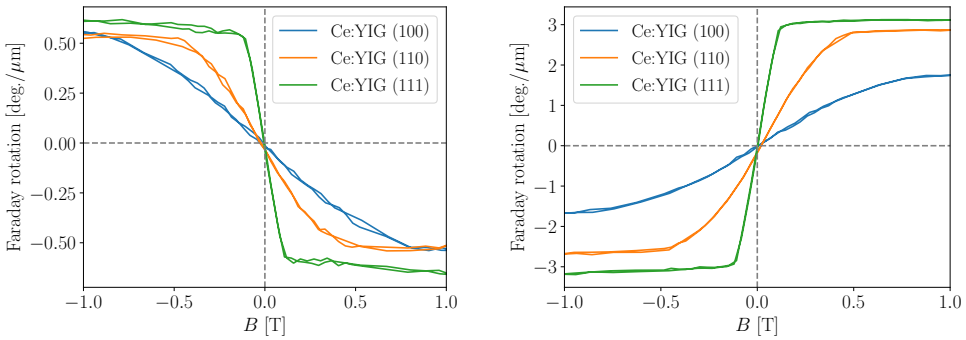

(a) 1550 nm (b) 780 nm

Figure 8.9: Room temperature Faraday rotation hysteresis loops of Ce:YIG (80 nm) films on GGG (100), GGG (110), and GGG (111) substrates measured at (a) 1.6 eV (780 nm), and (b) 0.8 eV (1550 nm).

measurements, the main observed spectroscopic feature is situated near 1.4 eV. Its origin is addressed to 4f-5d transition in Ce^{3+} [49, 60]. The enhancement of magneto-optical response in near-infrared region is originating in Ce^{3+}(4f)-Fe^{3+}(tetrahedral) electric dipole transition that is between 1 and 2 eV [59]. The rest of the spectra, especially visible region, is dominated by Fe^{3+} crystal-field transitions at both tetrahedral and octahedral sites that are well known from the studies of other garnets [20]. If we look at the comparison of amplitudes of Faraday effect among different substrate orientation, it is clearly visible, that (111) orientation exceeds the other two in the whole measured region.

Magneto-optical Kerr spectroscopy was performed using the setup described in section 7.3. Applied field of 1 T was applied to fully saturate the films. Results of these measurements are shown in Fig. 8.11. Large magneto-optical response below 2 eV was result of transparency of Ce:YIG in this spectral region. Penetration depth for these energies was larger than the film thickness; therefore, the observed change of polarization has significant contribution from light propagating through the film in so called double-Faraday effect. Notable difference above 3 eV was observed among the films that was not visible in Faraday measurements. In this spectral region, double-Faraday effect no longer contributed to the signal, hence one can assume that the difference is originating in the surface of the sample. Since the difference was among all samples, it hinted to formation of damaged non-magnetic surface layer, that was probably introduced during mechanical roughening of back sides of samples, that were necessary for MOKE measurements. This was partially confirmed by Atomic force microscopy (AFM) measurements that showed peak to valley roughness of surface of around 18 nm that is much higher than usual films exhibit as grown. Similar non-magnetic interfaces have been reported in Bi:YIG films [61] as well as YIG nanoparticles [62].

Modeling

Presented experimental data were used together with 4 × 4 matrix formalism described in 1.4 to derive the off-diagonal elements of the permittivity tensor. The model consisted of thin layer on semi-infinite substrate. The measurement

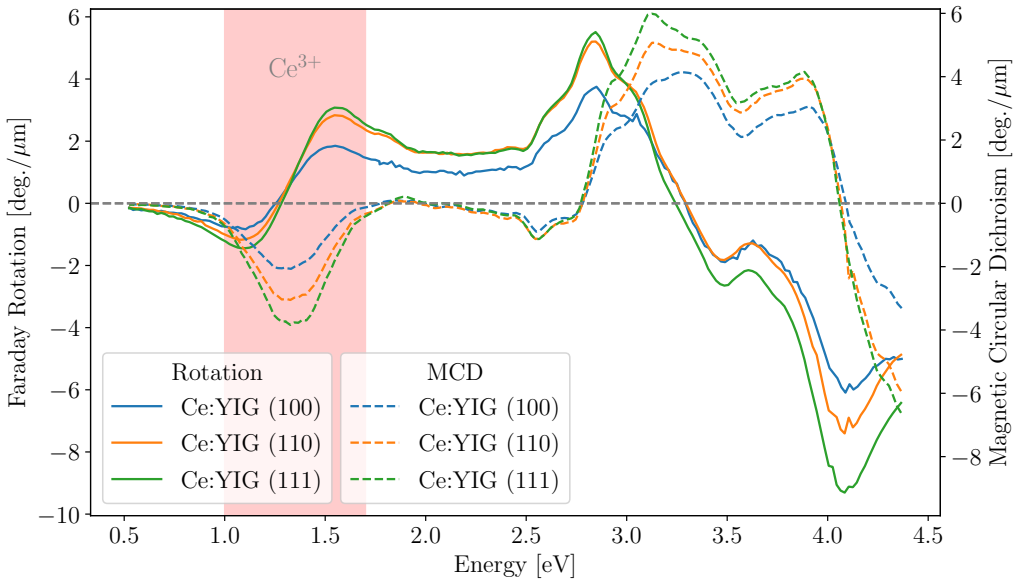

Figure 8.10: Room temperature spectral dependence of Faraday rotation and MCD of Ce:YIG (80 nm) films on GGG (100), GGG (110), and GGG (111) substrates. Spectral region marked by red background marks spectral features originating from intra-ionic electric-dipole transitions of the Ce^{3+} ions. The visible region is dominated by Fe^{3+} crystal-field transitions at both tetrahedral and octahedral sites.

of spectral dependence of Faraday effect was used for the calculations. The validation was performed by calculation of spectra of polar MOKE effect and its comparison with the experimental data (Fig. 8.12). The figure shows good agreement between experiment and the model in the whole near IR region. However, above 3 eV the simple model starts to drift away. Therefore, revised model that includes damaged non-magnetic surface layer, that was mentioned in the paragraph above, was used. With this correction, the model has excellent agreement in the whole studied region. The same modeling was performed for the rest of the films with similar results. The main difference was in the thicknesses of the surface layers.

The sample on (100) oriented substrate showed 35 nm and the one on (110) 15 nm, which was estimated based on AFM measurements.

Calculated spectra of off-diagonal elements, ε_2, are depicted in Fig. 8.13. Since the surface of the samples was damaged after the measurements of Faraday effect, the corrections described above are not included in these results. The spectra show two distinct regions. Low-energy region around 1.4 eV is, as described above, dominated with intra-ionic electrical dipole transitions in Ce^{3+} that have paramagnetic character. On the other hand higher energy charge transfer transitions involving Fe^{3+} crystal field at energies above 3 eV are diamagnetic.

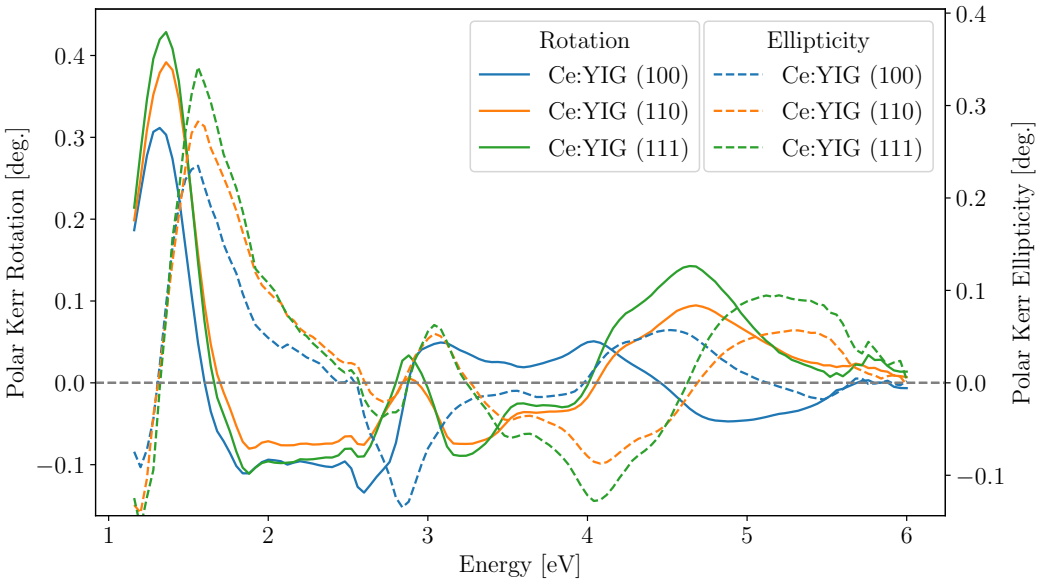

Figure 8.11: Room temperature polar Kerr rotation and ellipticity spectra of Ce:YIG (80 nm) films on GGG (100), GGG (110), and GGG (111) substrates. Enhancement of magneto-optical effect below 3 eV is caused by the interference in the film. The differences in spectra above 3 eV originates in the surface of the films that are related to substrate orientation.

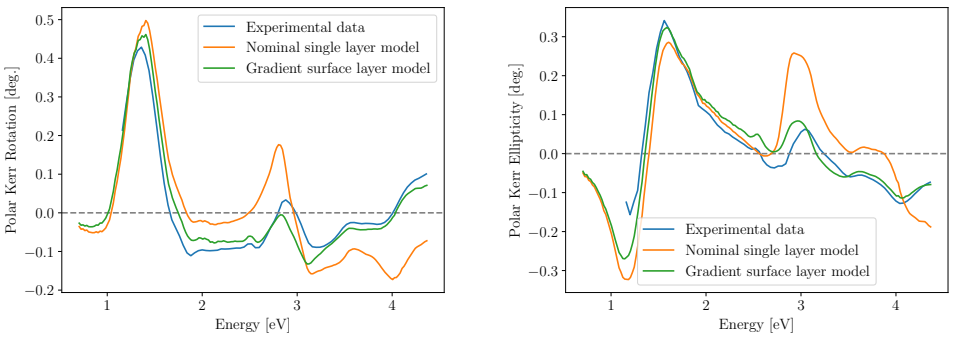

Figure 8.12: Room temperature polar Kerr (a) rotation and (b) ellipticity spectra of Ce:YIG (80 nm) films on GGG (111) substrate compared with theoretical models. Gradient surface layer model includes the effect of lowering of magnetization caused by damaged non-magnetic surface layer.

Ultra-thin films

The films presented so far were relatively thick for requirements of actual applications. The thick films wre chosen for their easier and more precise characterization. However, it is unclear, whenever the material sustains its performance once its thickness is decreased. Therefore, the second set of samples was prepared with much thinner films.

The exactly same deposition recipe was used except of ten times lower number of laser shots. Therefore, the resulting films were expected to be around 10 nm

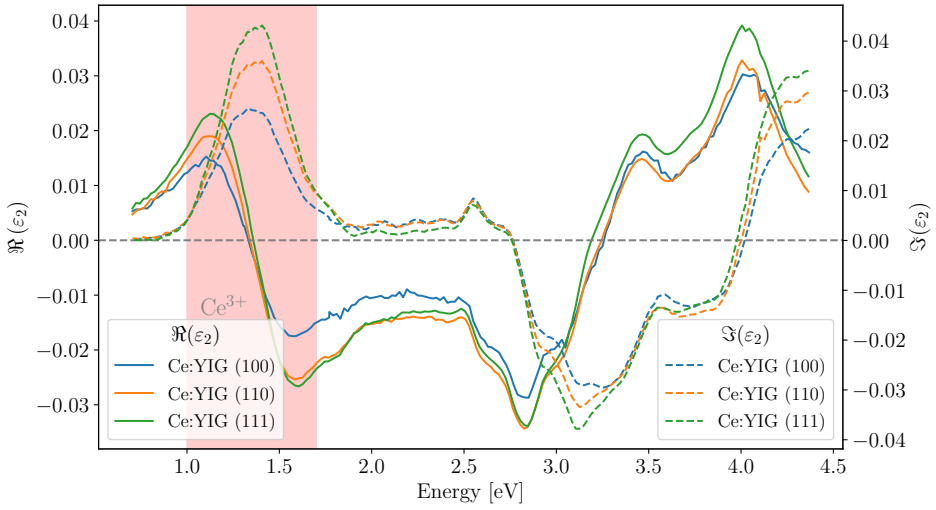

Figure 8.13: Spectral dependence of off-diagonal elements of permittivity tensor, ε_2, of Ce:YIG (80 nm) films on GGG (100), GGG (110), and GGG (111) substrates. Spectral region marked by red background indicates spectral features originating from intra-ionic electric-dipole transitions of the Ce^{3+} ions.

thick. Due to its low volume, these films could not be characterized by the means of XRD and VSM. Since the layers consists only of about eight atomic layers, its structural and magnetic properties are expected to be much less pronounced than in the case of thick films.

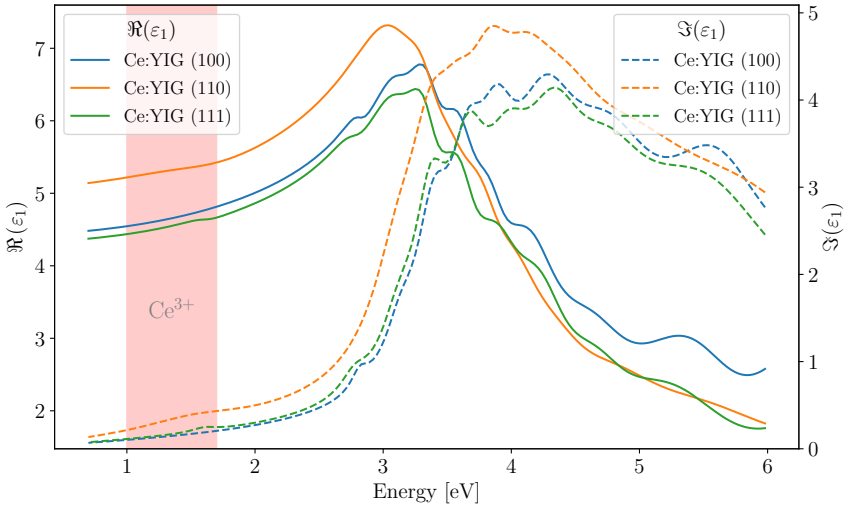

Figure 8.14: Spectral dependence of diagonal elements of permittivity tensor, ε_1, of ultra-thin Ce:YIG (10 nm) films on GGG (100), GGG (110), and GGG (111) substrates. Spectral region marked by red background indicates spectral features originating from intra-ionic electric-dipole transitions of the Ce^{3+} ions.

Optical properties were, similarly to the thick films, determined by the means of spectroscopic ellipsometry. The modeling determined their thicknesses to be

around 10 nm. The same model of harmonic oscillators as for thick films was used to describe the optical response of these films. Resulting optical constants are depicted in Fig. 8.14. Even though there is worse agreement of model with experimental data, they provide a good mean of comparison between thick and thin films. In general, the overall shape and presented features are very similar to thicker films shown in Fig. 8.8. Therefore, these films have optical response of fully developed garnet structure even for such small thicknesses. However, the transitions are more pronounced.

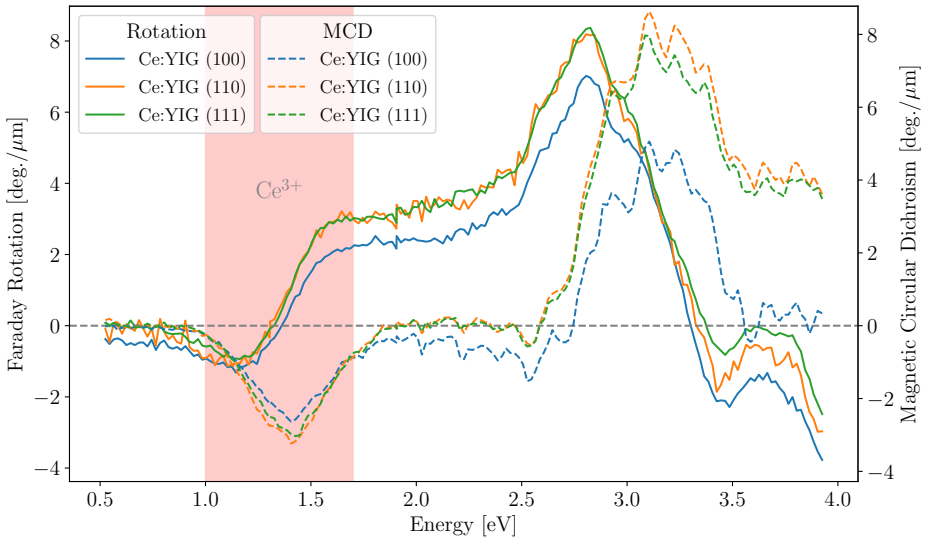

Figure 8.15: Room temperature spectral dependence of Faraday rotation and MCD of ultra-thin Ce:YIG (10 nm) films on GGG (100), GGG (110), and GGG (111) substrates. Spectral region marked by red background indicates spectral features originating from intra-ionic electric-dipole transitions of the Ce^{3+} ions. The spectral features show higher broadening than in the case of thicker (80 nm) films.

Despites the measured films were only 10 nanometers thin, measured spectra (Fig. 8.15) show high Faraday rotation per micrometer in the whole studied region. The spectral dependence is almost identical to the one of thick films (Fig. 8.10). The electronic transitions contributing to the magneto-optical response are situated at same energies; however, exhibit significantly higher broadening. That is most likely caused by higher straining of the films due to their lower thickness. Even though, the overall amplitude of the effect, especially in visible region, exceeds the one of the thick films. The influence of substrate orientation confirms the lowest performance of (100) orientation and sets the other two to similar values.

More information about the surface quality and its magnetization can be determined from measurement of polar MOKE (Fig. 8.16). These spectra show the most significant difference from thick films. Starting with transparent region situated below 2.8 eV, the effect of interference is for 10 nm negligible and therefore there is no presence of strong peak at 1.3 eV. The spectral range above 2.8 eV shows familiar spectral shape from thick films; however, this time the layer on GGG (100) does not differ. Previously, this was addressed to presence of non-

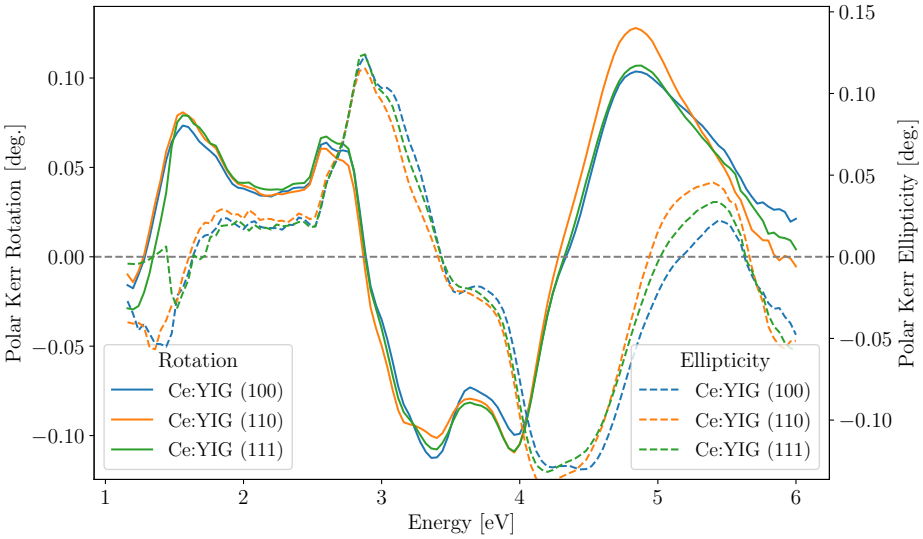

Figure 8.16: Room temperature polar Kerr rotation and ellipticity spectra of ultra-thin Ce:YIG (10 nm) films on GGG (100), GGG (110), and GGG (111) substrates. Similarity of spectra indicates weaker tendency of formation of non-magnetic layer in case of ultra-thin films independently on the substrate orientation.

magnetic layer forming at the interface influencing the magneto-optical response. In this case, the film is so thin, that it benefits its properties and since there is no relief of the strain, this interlayer does not form at all. Especially in case of (100) orientation this effect improves film's quality the most compared to thicker layers.

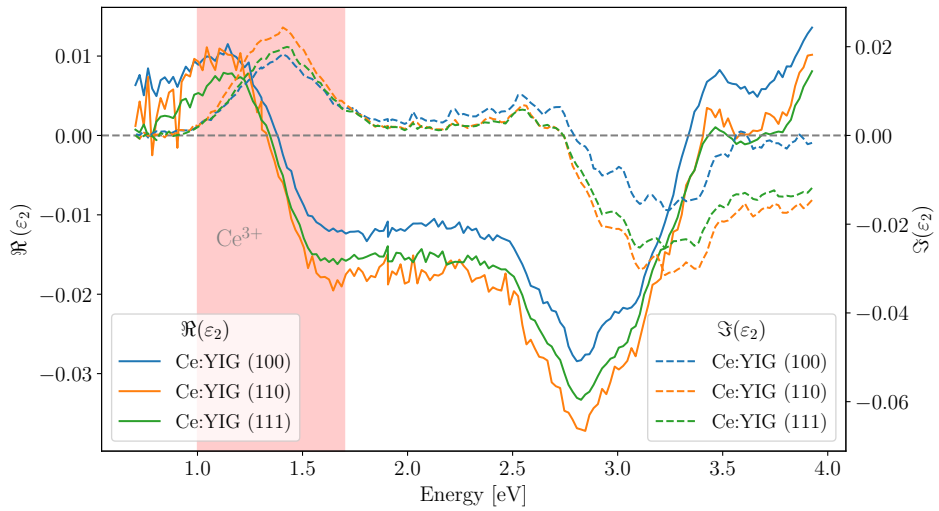

Figure 8.17: Spectral dependence of off-diagonal elements of permittivity tensor, ε_2, of ultra-thin Ce:YIG (10 nm) films on GGG (100), GGG (110), and GGG (111) substrates. Spectral region marked by red background indicates spectral features originating from intra-ionic electric-dipole transitions of the Ce^{3+} ions.

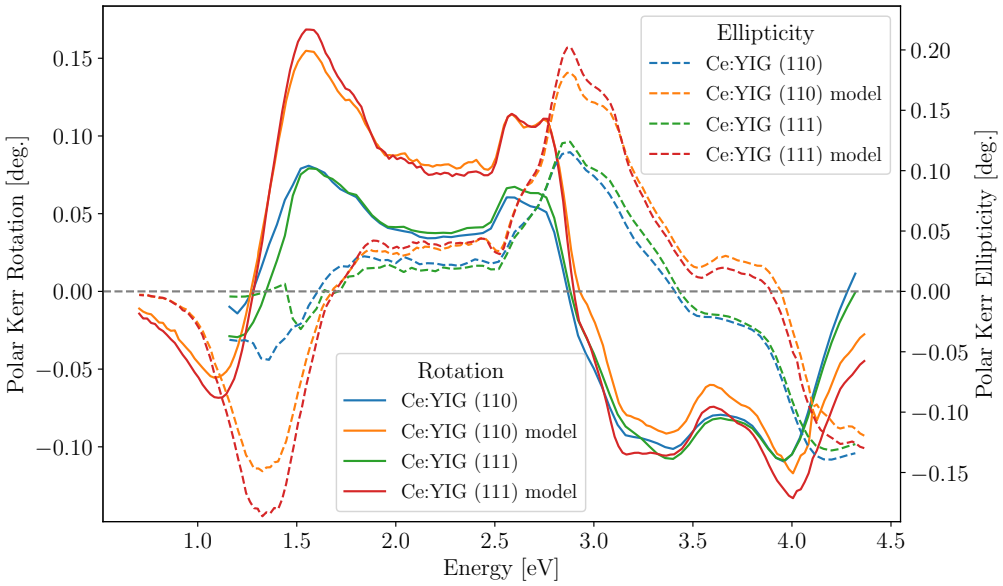

(a) Polar MOKE

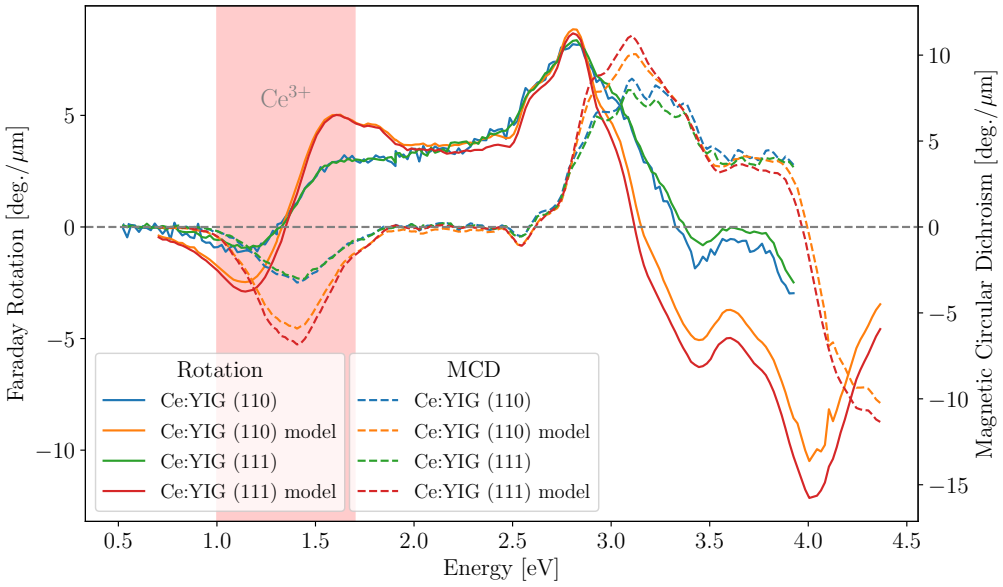

(b) Faraday Effect

Figure 8.18: Room temperature (a) polar MOKE and (b) Faraday effect experimental spectra of ultra-thin Ce:YIG (10 nm) films on GGG (110), and GGG (111) substrates compared with theoretical model calculated using permittivity tensor of thick (80 nm) films. Overestimation of model in IR region indicates smaller concentration of Ce in ultra-thin (10 nm) films compared to thick (80 nm) films.

To complete the analysis, the off-diagonal terms of permittivity tensor of these films were calculated as shown in Fig. 8.17. Similarly to other observations, the spectral shape is very similar to thicker films (Fig. 8.13) and therefore the overall magneto-optical response of these films should not differ from them. This finding was confirmed by calculating of polar MOKE and Faraday effect using permittivity tensor of thick samples and model structure of the thin ones. Comparison of

these calculations with experimental data from thin films is shown in Fig. 8.18. Starting with polar MOKE in Fig. 8.18a, one can see excellent agreement in non-transparent region above 2.8 eV. The origin of the deviation at lower energies is better explained looking at the spectra of the Faraday effect shown in Fig. 8.18b. The difference lays only in region that is specifically originating from Ce ions. This concludes, that even 10 nm thin films exhibit optical and magneto-optical properties of much thicker films. However, less Ce is incorporated into the garnet structure under the same deposition conditions.

Figure of Merit

For the evaluation of application potential in telecommunication, the FoM of studied films was determined. In the IR spectral region, garnets have great advantage due to their small absorption (Fig. 8.19). Such small values unfortunately cannot be determined with enough accuracy by use of spectroscopic ellipsometry by itself. Therefore, a highly precise Thermo Nicolet Nexus Fourier-transform infrared spectroscopy (FTIR) spectrometer was employed to measure IR transmission of studied films. These data were combined with measurements of spectroscopic ellipsometry and considered in ellipsometry fitting. For the best performance in the IR region, studied spectral region was limited to energies around 0.8 eV and the optical response was modeled using Cauchy relations [11]. The result of this procedure is depicted in Fig. 8.20. The most notable film is the one deposited on GGG (100) orientation. The difference; however, might be only the relict of measurement technique. Since the studied system is thin film on much thicker substrate, multiple reflection in the film play huge influence in the overall transmission of the sample. This effect is determined by the difference between refractive indexes of these materials and due to the interference character of the phenomenon, even small deviations might have significant impact on the performance of the model. The Fig. 8.7 suggests there is small, but present, difference in optical properties between substrates of different orientation. This might be cause of higher absorption of film on (100) substrate orientation, because its optical properties were not accounted for in the modeling precise enough due to measurement error. To safely conclude the origin of the higher extinction coefficient, other techniques like photothermal deflection spectroscopy would have to be employed.

Optical and magneto-optical properties were used to calculated spectral dependencies of figure of merit for all studied samples that are depicted in Fig. 8.21. Due to lowering of absorption coefficient towards lower photon energies, FoM shows significant increase peaking around communication wavelength. The values differ greatly among substrate orientations, but the best performance of 943 deg./dB was achieved with the film on GGG (111). The final factor, that made this film to stand out, is position of absorption edge, that is shifted slightly towards higher energies than in the cases of other two (Fig. 8.19). Since 0.8 eV is very close to this edge, absorption in this region follows very steep trend and the shift of only 0.1 eV yielded this result. The position of absorption edge in strongly bound to the Ce content in the material and therefore that is what is expected to be driving force in this matter. For comparison, this value does not exceed the performance of bulk single crystal [63]; however, outmatches other thin films

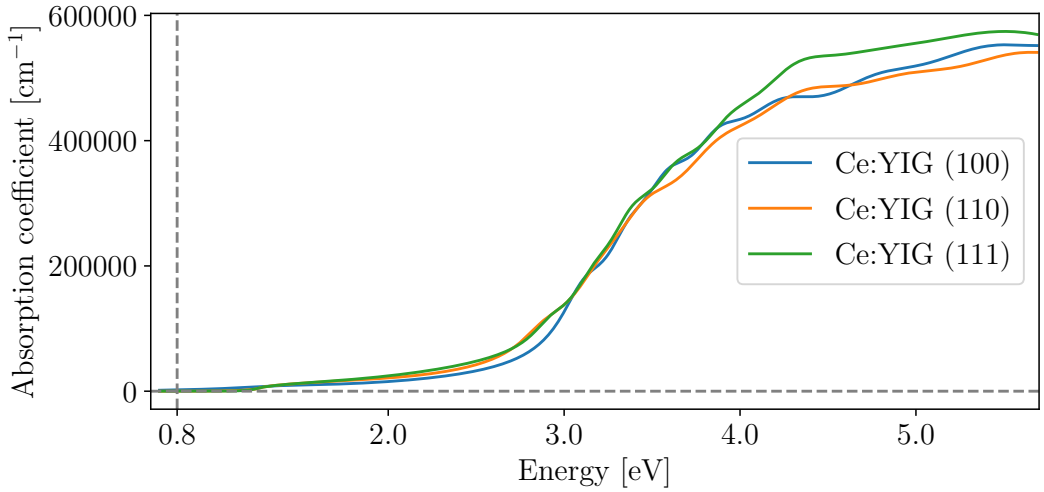

Figure 8.19: Room temperature spectral dependence of absorption coefficient of Ce:YIG (80 nm) films on GGG (100), GGG (110), and GGG (111) substrates.

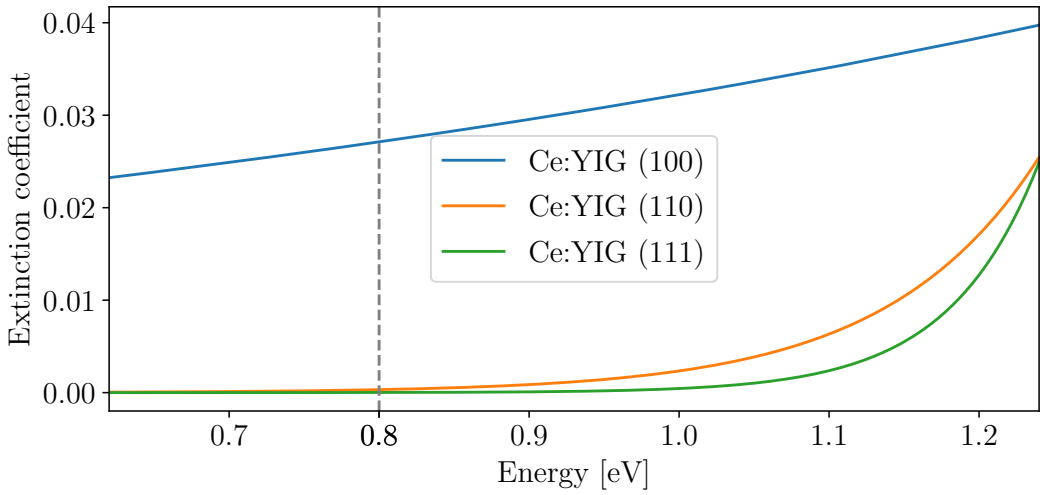

Figure 8.20: Room temperature spectral dependence of extinction coefficient of Ce:YIG (80 nm) films of GGG (100), GGG (110), and GGG (111) substrates in IR region.

reported so far [51, 52, 57, 63, 64, 65, 66, 67]. Further comparison with other materials and techniques presented through this work is shown in Table 8.1.

8.3 $Ce_xY_{3-x}Fe_5O_{12}$ on Si

Preparation of single crystal garnet films on silicone has so far shown to be unachievable task. That is due to enormous difference in lattice constant where the one of garnet is more than $2\frac{1}{3}$ times bigger. There have been reports of polycrystalline films achieved by post annealing [41]; however, there are still very significant constrains in achievable Ce content. In the case of Ce:YIG on GGG substrate, the limit is Ce:Y ratio of 2.5:0.5 due to epitaxial interface stabiliza-

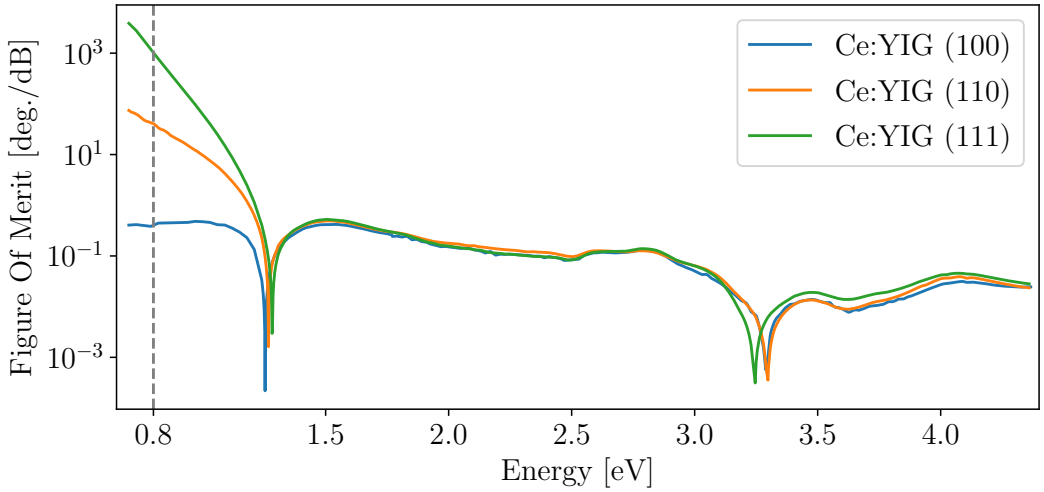

Figure 8.21: Spectral dependence of FoM of Ce:YIG (80 nm) films on GGG (100), GGG (110), and GGG (111) substrates. Telecommunication wavelength 1550 nm (0.8 eV) is marked by dashed line.

Material and substrate	FoM [deg./dB]	Growth method	Optical loss [dB/cm]	Reference
$Y_{2.82}Ce_{0.18}Fe_5O_{12}$	1420	Floating zone	0.52	[63]
Ce:YIG on GGG (111)	943	PLD	6	ch. 8.2
Ce:YIG on Si	38	PLD	29	[52]
Ce:YIG on Si	21.8	PLD	58	[51]
Ce:YIG on Si	4	PLD	256	ch. 8.3
YIG/Bi0.8YIG/Si	397	PLD	1.26	ch. 8.4
Bi1.5YIG/YIG/Si	769	PLD	2.6	ch. 8.4

Table 8.1: Comparison of the room temperature FoM values at telecommunication wavelength (1550 nm, 0.8 eV) of garnets presented through this work and in the literature.

tion [52, 66]. In case of the film on Si substrate is this limit even lowered to ratio of 1:2. Furthermore, magneto-optical response of polycrystalline films tends to be much lower than the one of single crystal films. This section presents the technique for further phase stabilization using YIG seed layers. This improves crystallographic quality of films as well as their magneto-optical response.

Samples

Samples in this chapter were prepared by PLD on silicon (100) substrates. The different Ce content of studied samples was achieved by deposition from targets of specific compositions. These ceramic targets of $Ce_xY_{3-x}Fe_5O_{12}$ (x=1.0, 1.2, 1.4, 1.5) were prepared by Sintering method (Ch. 4.3) from powders of Y_2O_3, CeO_2 and Fe_2O_3. The PLD system used a Compex Pro 205 KrF laser operating at

248 nm and at 10 Hz repetition rate. YIG seed layers were deposited at substrate temperature of 400 °C in oxygen partial pressure of 5 mTorr. Afterward, the film was crystallized using rapid thermal annealing (RTA) at temperature of 800 °C. Second growth of Ce:YIG was carried at higher temperature (650 °C). After the process, the sample was kept in vacuum for 30 minutes to further stabilize the phase of the films before the cooling down to the room temperature. There was no more annealing after the deposition process. Film thicknesses, determined by SEM, were ranging between 162 and 219 nm [56].

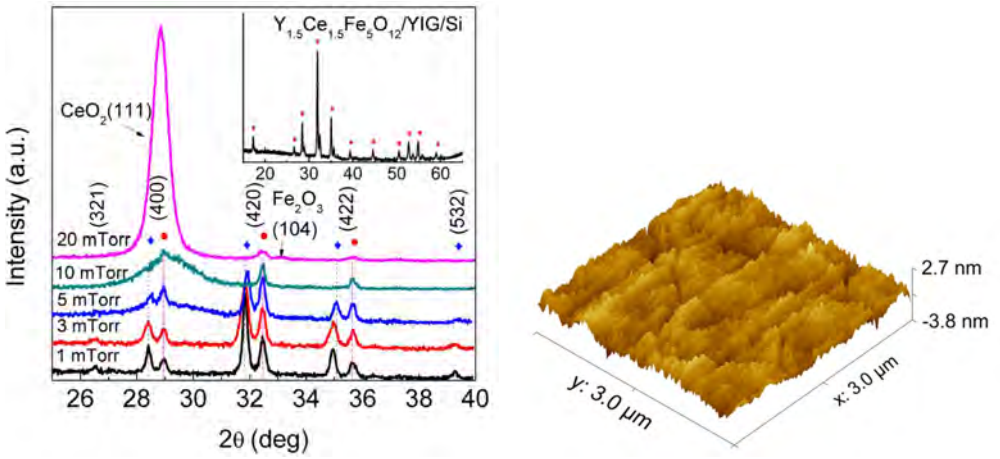

(a) XRD pattern (b) AFM

Figure 8.22: (a) XRD patterns of $Ce_{1.5}Y_{1.5}Fe_5O_{12}$ films deposited on YIG seed layer on Si at various oxygen pressures during the deposition. Blue dots and red squared marks peaks originating from Ce:YIG and YIG, respectively. Inset shows wider scan of Ce:YIG deposited at oxygen pressure of 1 mTorr. (b) Surface morphology of Ce:YIG film deposited at oxygen pressure of 1 mTorr measured by AFM over 3 μm wide scan.

Crystallization of Ce:YIG even on YIG seed layer was found to be very sensitive to working pressure of oxygen during the deposition. Fig. 8.22a shows difference in XRD patterns depending on oxygen pressure with highlighted garnet peaks. Starting from 20 mTorr one can see the formation of secondary phase of CeO_2 and Fe_2O_3 instead of Ce:YIG. After decreasing pressure below 10 mTorr, peaks belonging to garnet structure emerge on the scan. For pressure of 1 mTorr the XRD scan shows clear separation of diffraction peaks of the seed layer of YIG and Ce:YIG. Diffraction peaks of Ce:YIG are at lower angles due to its larger lattice constant. The average grain sizes of $Ce_{1.5}Y_{1.5}Fe_5O_{12}$ for samples deposited at 3 and 1 mTorr are 28 and 38 nm respectively. Consistently with the small grain size, the surface roughness of these films was only 0.7 nm (Fig. 8.22b), which is comparable to the YIG seed layer roughness of 0.6 nm. More detailed structural analysis can be found in Ref. [56].

Magnetic properties

Magnetization hysteresis loops at room temperature are shown in Fig. 8.23. As follows from the figure, studied samples exhibited in-plane magnetization easy-axis and their anisotropy fields increased with Ce content. Films with Ce content

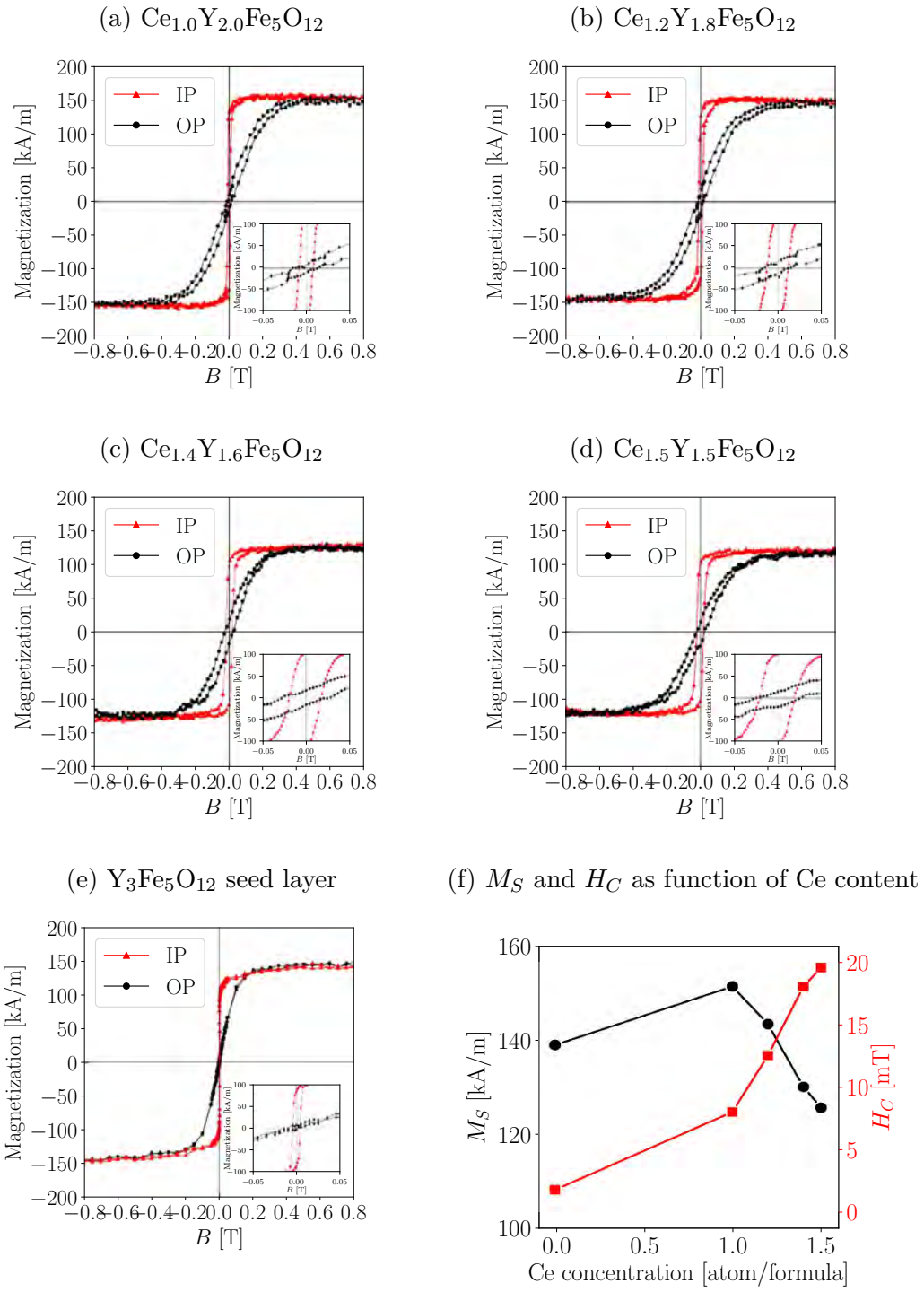

Figure 8.23: Room temperature magnetic hysteresis loops of $Ce_xY_{3-x}Fe_5O_{12}$/YIG films of nominal composition (a) x = 1.0, (b) 1.2, (c) 1.4, (d) 1.5; as well as (e) YIG seed layer. (f) The magnetic saturation M_S and coercivity H_C of $Ce_xY_{3-x}Fe_5O_{12}$/YIG films as a function of Ce concentration.

of x = 1.0 and 1.2 show higher saturation magnetization than pure YIG what indicates presence of Ce^{3+} ions with $4f^1$ unpaired electrons contributing to the magnetic moment. This finding was also confirmed by XPS measurements [56]. The

films with Ce concentration above 1.0 show decrease of M_S, which is caused by the change of occupancy of Fe sites that are in anti-parallel orientation. Anisotropy fields were ranging between 0.35 and 0.45 T which is significantly higher that the values presented in previous chapter for the single crystal films. Taking in account out-of-plane demagnetization factor of a thin film $N = 4/pi$, the shape anisotropies were determined to be 0.19 T, 0.18 T, 0.16 T and 0.16 T for x = 1.0, 1.2, 1.4 and 1.5 samples respectively. These values are on the other hand much smaller than in the case of thin films indicating other contributions to in-plane anisotropy. This could be magnetoelastic anisotropy as well as deposition-induced anisotropy. The magnetization switching in the direction of easy-axis shows distinct switching at low fields with slow approach to the saturation field that can be explained by pinning of domain walls at the grain boundaries. The coercivity fields show increase with Ce concentration as shown in Fig. 8.23, which confirms role of Ce incorporated in the garnet lattice as pinning centers.

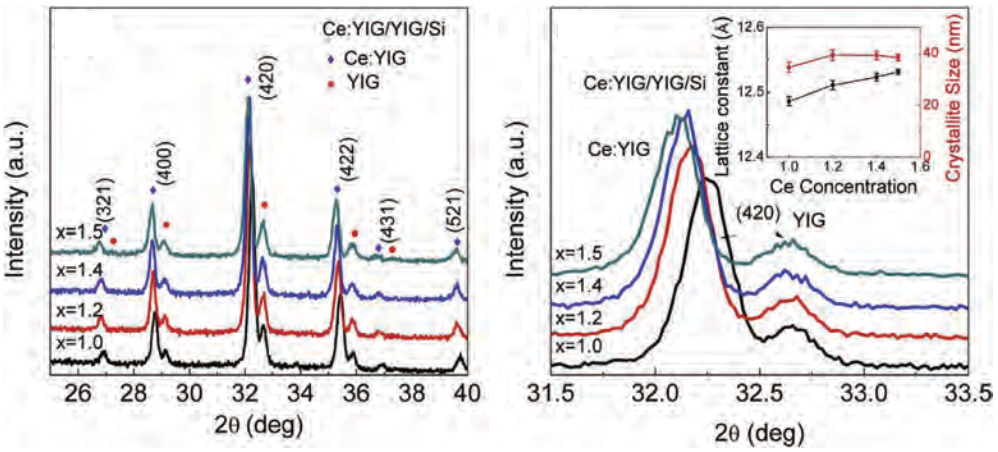

(a) XRD scan (b) (420) peak detail

Figure 8.24: (a) XRD pattern of $Ce_xY_{3-x}Fe_5O_{12}$/YIG films on Si substrates. Blue dots and red squared marks peaks originating from Ce:YIG and YIG, respectively. (b) Detail of (420) diffraction peak. The inset shows the calculated lattice constant and grain size of $Ce_xY_{3-x}Fe_5O_{12}$ films with error bars.

Magneto-optical properties

Magnetic hysteresis loops of Faraday effect were measured at the energy of 0.8 eV (1550 nm) are shown in Fig. 8.25a. One can see, that all features described in the previous paragraph are resembled in the magneto-optical response. The amplitude of the Faraday rotation angle in saturation monotonically increased with Ce concentration (inset in Fig. 8.25a). The highest achieved value was (-0.641 ± 0.015) deg./μm in the $Ce_{1.5}Y_{1.5}Fe_5O_{12}$ sample. For comparison, the $Ce_1Y_2Fe_5O_{12}$ showed similar values to films deposited by radio frequency (RF) sputtering [68]. The connection of the increase on magneto-optical response with incorporation of Ce^{3+} ions into the lattice was confirmed by XRD scans depicted in Fig. 8.24. Due to size of Ce atoms, the lattice constant shows increase with the Ce concentration.

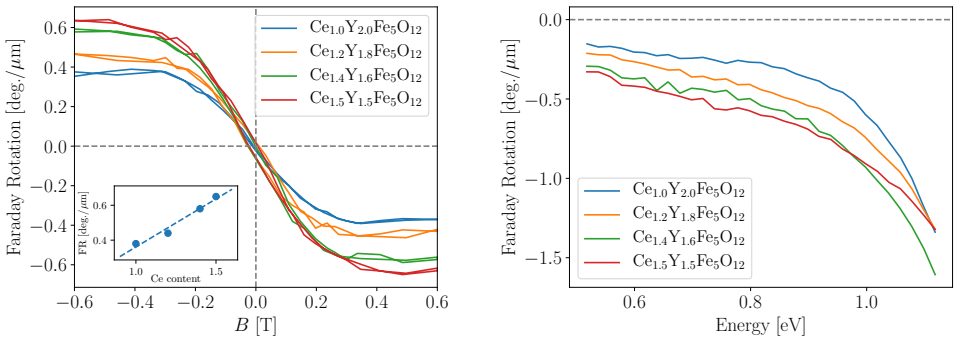

(a) Loops of Faraday rotation (b) Faraday rotation spectra

Figure 8.25: (a) Room temperature Faraday rotation hysteresis loops of $Ce_xY_{3-x}Fe_5O_{12}$ films with YIG seed layer on Si substrates measured at 0.8 eV (1550 nm). The inset shows increase of saturation FR with Ce content. (b) Room temperature Faraday rotation spectra of $Ce_xY_{3-x}Fe_5O_{12}$/YIG films measured in near IR spectral region.

The magneto-optical response of deposited films was further analyzed by measurement of spectral dependencies of Faraday rotation (Fig. 8.25b) in the spectral range from 0.5 eV to 1.12 eV. The upper limit is determined by the absorption edge of Si substrate. Similarly to single crystal films, the films exhibited tail of intrinsic paramagnetic Ce transition at 1.44 eV that is reaching down to the near infrared region [59, 69]. The increase of amplitude with Ce content is consistent with single wavelength measurement results at 0.8 eV (1550 nm).

Optical properties

To finalize the analysis of the investigated films, spectroscopic ellipsometry was measured to determine optical properties that are depicted in Fig. 8.26. Optical constants of samples are comparable to the reported values in literature [68]. Focusing on wavelength of 1550 nm, the real part of permittivity decreases with the increase of Ce concentration. The optical absorption of films seems to be, on the other hand, much higher than reported in literature [68]. This might be due to lower fabrication oxygen partial pressure, since oxygen vacancies are known to increase the absorption coefficient [19]. Because of the high optical absorption, the performance of these films at telecommunication wavelengths would not be sufficient for applications. However, due to their high Faraday rotation, they could be used in fields less critical to optical loss such as magneto-optical imaging or magneto-plasmonics. There is also potential for improvement of the absorption coefficient by tuning the oxygen pressure during the deposition.

8.4 $Bi_xY_{3-x}Fe_5O_{12}$ on Si

The previous section demonstrated that Ce:YIG can be to some extend transferred to Si substrate; however, only in the form of polycrystalline films. This leads to worsening of optical absorption in near IR spectral region resulting in low FoM. Furthermore, higher concentration of Ce in YIG lattice inevitably leads

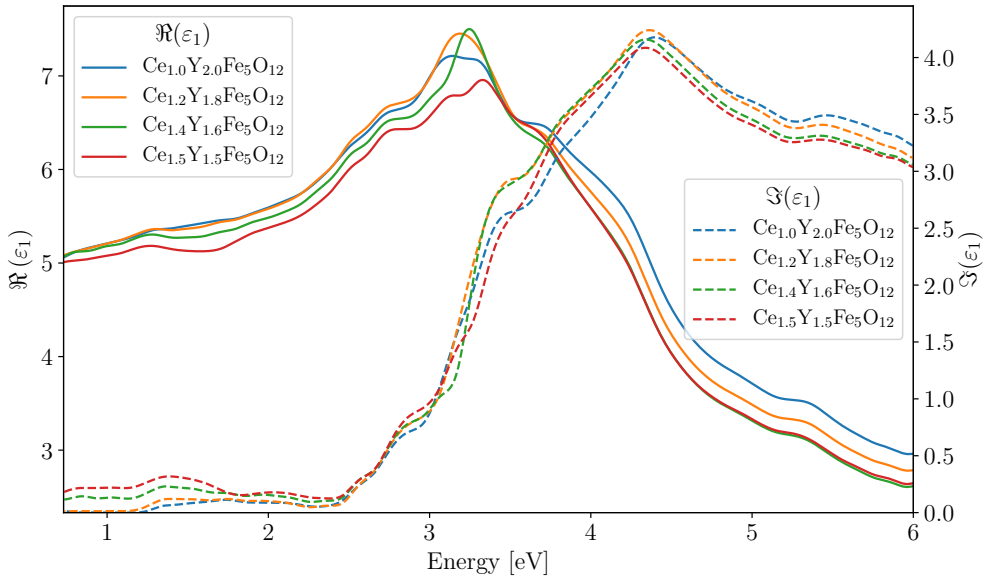

Figure 8.26: Spectral dependence of diagonal elements of permittivity tensor, ε_1, of $Ce_xY_{3-x}Fe_5O_{12}$/YIG films on Si substrates determined from measurements of spectroscopic ellipsometry.

to the formation of CeO_2 phase. One solution to this problem is a choice of different garnet that is easier to transfer to silicone. With this motivation, this study focuses on series of samples of Bi:YIG. For better characterization of Bi:YIG films, the first characterization is performed on layers grown on GGG, before the deposition on Si.

Growth

The deposition system used for preparation of samples in this section is the same as in the section 8.2. Similarly to previous section, the effect of oxygen pressure p_{O_2} during the deposition on the crystallinity and stoichiometry of grown films was studied. Additionally the effect of substrate temperature T_s was included as well. Result of this study is shown in Fig. 8.27. The composition of these films was measured by means of wavelength dispersive spectroscopy (WDS). For the characterization of investigated films, the ratio (Bi+Y)/Fe is used. Its value for stoichiometric case is equal to 0.6. For the purpose of more complex analysis, the samples were grown on Si (100) substrates as well as on GGG (100). Independently on the type of substrate, films from the same growth cycle showed the same stoichiometry. Amount of Bi in films can be controlled by both, p_{O_2} as well as T_s. Bismuth-rich films were prepared with low T_s along with high p_{O_2} as shown in Fig. 8.28. Low T_s is crucial due to volatility of Bi and similar trends were also observed in growth of $BiFeO_3$ [70, 71]. The effect of high p_{O_2} can be explained with scattering of the ablated species by the oxygen in the chamber. Since Bi is a heavy element, it is less prone to scattering than other much lighter atoms. The pressure also affects Y/Fe ratio resulting in (Bi+Y)/Fe ratio being much lower than target 0.6 for low pressures, but increases with p_{O_2}. Graphi-

cal representation of stoichiometry dependence is shown in Fig. 8.27b. Based on these results, garnet with stoichiometric ratio close to 0.6 can be grown in window between 520 and 600 ° at p_{O_2} of 20 mTorr. Example of high resolution X-ray diffraction (HRXRD) scans of these films is shown in Fig. 8.27a. Moreover, films grown at oxygen pressure between 10 and 100 mTorr did not exhibit formation of secondary phases as well.

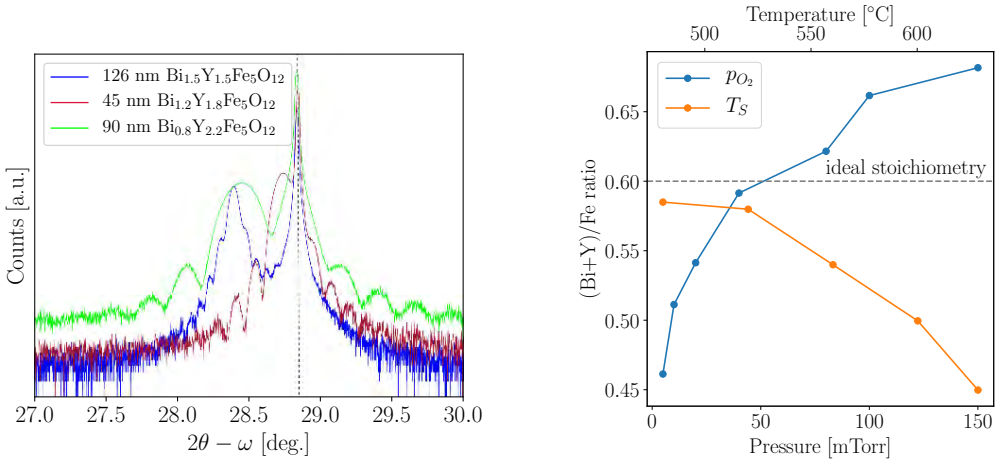

(a) XRD scans (b) Composition ratio

Figure 8.27: (a) HRXRD patterns of Bi:YIG films deposited at 560 °C substrate temperature and 100 mTorr oxygen pressure on GGG (100) substrates around (400) diffraction peak. The peak originating from GGG substrate is marked by dashed line. (b) (Bi+Y)/Fe ratio as a function of T_S (red line) and oxygen pressure (black line). Ideal stoichiometry is marked by dashed line.

(a) O_2 Pressure (b) Substrate Temperature

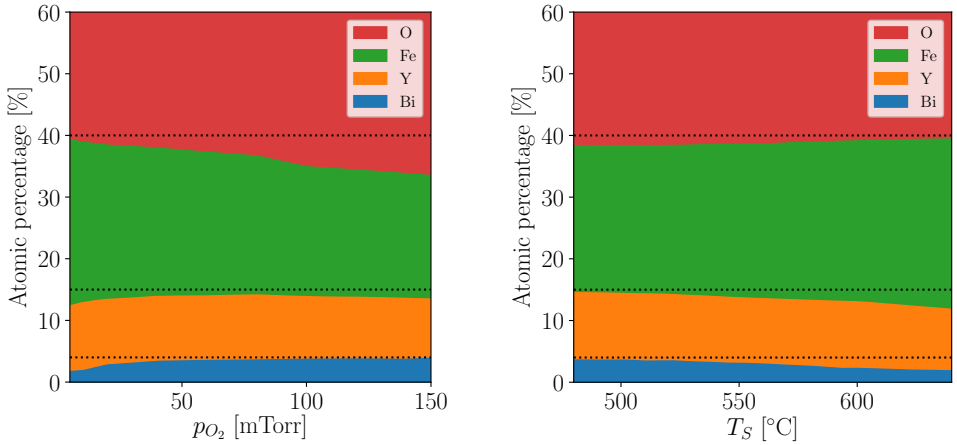

Figure 8.28: The effect of (a) oxygen pressure ($T_S = 560$°C) and (b) temperature ($p_{O_2} = 20$ mTorr) on composition of films grown from a target of $Bi_{0.8}Y_{2.2}Fe_5O_{12}$.

Magnetic properties of singlecrystalline films

Magnetic properties of films were measured by VSM (Fig. 8.29). The M_S values around 120 kA/m are similar to previous reports [51]. The anisotropy field of the films is not significantly influenced by the amount of Bi the film; however, it causes the increase of H_C. Due to different thickness of film, it is unclear, whether this effect is strain related or originates only from the presence of Bi in the lattice. All samples exhibit magnetization hard-axis in out-of-plane direction and the easy-axis lay in-plane to the film surface.

Magneto-optical properties of singlecrystalline films

Fig. 8.30 shows magnetic hysteresis loops of Faraday effect after removal of substrate contribution. These loops resemble the shape of magnetization measured by VSM. Faraday effect in saturation increases linearly with the bismuth content as previously showed in chapter 8.1 and reported in Ref. [72]. Therefore, the magneto-optical response can be controlled by tuning of this parameter.

Spectral dependencies of Faraday effect are shown in Fig. 8.31. The observed spectral shape can be compared with Fig. 8.2 to see the differences of films between deposition techniques. Even though the spectral features lay on the same energies that are specific for Bi:YIG films [20, 72], one can see that ratio of their contribution differs. This effect is caused by iron deficiency of garnets grown by PLD. Missing iron is usually replaced with another element causing shift of ratio in magnetization contributions of sublattices. The observed spectra imply, that this effect is selective only to one of the iron sublattices. In this specific case, it changes the steepness of the tail reaching towards IR region resulting in higher Faraday rotation in this spectral region than in films deposited by MOD. Otherwise, the amplitude of the Faraday rotation is in agreement with low concentration of Bi in the films.

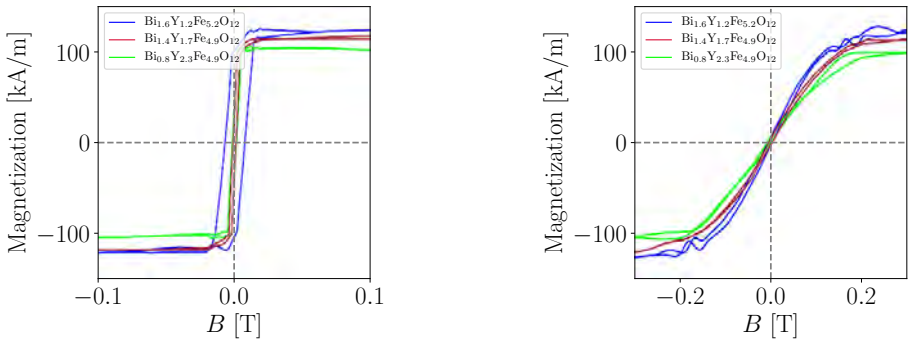

(a) In-plane

(b) Out-of-plane

Figure 8.29: Room temperature magnetic hysteresis loops of Bi:YIG films of various Bi content on GGG (100) substrates. Field was applied (a) in-plane and (b) out-of-plane to the film plane. All films exhibit in-plane magnetization easy-axis.

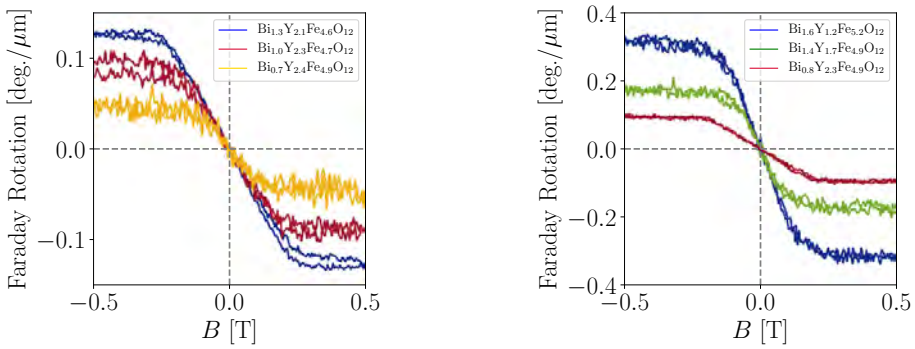

Figure 8.30: Room temperature Faraday rotation hysteresis loops of Bi:YIG films with various Bi content on GGG (100) substrates deposited at (a) different oxygen pressures and (b) using different stoichiometry of the target measured at 0.8 eV (1550 nm).

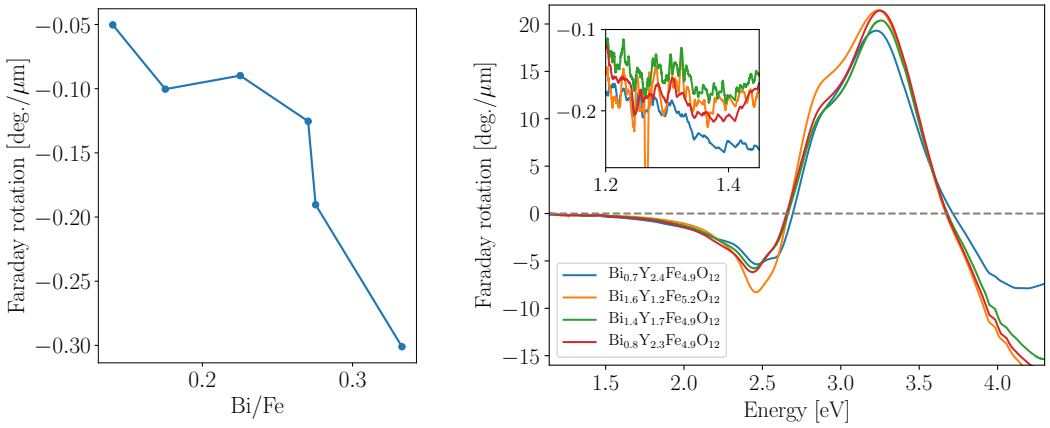

(a) FR versus Bi/Fe ratio

(b) Spectra of Faraday rotation

Figure 8.31: (a) Saturated Faraday rotation at 0.8 eV (1550 nm) of Bi:YIG films of GGG substrates as a function of Bi/Fe ratio. (b) Room temperature spectral dependence of Faraday rotation of Bi:YIG films of various Bi content on GGG (100) substrates. The inset shows zoom of Faraday rotation in near IR spectral region.

Samples on Si

The other approach to influence stoichiometry, rather than tuning T_s and p_{O_2}, is use of non-stoichiometric target. This way is more convenient once the working deposition conditions are found, because it produces films with more consistent properties. Therefore, the samples on Si were deposited using targets of composition $Bi_{0.8}Y_{2.2}Fe_5O_{12}$, $Bi_{1.2}Y_{1.8}Fe_5O_{12}$ and $Bi_{1.5}Y_{1.5}Fe_5O_{12}$. Deposition of films using these targets on Si did not produce a garnet structure even after annealing. Therefore, YIG seed layer had to be introduced into the structure as was previously shown for Ce:YIG in Chapter 8.3 and other studies [51, 73]. Two types of geometry are at hand. The structure with YIG layer underneath Bi:YIG film is called bottom-up crystallization. The opposite configuration is called top-down

crystallization (Fig. 8.32a). Performance of crystallization with seed layers can be seen on XRD scans depicted in Fig. 8.32b. To further improve the crystallinity, additional RTA at 800°C for 5 min was performed after take out of the samples from the chamber. During the optimization of growth of the films, formation of secondary phases of Bi_2O_3 and Fe_2O_3 was observed in the case of top-down configuration. Theses phases can be explained by effect of the capping layer. Coverage of the surface stops exceeding Bi during annealing from leaving the structure and therefore forms secondary phases at the interface between the film and the seed layer. This effect was suppressed by preannealing of the sample in the chamber before the YIG seed layer is deposited. The other option to prevent secondary phase formation is providing more Fe into the film structure by co-deposition of Fe_2O_3. Unfortunately this approach dit not yield any films of sufficient quality.

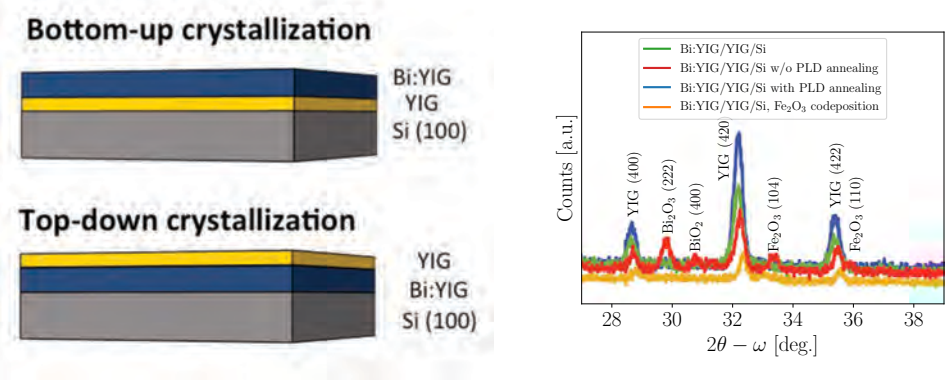

(a) Crystallization scheme (b) XRD patterns

Figure 8.32: (a) Schematic of bottom-up and top-down crystallized films. (b) XRD patterns of Bi:YIG films deposited on Si substrates after RTA.

Magnetic and magneto-optical properties of samples on Si

Measurement of magnetization loops of samples on Si are shown in Fig. 8.33. The improved signal to noise ratio of these measurement in comparison to Fig. 8.29 is caused by lack of much stronger magnetic substrate. Looking closer at the measured values, saturation magnetization and anisotropy field are similar to the values obtained for films on GGG. The Faraday rotation of up to -0.2 deg./μm at 0.8 eV (1550 nm) is exceptional for polycrystalline films. The highest magneto-optical response achieved (Fig. 8.34) is similar to previous samples with high Bi content coming from $Bi_{1.5}Y_{1.5}Fe_5O_{12}$ target [20, 72, 74, 75]. Since the contribution of YIG layer cannot be separated from Faraday signal, presented values are overall Faraday rotation of the whole structure including YIG seed layer. Looking at the difference between the types of seed layer, one can see that achieved values are comparable between samples with the same target composition.

Optical properties

Optical properties of studied samples were investigated using spectroscopic ellipsometry. The model structure was altered to mirror the position of seed layer for each type of crystallization. Optical properties of substrates as well as YIG

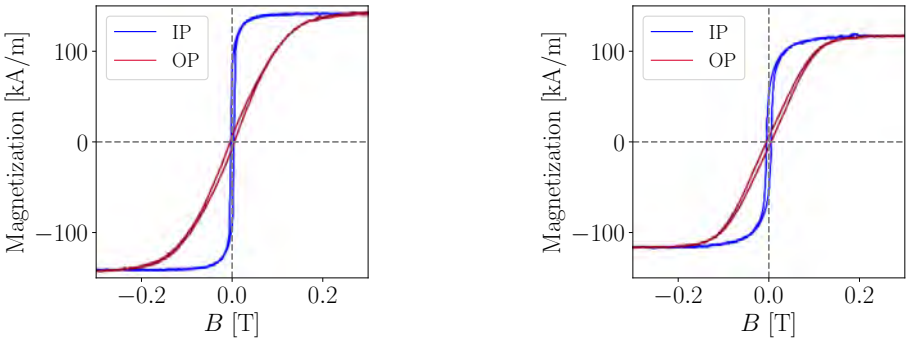

(a) Bottom-up (b) Top-down

Figure 8.33: Room temperature magnetic hysteresis loops of Bi:YIG films on Si after RTA deposited from (a) $Bi_{1.2}Y_{1.8}Fe_5O_{12}$ target with bottom-up crystallization and (b) $Bi_{1.5}Y_{1.5}Fe_5O_{12}$ target with top-down crystallization.

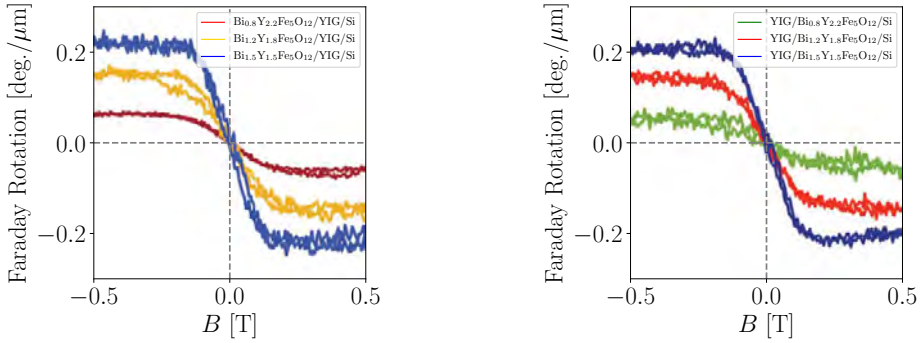

(a) Bottom-up (b) Top-down

Figure 8.34: Room temperature Faraday rotation hysteresis loops of Bi:YIG films on Si with various Bi content measured at 0.8 eV (1550 nm) using (a) bottom-up and (b) top-down crystallization.

were measured on separate samples to further improve the precision of the model. Resulting optical properties are depicted in Fig. 8.35. The spectral shape of optical constants is typical for iron based garnets [76, 20, 39, 75, 77]. Similarly to previous chapters, one can see the shift in optical absorption towards lower energies with the increase of Bi content. The optical constants obtained from samples on GGG substrates were further used as a starting point for the samples on Si. The results of their fitting are shown in Fig. 8.36. The spectra in this case follow the general shape observed on singlecrystalline films, but smaller features are more pronounced. From applications point of view, it is vital, that extinction coefficient still falls dramatically towards the IR region resulting in the highest values of FoM at 1550 nm for polycrystalline garnet on Si reported (769 deg./dB, see Tab. 8.1). These values are even more than an order of magnitude higher than previously reported values for Ce:YIG films [51, 52].

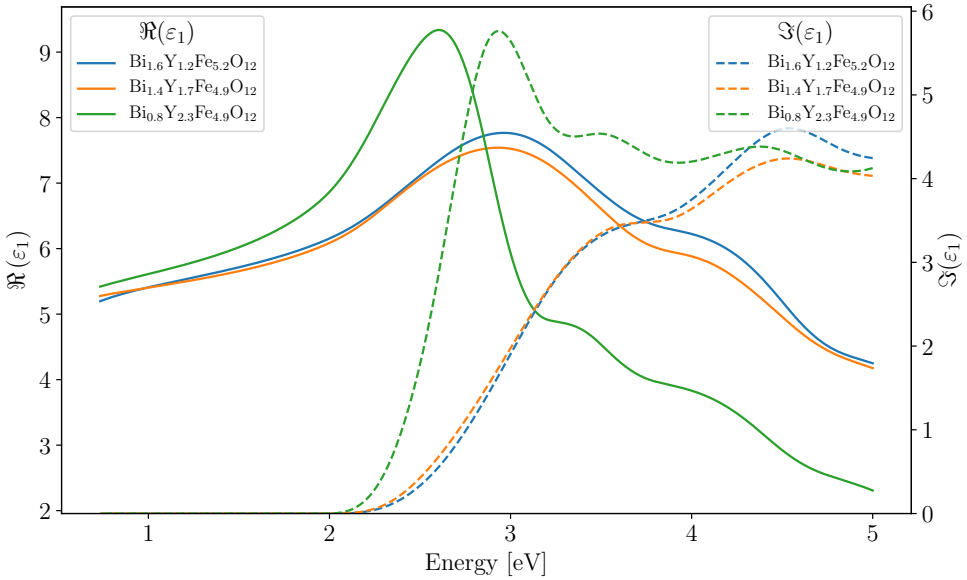

Figure 8.35: Spectral dependence of diagonal elements of permittivity tensor, ε_1, of Bi:YIG films with various Bi content on GGG (100) substrates.

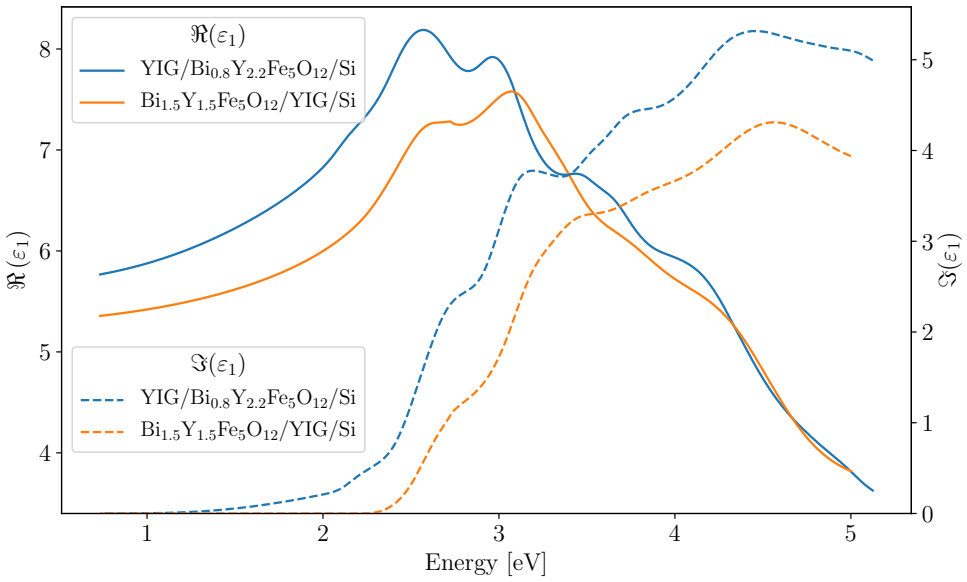

Figure 8.36: Spectral dependence of diagonal elements of permittivity tensor, ε_1, of Bi:YIG films using top-down (blue line) and bottom-up (orange line) crystallization on Si (100) substrates.

9. Garnets with perpendicular magnetic anisotropy for spintronics

Every garnet film presented in this work so far had its magnetic anisotropy with easy magnetization axis pointing in-plane. This orientation of magnetization can be explained by the highest contribution of shape anisotropy into the anisotropy energy. The contribution of the magnetocrystalline anisotropy is much smaller than shape anisotropy, because there was no significant change of the anisotropy in films deposited on different substrate orientations. However, films with PMA would be preferable for many applications [78, 79]. It has been already shown that the last contribution in anisotropy energy, magnetoelastic anisotropy, can be utilized to tilt easy magnetization axis of thulium iron garnet ($Tm_3Fe_5O_{12}$) (TmIG) out-of-plane [80]. This study also demonstrated the possibility of magnetization switching of garnet film via physical phenomenon called spin orbit torque. This study attempted to prepare other garnet films that would exhibit PMA.

Based on magnetic anisotropy constants for bulk crystals [19], there are two additional candidates, that could be grown on GGG and exhibit PMA. The first one, europium iron garnet ($Eu_3Fe_5O_{12}$) (EuIG), should have PMA on any substrate orientation due to same sign of both anisotropy constants λ_{100} and λ_{111}. The second one, terbium iron garnet ($Tb_3Fe_5O_{12}$) (TbIG), should work only on GGG (111). Moreover, the bulk crystal of TbIG has its compensation temperature very close to room temperature [19], which presents another very interesting field of study.

9.1 Growth

Polycrystalline targets for the deposition of TmIG, TbIG and EuIG were prepared using the process described in detail in section 4.3. The starting deposition conditions were based on experience from previous growth of TmIG [80]. The vital point during the deposition was found to be the laser power. The maximum laser power available from the laser was 500 mJ in pulse at the laser output. Unfortunately, this was found insufficient during the first attempts to the growth of good quality garnets. The problem was found to be high loss of beam power in optical elements on the way to the deposition chamber. The loss was more than 70 percent of laser power. This problem was solved by the exchange of focusing optics which increased the laser flux in the chamber to almost double of the starting value. The optimal oxygen pressure during the deposition was found to be 150 mTorr in combination with substrate heater set point at 900 °C. Actual temperature at the substrate was expected to be about 250 °C lower. In addition, the effect of cooling rate on the film quality was studied. It was found that faster rates (10 °C·min^{-1}) yields layers with better crystallinity. For the purpose of optical and magneto-optical measurements, the target film thickness was chosen 40 nm. This thickness is sufficient to obtain good optical signal while the film remains fully strained. Actual thicknesses measured by XRR (inset in

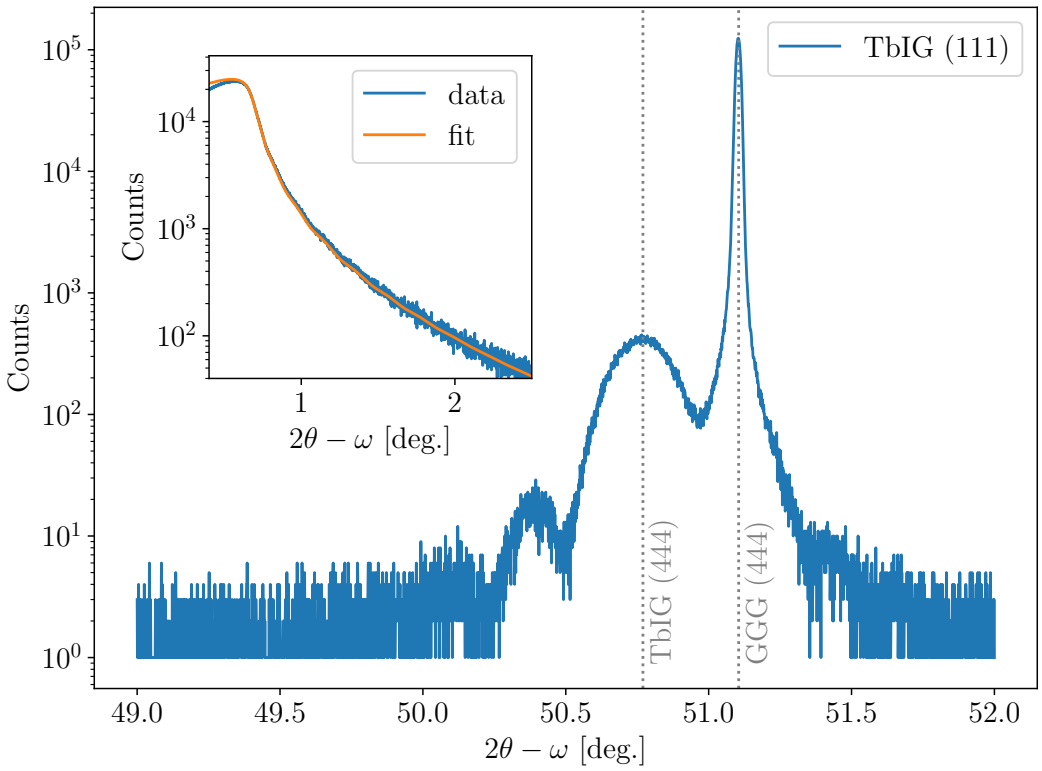

Figure 9.1: HRXRD pattern of (444) diffraction peak of TbIG film on GGG (111) substrate. Substrate and film peaks are indicated by dashed lines. Fringes are symmetrically on both sites of the film peak. The inset shows XRR measurement with fit.

Fig. 9.1) are shown in table 9.1. Since the same number of shots was used for all the depositions (20 000), one can see that deposition rate of all these materials is similar.

Material	Thickness [nm]	H_C [mT]
TmIG	36.8	0.3
TbIG	40.9	4
EuIG	40.8	1-20

Table 9.1: Physical properties of garnets presented in chapter 9.

9.2 Structural and magnetic characterization

The crystallinity of the grown samples was determined by HRXRD measurements in the vicinity of the substrate peak. The garnet peak is in all the cases next to the substrate peak. With exception of (440) diffraction, that is very weak, all the scan show very distinct Laue fringes symmetrically along both sides of the garnet peak. That indicates very good epitaxial quality of grown films. From the relative position of film and substrate diffraction peak one can see, that in the cases of TbIG and EuIG, the films are under compressive strain, while the

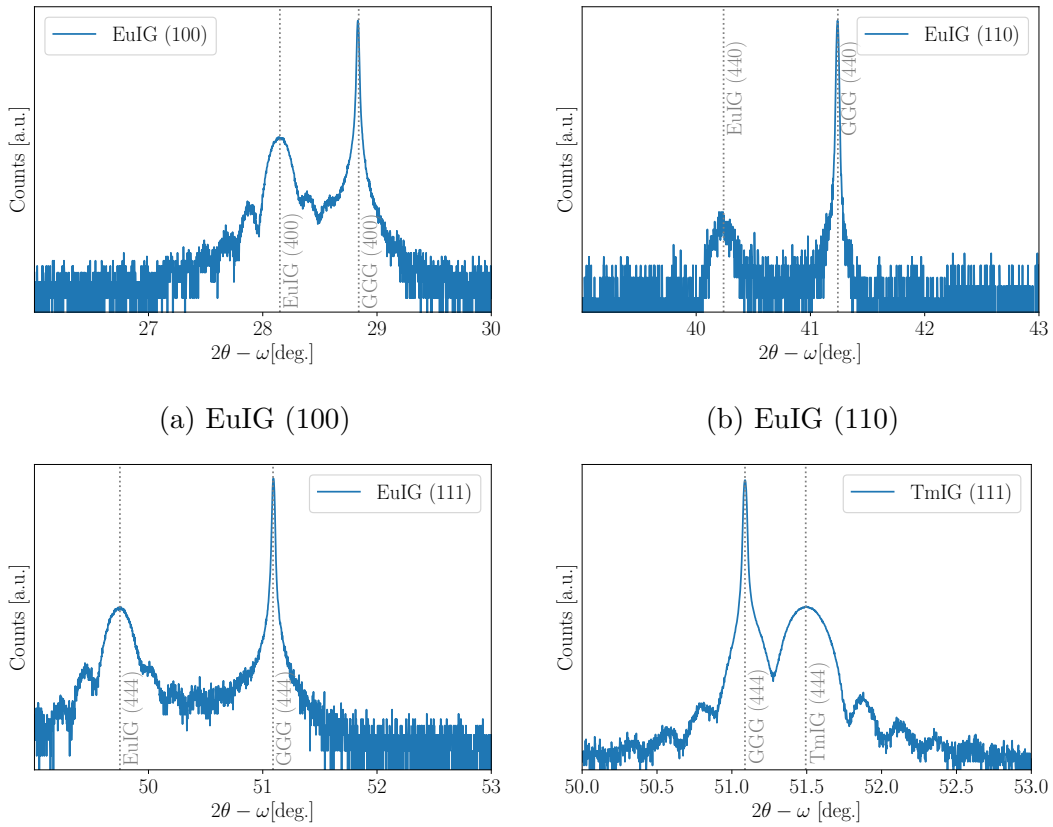

(a) EuIG (100)

(b) EuIG (110)

(c) EuIG (111)

(d) TmIG (111)

Figure 9.2: HRXRD pattern of EuIG film on (a) GGG (100), (b) GGG (110), (c) GGG (111), and (d) TmIG on GGG (111) substrates. Substrate and film peaks are indicated by dashed lines. Fringes are symmetrically on both sites of the film peak with exception of EuIG on GGG (110), where the reflection is too weak to resolve them.

TmIG is, on the other hand, under tensile strain. The strain state of films was confirmed by measurement of RSMs for some of the samples. One example for EuIG on GGG (111) is shown in Fig. 9.3. These measurements showed no sign of relaxation at this thicknesses. Another study on different set of samples showed that the films remained fully strained up to the thickness of 150 nm. This limit can be even more improved by control of stoichiometry. Compositional analysis was carried out on different set of samples deposited under same conditions using XPS [36]. These films show trends similar to samples in previous chapters. There is a significant iron deficiency and traces of RE elements in different oxidation states. However, XRD measurements do not point on the presence of any secondary phases. Therefore, the exceeding RE elements is incorporated in the garnet structure. Further information about present ionic states and occupancy of sublattices can be found in Ref. [36].

Magnetic properties of all samples were obtained by VSM. Both in-plane and out-of-plane loops of EuIG samples on different GGG substrate orientations are depicted in Fig. 9.4. The magnetic anisotropy of TmIG is demonstrated on out-of-plane loop in Fig. 9.5a. In the case of TbIG, the contribution of the film could not

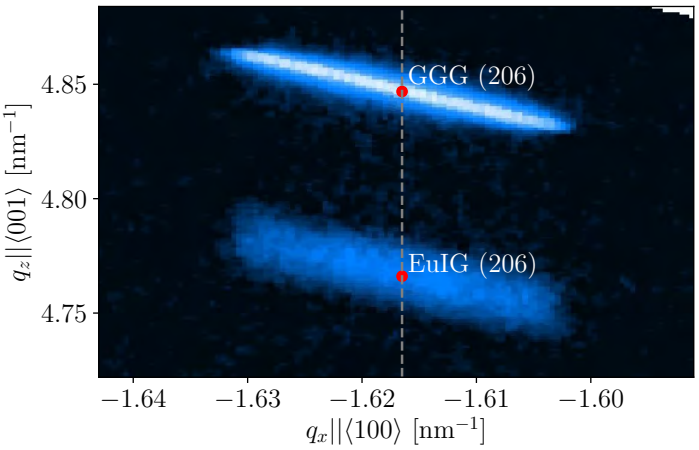

Figure 9.3: RSM of (206) peak of EuIG on GGG (111). Substrate and film peak centers are marked with red dots. Both peaks lay on same q_x (white dashed line) indicating in-plane lattice matching between the film and the substrate. Therefore, the film is fully strained.

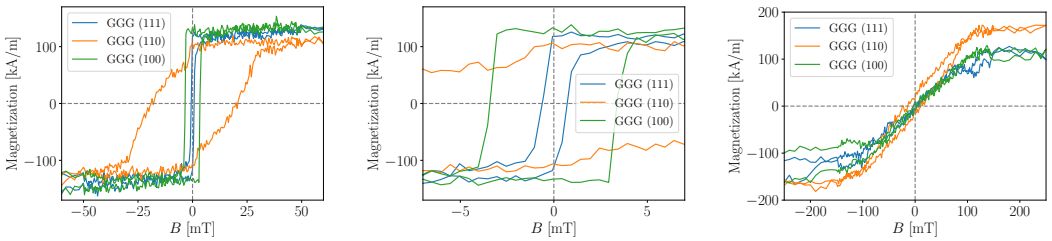

(a) Out-of-plane (b) Out-of-plane zoom (c) In-plane zoom

Figure 9.4: Room temperature magnetic hysteresis loop of EuIG films on GGG (100), GGG (110), and GGG (111) substrates with external magnetic field applied in (a, b) out-of-plane and (c) in-plane to the film plane. All films exhibit PMA. EuIG on GGG (110) shows more complicated magnetization reorientation.

be easily subtracted from the signal of the substrate due to its weak magnetization at the room temperature. Therefore, magneto-optical methods have been used to obtain information about its magnetic properties. The magnetic anisotropy and coercivity field were determined from polar MOKE loops depicted in Fig. 9.5b.

From the graphs, one can see that the easy-axis is pointing out-of-plane to the sample surface, while the hard axis lays in-plane. TmIG is the softest material with coercivity of less than 0.3 mT, which is even smaller than presented in literature [80]. Polar MOKE showed, that TbIG has this value around 4 mT. For EuIG on (100) and (111) substrate orientation, one can observe square loops with very low coercivity of 4 and 0.8 mT. The (110) orientation shows more complicated magnetization reorientation mechanism that is most likely connected to pinning of domain wall motion. In the case of (110) orientation, the straining of the film seems to be more complex, causing higher concentration of dislocations.

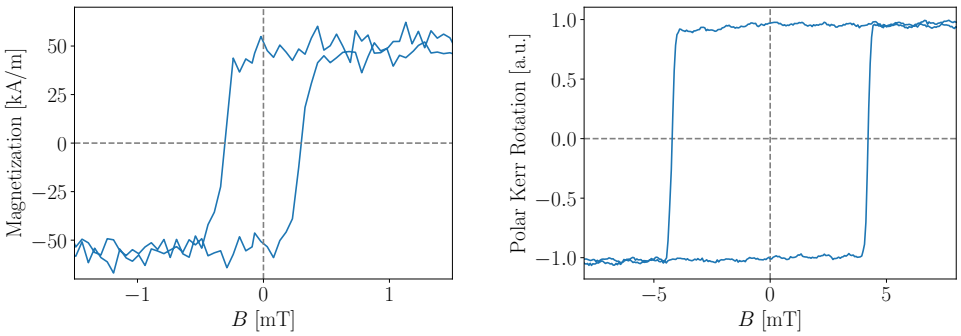

(a) TmIG (b) TbIG

Figure 9.5: (a) Room temperature magnetic hysteresis loop of TmIG film on GGG (111) substrate with the external magnetic field applied in out-of-plane to the film plane. (b) Faraday rotation hysteresis loop of TbIG film on GGG (111) substrate measured at 2 eV (635 nm). Both films exhibit PMA.

These dislocations act as pinning centers for the magnetic domain walls during the magnetization reversal. Saturation magnetization of all films is similar to bulk values [19]. Furthermore, the temperature dependency of magnetization of EuIG on (111) substrate (Fig. 9.6a) was measured. On can see in Fig. 9.6b that the magnetization shows almost linear increase of coercivity towards lower temperature and no change of M_S in the whole measured region. This behavior will be addressed in the next chapter, but it can be explained by the change of magnetoelastic anisotropy due to increase of strain caused by different expansion coefficients of the film and the substrate.

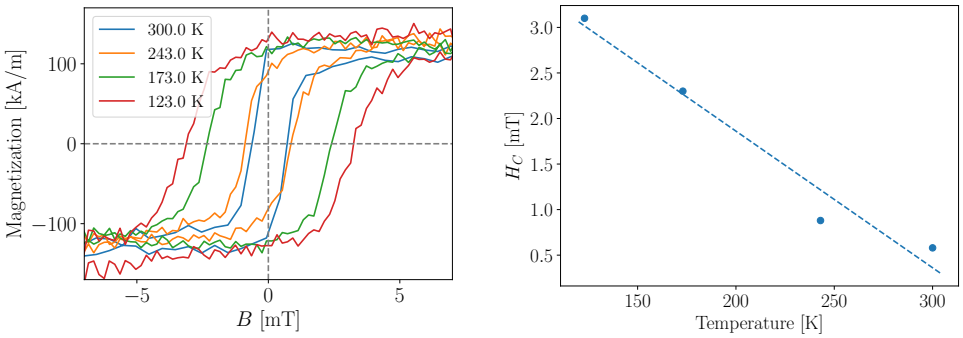

(a) M at different T (b) H_C versus T

Figure 9.6: (a) Magnetic hysteresis loops of EuIG on GGG (111) substrate at various temperatures. Hysteresis loops show increase of H_C with decrease of temperature, while M_S remains the same value. (b) H_C of EuIG on GGG (111) substrate as a function of temperature. Dashed line shows linear trend.

9.3 Optical properties

Optical properties of the films were investigated using spectroscopic ellipsometry. All materials were measured on single side polished substrates to avoid contri-

butions from back reflection. Measured angles were ranging between 55° and 70°. Optical constants of the substrates were obtained from separate measurements. The ellipsometric experimental Ψ and Δ were fitted together with optical transmission measurements to further improve the fit precision. Since the optical properties of these materials are not well documented in such broad spectral range, single layer described by B-spline [81] on GGG substrate was used as the starting model. This layer was afterwards parametrized by combination of 10 Tauc-Lorentz oscillators. Position of these transitions were based on Ref. [76] and further improved based on B-spline model. Resulting optical constants are depicted in Fig. 9.7. Following the figure, one can see a significant difference between TbIG and the rest of the garnets. The most of the films show similar spectral shape to Ce:YIG (Fig. 8.8). The main difference is caused by transitions near band edge that are stronger and broader in TmIG and EuIG, causing the shift of the absorption edge down to the infrared region. Therefore, TbIG is therefore much more transparent in infrared region than the other garnets. Above 3 eV the spectra of all samples are dominated similarly to other iron garnets by interband transitions mediated by Fe ions in octahedral and tetrahedral sites [20]. Due to similarity of optical properties of these films to YIG, there are no significantly contributing specific transitions of RE elements in the measured region.

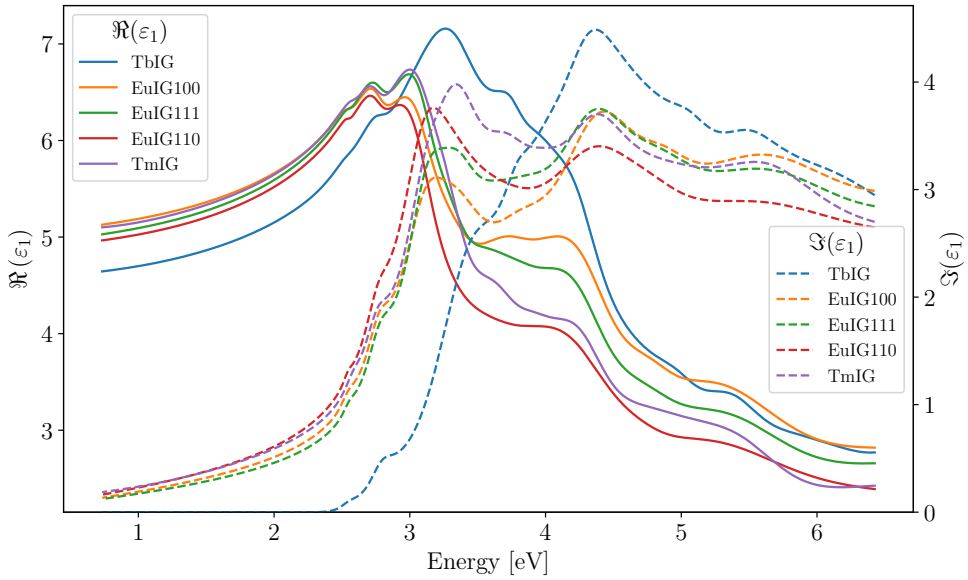

Figure 9.7: Spectral dependence of diagonal elements of permittivity tensor, ε_1, of TmIG on GGG (111), TbIG on GGG (111), and EuIG on GGG (100), GGG (110), and GGG (111) substrates.

9.4 Magneto-optical properties

Experimental spectra of Faraday rotation and MCD of all films were measured in broad range from 0.7 to 6.5 eV (Fig. 9.8). There was no significant effect at

room temperature below 2.4 eV; therefore, it is not shown in the graph. Due to optical properties of these films shown above, the Faraday effect could not be measured above 4.25 eV. Opposite sign of the Faraday effect of TbIG is due to difference in the dominant magnetic sublattice, because unlike other garnets, TbIG film is at room temperature below the compensation point. Therefore, its sublattices are oriented in external magnetic field anti-parallelly in comparison to the others, which causes change of sign of the magneto-optical effects. Due to higher sensitivity of magneto-optics to rare-earth specific transitions, one can see significant differences in spectral features. The most dominant is the one originating from Tb^{3+} situated near 3 eV. RE specific transitions have paramagnetic character which confirms the origin of the observed spectral changes. Otherwise, the magneto-optical response is dominated by the same set of transitions originating in crystal field split electron levels at Fe sublattices. Detailed description of magneto-optical response using microscopic models in performed in Chapter 11. The difference in Faraday spectra between EuIG films on various substrate orientations points to slightly different occupancy of iron sublattices. Since the samples were grown during the same deposition process, one can assume that this effect is caused strictly by orientation of the substrate.

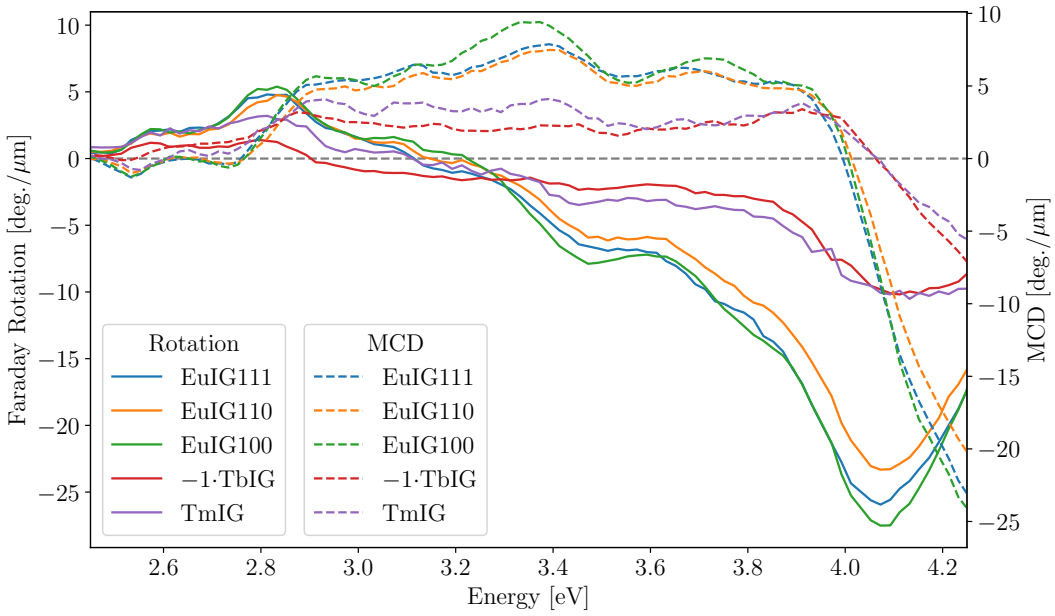

Figure 9.8: Room temperature spectral dependence of Faraday rotation and MCD of TmIG on GGG (111), TbIG on GGG (111), and EuIG on GGG (100), GGG (110), and GGG (111) substrates. Spectra of TbIG (red lines) are shown with opposite sign.

Measurements of spectral dependencies of polar MOKE are shown in Fig. 9.9. For a better comparison, all the data shown in this figure were acquired on samples grown on (111) GGG substrates. In the region below 3 eV, the penetration length of light exceeds the thickness of the film causing the difference to be a combination of optical properties with the film thickness. The only difference in magneto-optical response which is not visible in Faraday measurements is therefore situated in region above 4 eV. The spectral features at these photon

energies originate from iron crystal field and therefore suggest that occupancy of octahedral and tetrahedral are influenced by the RE element. That would be in agreement with studies showing presence of RE elements in other than dodecahedral sites [36].

In conclusion, three different RE garnets were prepared in the form of thin films on GGG substrates. All of these exhibit PMA. With exception of EuIG on GGG (110), all samples show very small coercivity fields making them excellent candidates for magnetic domain wall motion experiments. Optical properties of these films are comparable to other commonly used garnet materials featuring very low absorption in IR region. Magneto-optical response is very similar to YIG without significant presence of RE element specific transitions with exception of TbIG which exhibits new feature around 3eV.

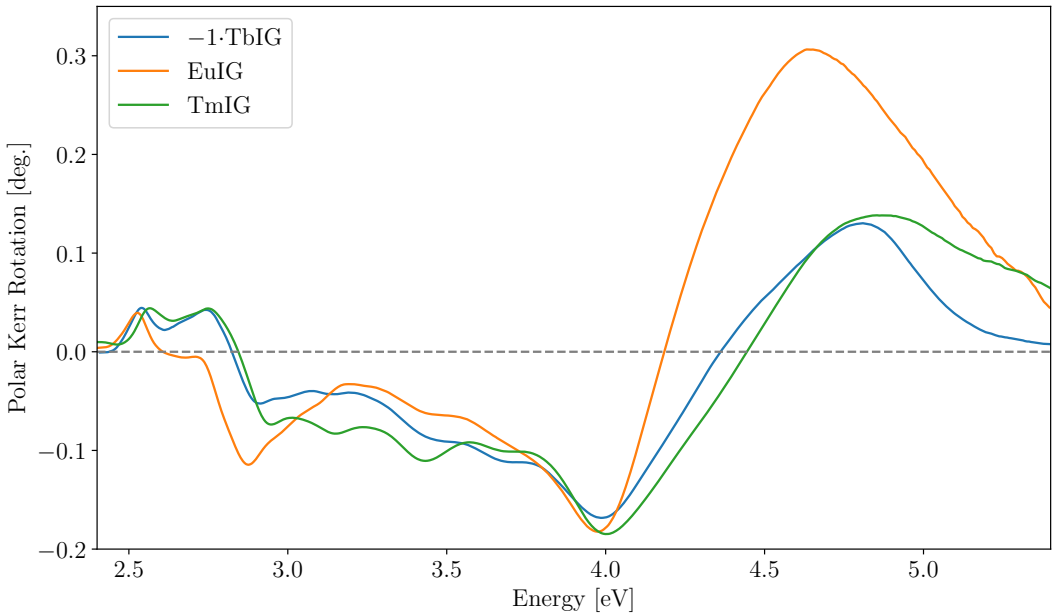

Figure 9.9: Room temperature spectral dependence of polar Kerr rotation of TmIG, TbIG, and EuIG on GGG (111) substrates. Spectrum of TbIG (blue line) is shown with opposite sign.

10. Temperature dependent physical properties of garnet thin films

So far, temperature dependent studies of physical properties of garnets were mostly focused on bulk materials [82, 83, 84]. These works show increase of saturation magnetization as well as magneto-optical response at low temperatures. Detailed information about magnetocrystalline anisotropy and magnetostriction of thin garnet films at low temperatures were not reported yet. This chapter is therefore dedicated to the systematical study of temperature dependence of optical and magneto-optical properties together with magnetic and structural characterization.

10.1 Anisotropy reorientation of $Ce_1Y_2Fe_5O_{12}$

Chapter 8.2 showed the important aspects of Ce:YIG that make it interesting for future application; however, it focused only at its physical properties at room temperature. To add up to these results, sample for this study, that focuses on temperature dependence of its physical properties, was deposited the same way as the films presented in chapter 8.2. This particular film composition of the sample was determined by WDS to be $Ce_{0.59\pm0.18}Y_{2.86\pm0.41}Fe_{4.55\pm0.5}O_{12}$. Its thickness measured by XRR was 80 nm.

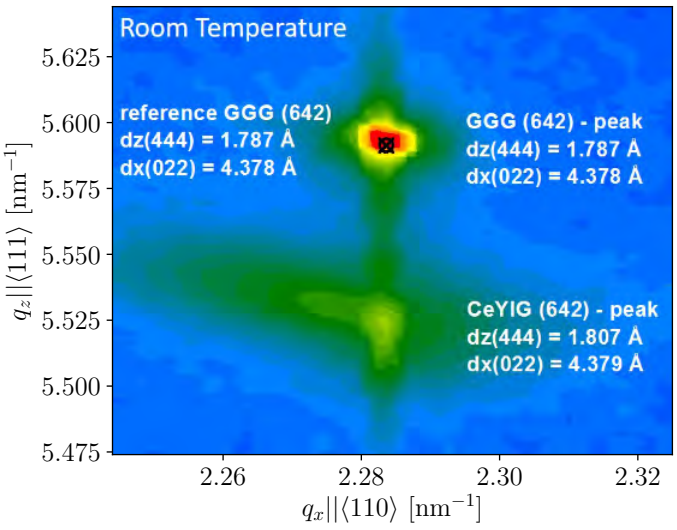

Figure 10.1: Room temperature RSM of (642) peak of Ce:YIG on GGG (111) substrate. Position of peaks indicate that the Ce:YIG film is almost fully strained with minor strain relaxation towards lower q_x.

The staining of the film by the GGG substrate was determined by measurement of RSM at room temperature (Fig. 10.1). The RSM of the (642) peaks

indicates that the Ce:YIG film is almost fully strained with minor strain relaxation towards lower q_x and well matching in-plane to the GGG lattice. The out-of-pane lattice constant is higher than the in-plane and indicates that the film is rhombohedrally distorted with tensile strain along out-of-plane direction (more details below). Obtained lattice parameters are comparable with bulk material of similar composition ($a = 12.44 \pm 0.01$ Å).

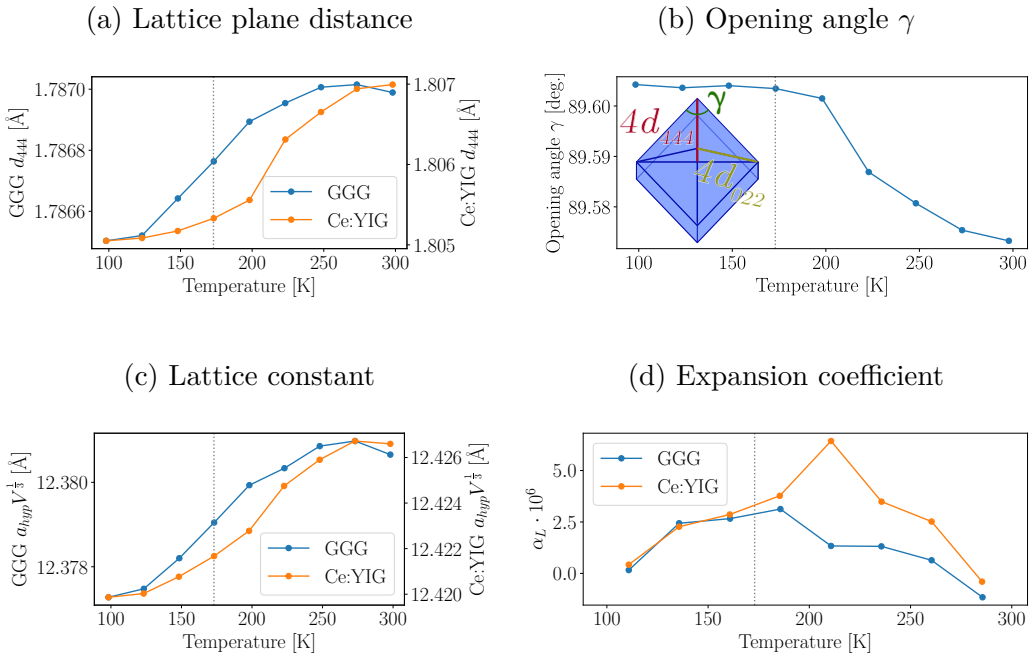

Figure 10.2: Temperature dependence of (a) the d_{444} out-of-plane lattice plane distance of the film, (b) the calculated facet angle γ of the rhombohedrally distorted unit cell, (c) the calculated lattice constant for GGG and the pseudocubic lattice constant for Ce:YIG, and (d) the thermal expansion coefficient of the film and the substrate for Ce:YIG film on GGG (111) substrate.

Measurement of XRD $\omega - 2\theta$ scans was carried out in temperature range from 77 K to 300 K. The results depicted in Fig. 10.2 show significant difference of thermal expansion between the film and the substrate. The relative change of the lattice plane distance d_{444} of Ce:YIG film over the whole temperature range is more than two times larger than for the substrate even though they follow the same trend. Looking at the opening angle γ (Fig. 10.2b), one can see nearly linear increase down to 200 K. Below that, the γ remains constant. Since the in-plain compressive strain is the cause of the rhombohedral distortion, the increase of γ with decrease of temperature indicates the decrease of in-plane compressive strain. The temperature 200 K is also the limit, above which the expansion coefficient (Fig. 10.2d) of Ce:YIG is higher than the one of GGG. Until that point, they are fairly similar.

Temperature measurement of magnetic hysteresis loops of Faraday rotation at 0.8 eV (1550 nm) was performed in temperature-controlled microscopy stage positioned between the poles of electromagnet. Hysteresis loops at 300 K and 77 K are shown in Fig. 10.3. These measurements were used to determine temperature dependence of saturated Faraday rotation, coercivity field H_C and anisotropy field

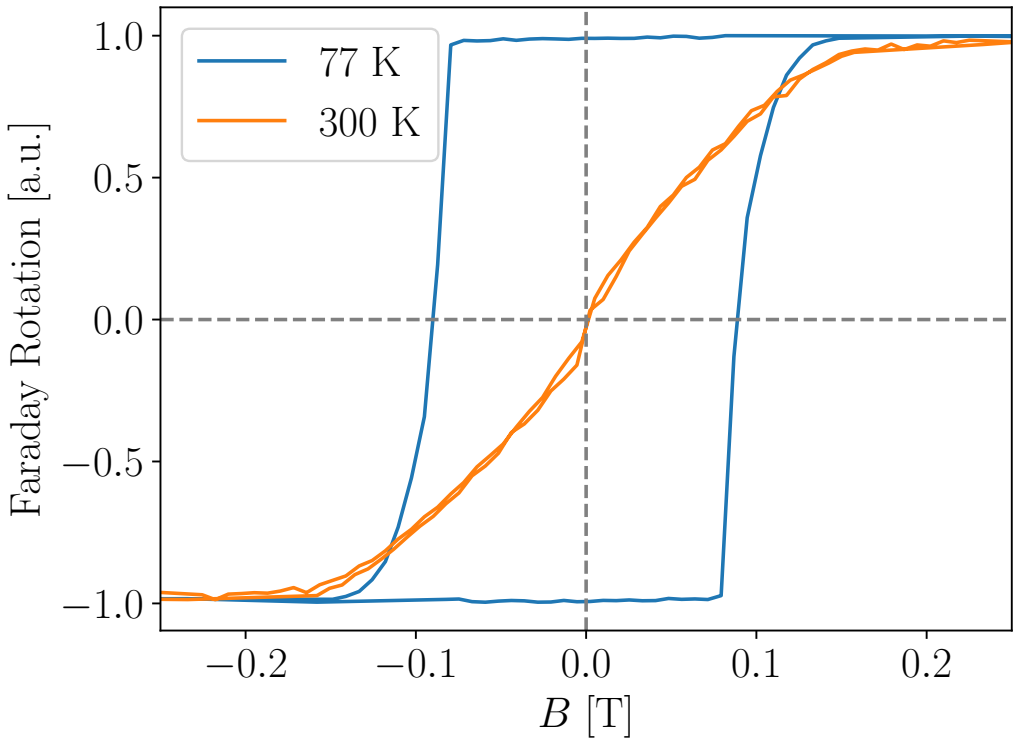

Figure 10.3: Faraday rotation hysteresis loops of Ce:YIG film on GGG (111) substrate measured at 0.8 eV (1550 nm) for 77 K and 300 K.

H_{sat} shown in Fig. 10.3. Loops of Faraday rotation show the magnetic anisotropy reorientation, where magnetization easy-axis turned out-of-plane below 170 K. The following effect is a significant increase of coercivity field reaching up to 100 mT at 77 K. The anisotropy field has clear minimum at 170 K, where the reorientation of magnetic anisotropy occurs. Saturated Faraday rotation increases toward the low temperatures which is caused by paramagnetic origin of transitions in near IR spectral region.

To investigate possible changes in electronic structure with temperature, spectral dependencies of FR and MCD were acquired at 77 K and 300 K (Fig. 10.5). Due to observed changes in coercivity field, external magnetic field of 0.8 T was applied during the measurements to ensure the magnetic saturation of the film. Since the spectra are normalized to the thickness of the film, one can see similar spectral behavior with the Faraday spectra presented in the chapter 8.2. Therefore, the origin of the spectral features will not be discussed and the focus is only on the effect of the temperature.

The spectral feature situated near 1.4 eV originates from intrinsic transitions in Ce^{3+}. Therefore, the significant increase in amplitude is consistent with their paramagnetic character. At low temperature, new spectroscopic structure near 1.9 eV appears. It does not show significant increase of amplitude at low temperature; therefore, its origin cannot be from Ce^{3+}. Moreover, the second excited state $5d^2$ of Ce^{3+} has higher energy and the sign of this spectroscopic feature is opposite to the one at 1.4 eV. In the case of thick YIG films [85], transition originating from iron crystal field was observed at similar photon energies. These

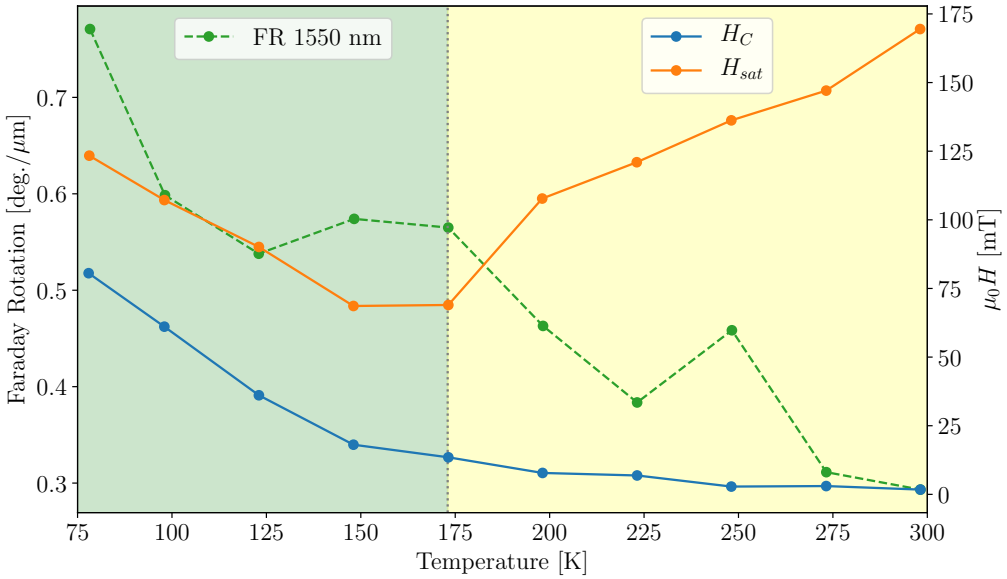

Figure 10.4: Temperature dependence of H_C, H_{Sat} and saturated Faraday rotation of Ce:YIG film on GGG (111) substrate determined from Faraday hysteresis loops measured at various temperatures.

transitions are spin-forbidden and therefore not visible at the room temperature. However, the presence of Ce^{3+} causes at low temperature resonant increase of magneto-optical response around 1.9 eV rendering this feature visible.

In the spectral region above 2.5 eV, the Faraday spectra resembles previously observed features of both Ce:YIG (ch. 8.2, 8.3) and Bi:YIG (ch. 8.1, 8.4). Amplitude of the effect is slightly higher at 77 K, which can be explained by small increase of magnetization.

10.2 Magneto-optical behavior near the compensation temperature

The compensation temperature of ferrimagnetic material in very useful property for several spintronic applications, especially when the material does not require cryogenic cooling to reach this temperature. According to literature, compensation temperature of bulk TbIG lies at 250 K. However, its exact value is strongly correlated with exact composition [86, 87]. Therefore, extensive study of magneto-optical response of this particular material was performed in wider temperature range. Focusing on an estimation of precise T_{Comp} value, temperature dependence of magneto-optical effect ranging from 5 K to 340 K was performed in a broad spectral region. The spectra of Faraday rotation depicted in Fig. 10.6 show the change with temperature of both amplitude and spectral shape over whole measured range. Such difference cannot be explained by simple magnetization increase, but also by presence of paramagnetic transitions situated around 3 eV. Since the spectral shape of such transitions is very wide in Faraday rotation, polar Kerr spectrum, where this effect is more pronounced, is more favorable for

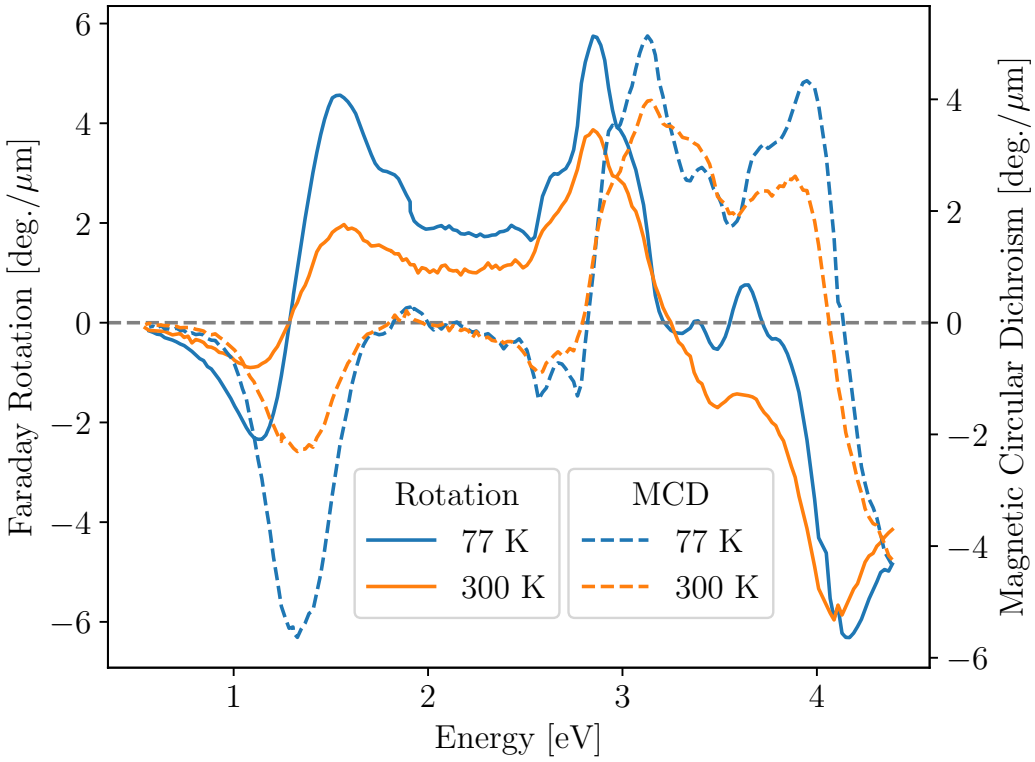

Figure 10.5: Spectral dependence of Faraday rotation and MCD of Ce:YIG on GGG (111) substrate measured at 77 K and 300 K. Increase of amplitude of Faraday effect in near IR spectral region is originating from paramagnetic character of electric dipole transitions of Ce^{3+}.

the analysis (Fig. 10.7). However, there is no sign change of magneto-optical effect that would be expected near compensation temperature. Therefore, the studied temperature range was further extended to higher temperatures. Detailed measurement of Faraday effect above the room temperature is shown in Fig. 10.8. At temperature of 316 K one can see clear drop of magneto-optical response and its reversal above this point.

These measurements showed that the reversal of sign of the effect occurs more than 80 K higher than expected. Based on this measurement, one can see, that there is no sudden swap of the sign, but at the temperature of 316 K the magneto-optical response renders zero. At this point of nearly compensated antiferromagnetic ordering, the applied external field used during the measurement was not sufficient to keep magnetic order and the film broke into small magnetic domains. Since the measurement area is about 1 mm wide, the sum of Faraday effect is close to zero. Narrowness of the transition window was achieved by heating of the sample in magnetic field without its sweeping during the measurement. Same temperature range was probed by the means of polar MOKE (Fig. 10.9). This time the field was swept at every measured temperature. One can see, that lowering of magneto-optical response occurs in much wider temperature window. The flat area, where there seems to be no MOKE is regime, where sweeping of the field does not cause any change in domain structure. Since the magneto-optical spectra are obtained from subtraction of signals of opposite

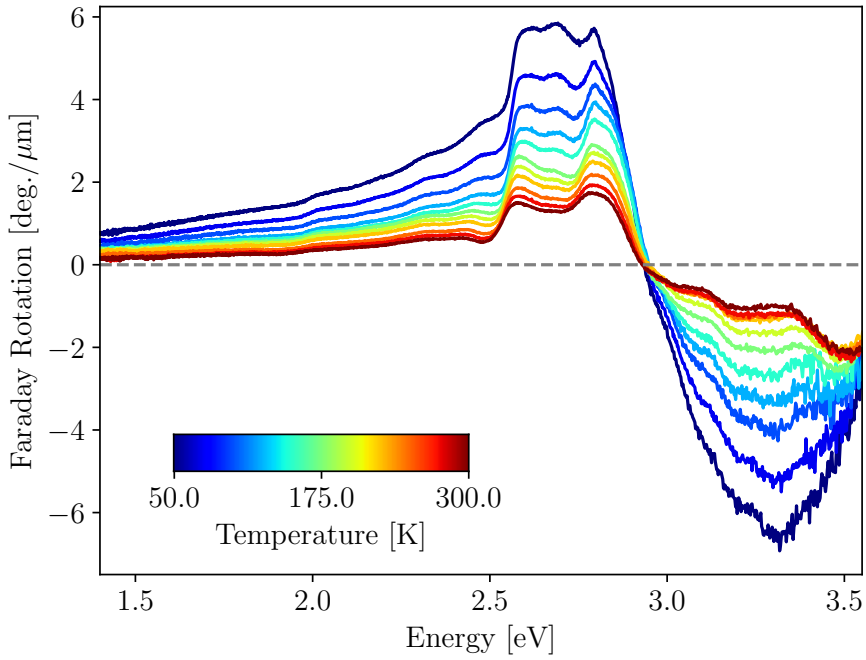

Figure 10.6: Spectral dependence of Faraday rotation of TbIG film on GGG (111) substrate measured from cryogenic temperatures up to the room temperature. The strong temperature dependence originates from broad paramagnetic transitions of Tb^{3+} situated around 3 eV.

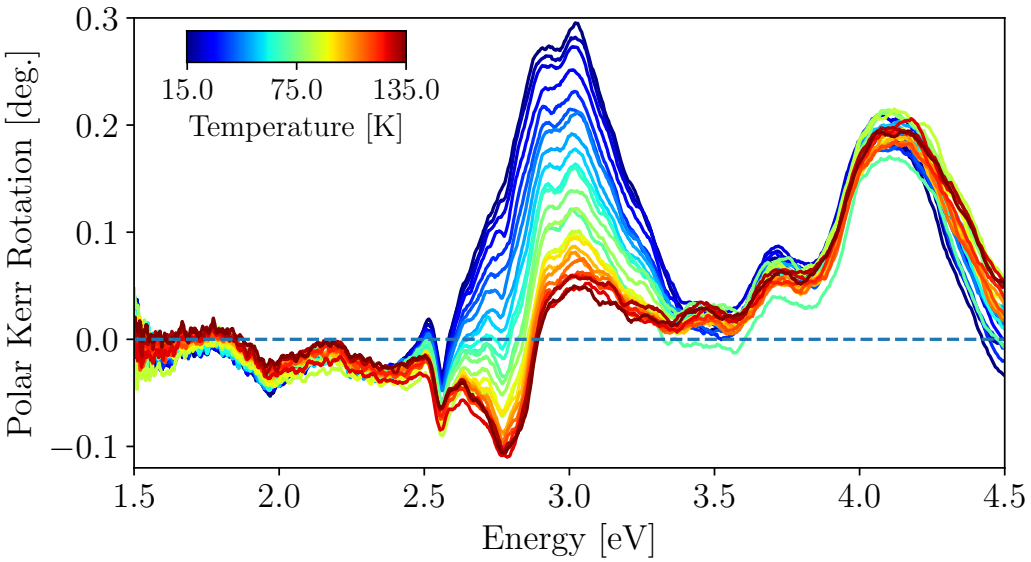

Figure 10.7: Spectral dependence of polar Kerr rotation of TbIG film on GGG (111) substrate measured from 15 K to 135 K. The strong temperature dependence originates from paramagnetic transitions of Tb^{3+} situated around 3 eV

external magnetic fields, these measurements show zero effect (details below). Comparison of these two switching techniques can be seen in Fig. 10.10. Despite

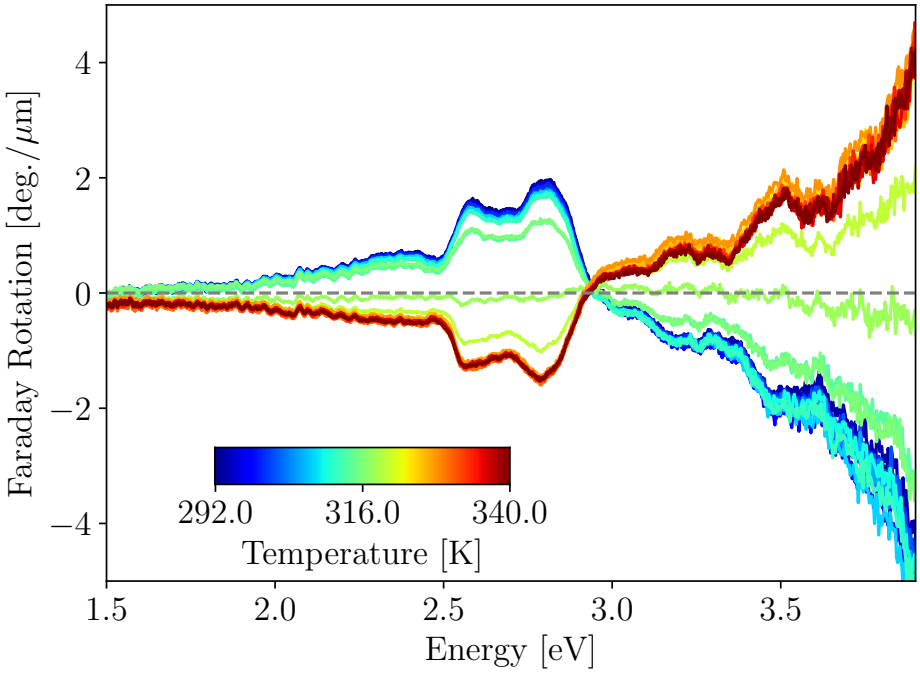

Figure 10.8: Spectral dependence of Faraday rotation of TbIG film on GGG (111) substrate measured from 292 K up to 340 K. The sign change of the magneto-optical effect is caused by change of dominant magnetic sublattice due to transition through compensation temperature.

the difference in switching described above, the sign change occurs at significantly different temperatures. That is most likely due to usage of different sample for these measurements. These samples were prepared during the same deposition cycle; however, the sample used for MOKE measurement was on a single side polished substrate and the second sample used for the Faraday measurements was on a double side polished substrate. This causes difference of substrate temperature during the deposition caused by change of effectivity of radiation heater based on roughness of the back side of the substrate. Therefore, these samples might slightly differ in stoichiometry that could lead to shift of the compensation temperature. However, this phenomenon was in the time of finishing of this thesis still under investigation.

As a reminder, the magneto-optical effect linear in magnetization is subtracted from the measured signal using its symmetry in magnetization. Magneto-optical angle is obtained from two measurements with opposite sign of external magnetic field

$$\Phi(\vec{B}) = \frac{\varpi(\vec{B}) - \varpi(-\vec{B})}{2}, \tag{10.1}$$

where $\varpi(B)$ denotes measured angle at external magnetic field of B. This technique requires the external magnetic field to be sufficient to saturate the magnetization of the measured sample. The spectral dependence of the magneto-optical effect of a garnet is superposition of contributions from each individual magnetic sublattice. Since each sublattice consist of atoms with different band structure,

their contribution into spectrum will differ. To change the sign of the magneto-optical spectrum, all sublattices have to reverse their orientation towards external magnetic field. If only one of the sublattices reversed or tilted, there would be significant change of spectral shape. Therefore, lowering of amplitude of both, Faraday and polar MOKE effect, has to originate from different mechanism. A ferrimagnet at its compensation temperature has near-antiferromagnetic ordering of its magnetic sublattices. Therefore, the net magnetization is zero and its magnetic state cannot be influenced by the external magnetic field. This explains the measured zero magneto-optical effect at the compensation temperature. The equation 10.1 requires a change upon reversal of the external magnetic field to be non-zero. In the case of Faraday effect, constant magnetic field kept the magnetic domain structure until it had the tendency to reverse due to transition through the compensation temperature. Therefore, the measured spectra show sudden step above the compensation temperature. The lowering of the the amplitude in this scenario is caused by insufficient external magnetic to keep the magnetic order causing nucleation of magnetic domains of opposite sign, that effectively lower the measured magneto-optical response. In case of polar MOKE measurement, continuous sweeping of magnetic field at different temperatures leads to pinning of domain walls during the switching, that cannot be further moved with provided external magnetic field due to decrease of net magnetization. This effect continues up to the compensation temperature, where the change of the external magnetic field does not cause any change of magnetization in the film. After this point, domain walls start to unpin with the increase of the net magnetization until the point, when the whole film can be switched again.

The Fig. 10.10b can be used to interpolate the exact position of zero effect. The single side polished and double side polished sample had the compensation temperature at (307.6 ± 0.2) K and (317.8 ± 0.1) K, respectively. If we try to compare these finding from measurements from VSM on similar sample ($T_{Comp} = 330 \pm 10$ K) [36], we obtained the value that is more precise by almost two orders of magnitude. This shows the magneto-optical spectroscopy as excellent tool for probing of magnetic ordering in ferrimagnets where net magnetic moment can be near zero and therefore unavailable for measurement by magnetometry.

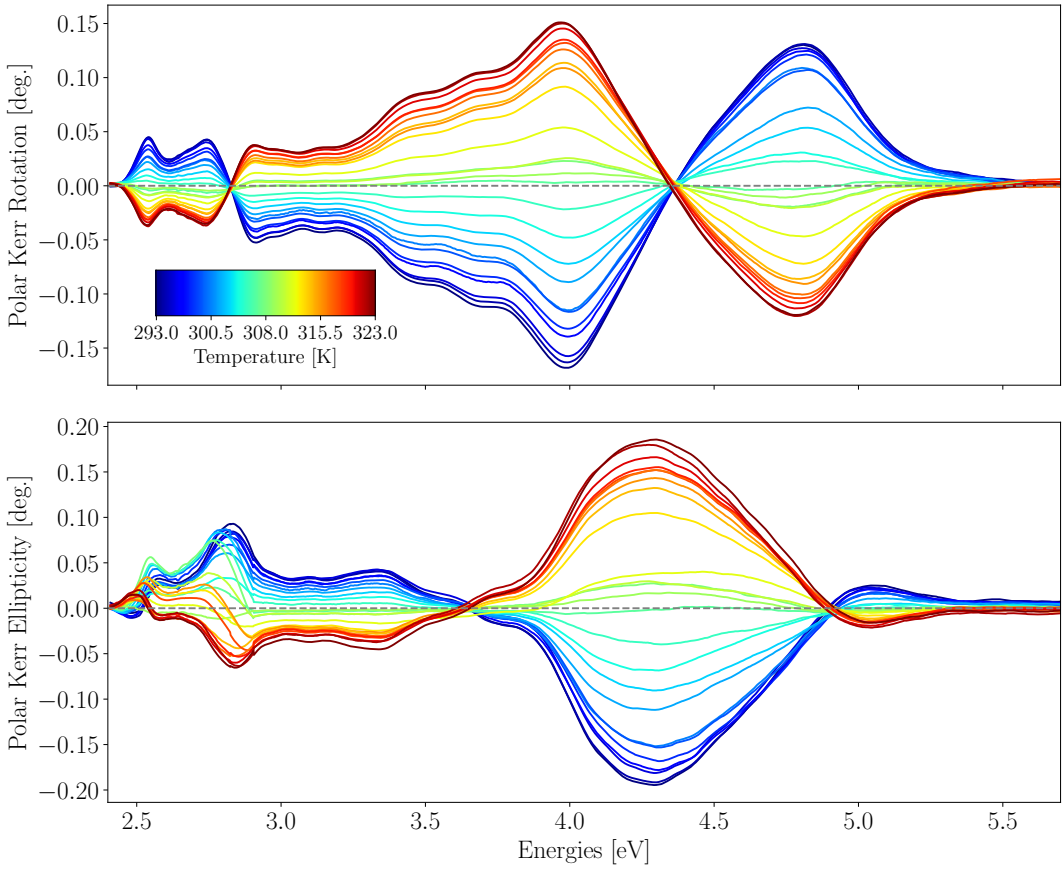

Figure 10.9: Spectral dependence of polar Kerr rotation of TbIG film on GGG (111) substrate measured from 293 K up to 323 K. The sign change of the magneto-optical effect is caused by change of dominant magnetic sublattice due to transition through compensation temperature.

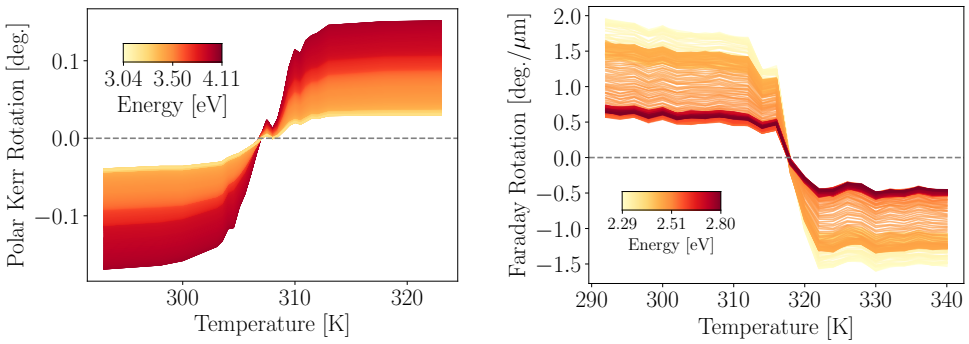

(a) Field swept at each temperature. (b) Field kept on during the heating up.

Figure 10.10: Saturated (a) polar Kerr rotation and (b) Faraday rotation as a function of temperature for various photon energies. The change of sign indicates the compensation temperature.

11. Modeling of magneto-optical spectra

The explanation of magneto-optical response of studied materials was so far limited to quantitative description of observed features and their comparison with known similar systems. The magneto-optical modeling provides, in the case of garnet structure, unique tool for describing each magnetic sublattice individually. Each magnetic atom in the lattice is surrounded by different oxygen symmetry and therefore it is possible to separate their contribution to magneto-optical spectra. To analyze the origin of the magneto-optical response in more detail, one has to introduce an adequate model which can describe experimental data. Used model was based on semiclassical approach described in chapter 3.4. The main goal was to build a robust model, that can fully describe experimental spectra. The model provides information about contribution of sublattices into magneto-optical response allowing their separation in measurements. Furthermore, this model was used to study the behavior or sublattices through magnetization reversal and temperature change. This study was limited to TbIG only for its T_{Comp}. However, similar procedure could be done also for other garnets described in previous chapters.

The model was build upon two sets of data. The Faraday spectra can be used as they are, since the substrate is already subtracted from the measurements. On the other hand, the experimental polar MOKE spectra must be further processed since system of thin film on substrate contains a lot of signal from interference. The data were processed using Yeh's formalism (section 1.4) and with the knowledge of diagonal elements of permittivity tensor obtained from spectroscopic ellipsometry, the spectral dependencies of the off-diagonal elements, ε_2 were deduced. These spectra can be modeled with transitions described in chapter 3.4.

As a first step, we used an model consisting of transitions found by spectroscopic ellipsometry. These transitions are summarized in Tab. 11.1a. With respect to different selection rules, not all of these transitions might be visible in the magneto-optical response. One can also look at the similar systems reported in literature [20]. This work reported six magneto-optically active transitions of YIG in narrower spectral range (see Tab. 11.1b).

Finally, the knowledge of temperature dependent changes in magneto-optical spectra was utilized. Looking at spectral features that have strong temperature dependency, one can further distinguish between diamagnetic and paramagnetic transitions. The final model consists of ten transitions as listed in Tab. 11.2. Corresponding sublattice was determined by the type of transition and its sign. Transitions from dodecahedral sites are know to have paramagnetic character. Tetrahedral and octahedral transitions are both diamagnetic. Furthermore, octahedral and dodecahedral sublattices are ordered parallelly and therefore their transitions have the same sign [19, 20]. Agreement of this model with experimental data obtained at the room temperature is depicted in Fig. 11.1. One can see that the model has excellent agreement with the experimental data and describes even very fine spectral features. This was the only measurement of Faraday effect in this chapter without a cryostat. Therefore, the other measurement have

n	A	Γ	E_0
1	0.80	2.66	0.98
2	1.35	0.24	2.79
3	8.71	0.63	3.43
4	1.55	0.35	3.79
5	2.44	0.53	4.00
6	5.89	0.68	4.31
7	4.18	1.00	4.67
8	0.69	0.55	5.05
9	0.55	0.53	5.51
10	26.0	4.00	6.17

(a) Optical transitions

n	Type	E_0
1	${}^6A_1 \rightarrow {}^4T_2$	2.46
2	${}^6A_1 \rightarrow {}^4E, A_1$	2.56
3	${}^6A_{1g} \rightarrow {}^4E_g, A_{1g}$	2.66
4	${}^6A_{1g} \rightarrow {}^4T_{2g}$	2.79
5		3.12
6		3.40

(b) Literature

Table 11.1: (a) Parameters of Tauc-Lorentz oscillators describing optical transitions contributing to the optical response of TbIG film on GGG (111) substrate. (b) Transitions contributing to magneto-optical response of YIG according to the literature [20].

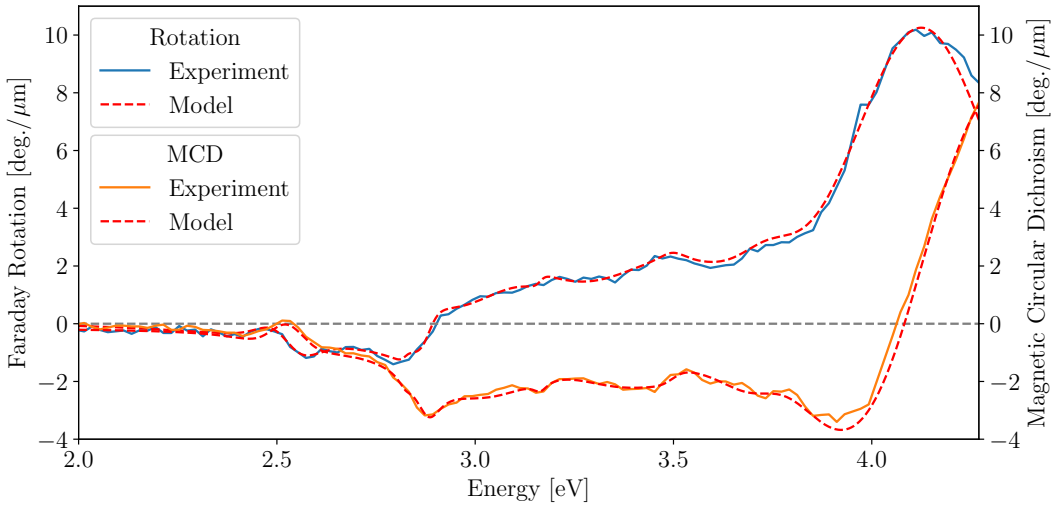

Figure 11.1: Room temperature spectral dependence of Faraday rotation and MCD of TbIG film on GGG (111) substrate compared with theoretical model.

more noise in UV region due to optical loss on the windows. The comparison of figures 11.1 and 11.2a further demonstrates the reproducibility of used measurement technique. The performance of model for various temperatures is shown in Fig. 11.2 and 11.3. These figures show robustness of the model since its agreement with experimental data remains even at different temperatures. Comparison of the tables 11.1a and 11.2 shows, that only several transitions observed by optical analysis are present in the magneto-optical model. Due to usage of Faraday effect for the modeling, transitions in UV region are unaccessible due to limit in the sample's transmission. To overcome this limitation, temperature dependance of spectra of polar MOKE (Fig. 10.9) were measured. Calculated off-diagonal term of permittivity tensor is depicted in Fig. 11.4. The same theoretical model was

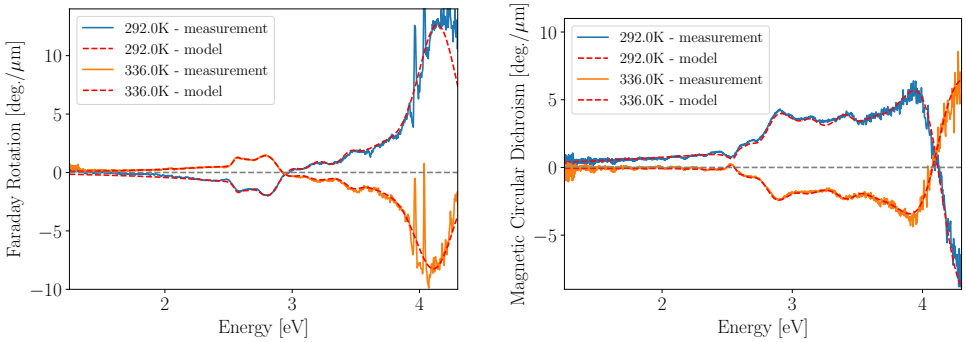

(a) Faraday rotation (b) Magnetic Circular Dichroism

Figure 11.2: Spectral dependence of (a) Faraday rotation and (b) MCD of TbIG film on GGG (111) substrate measured symmetrically around the compensation temperature compared with theoretical model.

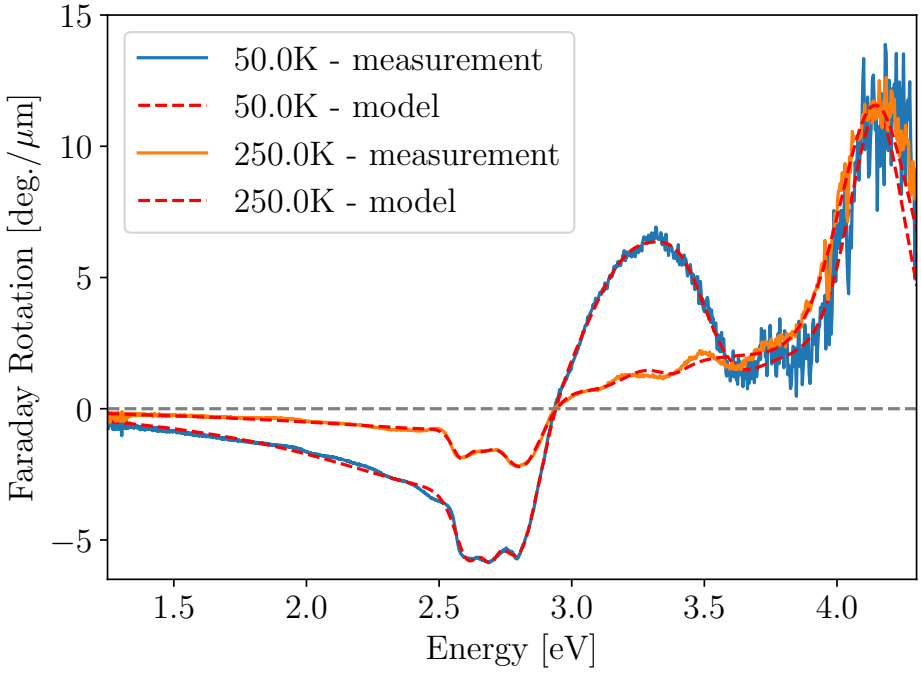

Figure 11.3: Spectral dependence of Faraday rotation of TbIG film on GGG (111) substrate measured at 50 K and 250 K compared with theoretical model.

applied on these data to extend its spectral coverage. The modified model was used to calculate the Faraday effect to study the changes introduced by extension of the spectral region. The comparison of the calculation with experimental data is shown in Fig. 11.5. Even though there is worse agreement between the model and the experimental data, the main difference occurs at high energies. This can be addressed to sensitivity of MOKE to surface, especially in UV region. Furthermore, the high optical absorption in this spectral region might cause lowering of the observed Faraday effect at the upper limit of the measured spectral region.

Working model can be used for further analysis of magneto-optical response.

n	E_0	Type	Sublattice
1	2.58	Dia	Octahedral
2	2.66	Dia	Octahedral
3	2.81	Dia	Octahedral
4	2.95	Dia	Tetrahedral
5	3.00	Para	Dodecahedral
6	3.12	Para	Dodecahedral
7	3.30	Para	Dodecahedral
8	3.41	Dia	Tetrahedral
9	3.60	Dia	Octahedral
10	4.15	Dia	Tetrahedral

Table 11.2: List of transitions used for modeling of magneto-optical response of TbIG.

Using knowledge of magnetic sublattice of each transition, one can separate their contribution to overall magneto-optical effect as shown in Fig. 11.6. The most noticeable transition is coming from dodecahedral site and due to its amplitude and broadness it covers the whole measured region. One can see it is dominant, especially at low temperatures, where it reaches even far into infrared region. Furthermore, the very narrow spectral features situated between 2.5 and 3 eV originate at octahedral site of iron, rendering them perfect for tuning of experiments for this specific sublattice. Tetrahedral site is on the other hand dominant near UV region. The other tetrahedral transition situated near 3 eV is significant as well; however, due to the strong temperature dependence of dodecahedral sublattice in this spectral region it presents the worse choice.

The modeling is not limited only to the spectra at different temperatures, but one can also look at magnetization dynamics. An example of the separation on spectra measured at different external magnetic fields is shown in Fig. 11.7. Each magnetic hysteresis loop show distinct steps at same fields corresponding to displacement of the domain wall. This illustrates the united magnetic behavior of magnetic sublattices and demonstrates the coupling between them. Even though there are reports showing that one of the sublattices is switching at smaller fields than the others [88]. This observation demonstrates that the switching occurs via domain structure where sublattices keep their alignment.

In conclusion, the constructed model of magneto-optical response of TbIG shows excellent agreement with measured experimental data. Its performance was proved at various temperatures and it described the behavior around the compensation temperature. This model allows separation of magneto-optical response of individual magnetic sublattices that can be further used for their study in static as well as dynamic regime. This was proved by modeling of magnetization reversal at room temperature. The result showed that the switching mechanism is propagation of magnetic domains rather than tilting of individual sublattices.

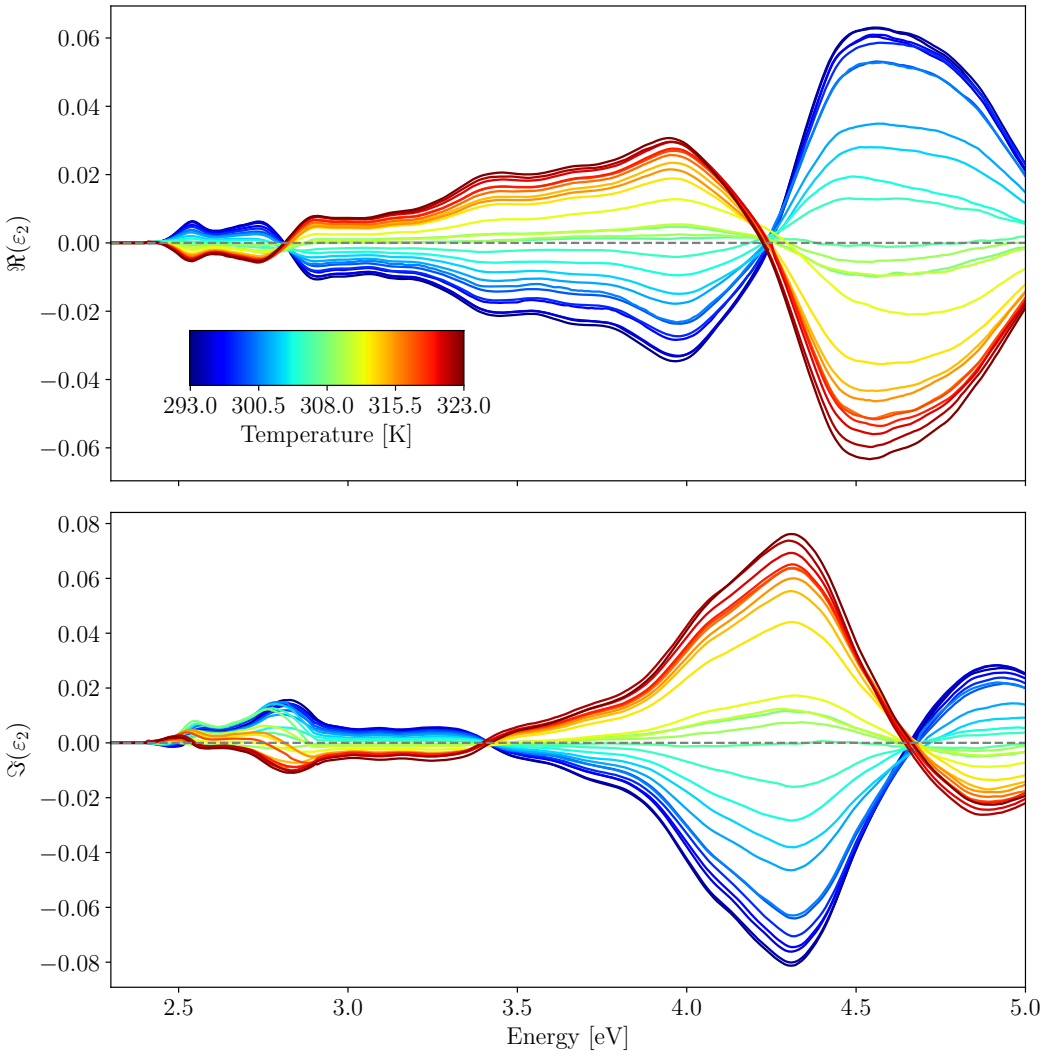

Figure 11.4: Spectral dependence of off-diagonal elements of permittivity tensor, ε_2, of TbIG film on GGG (111) substrates calculated for temperature range from 293 K to 323 K.

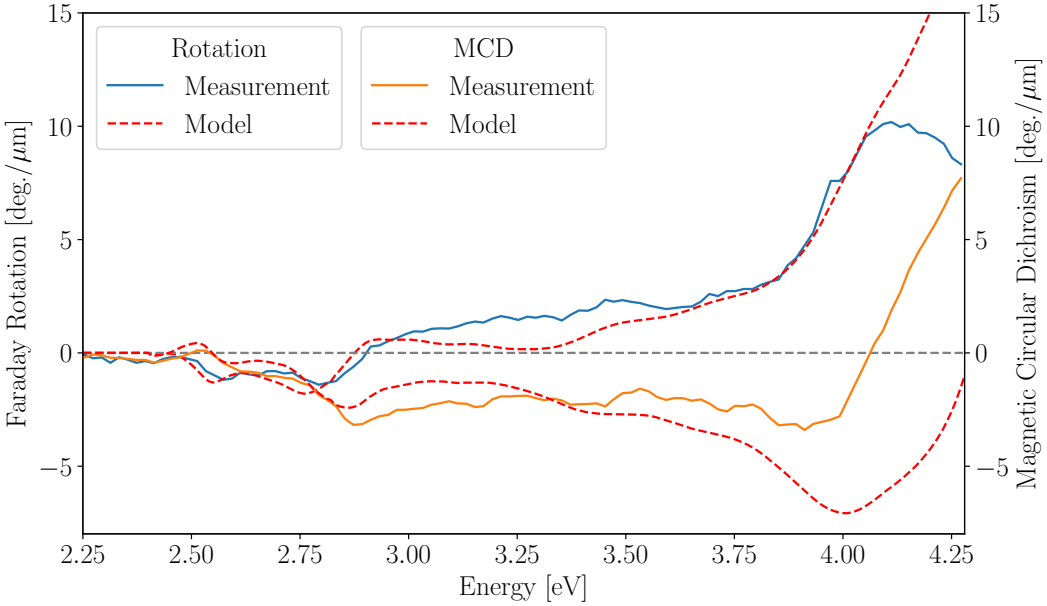

Figure 11.5: Room temperature spectral dependence of Faraday rotation and MCD of TbIG film on GGG (111) substrate compared with theoretical model using calculated permittivity tensor.

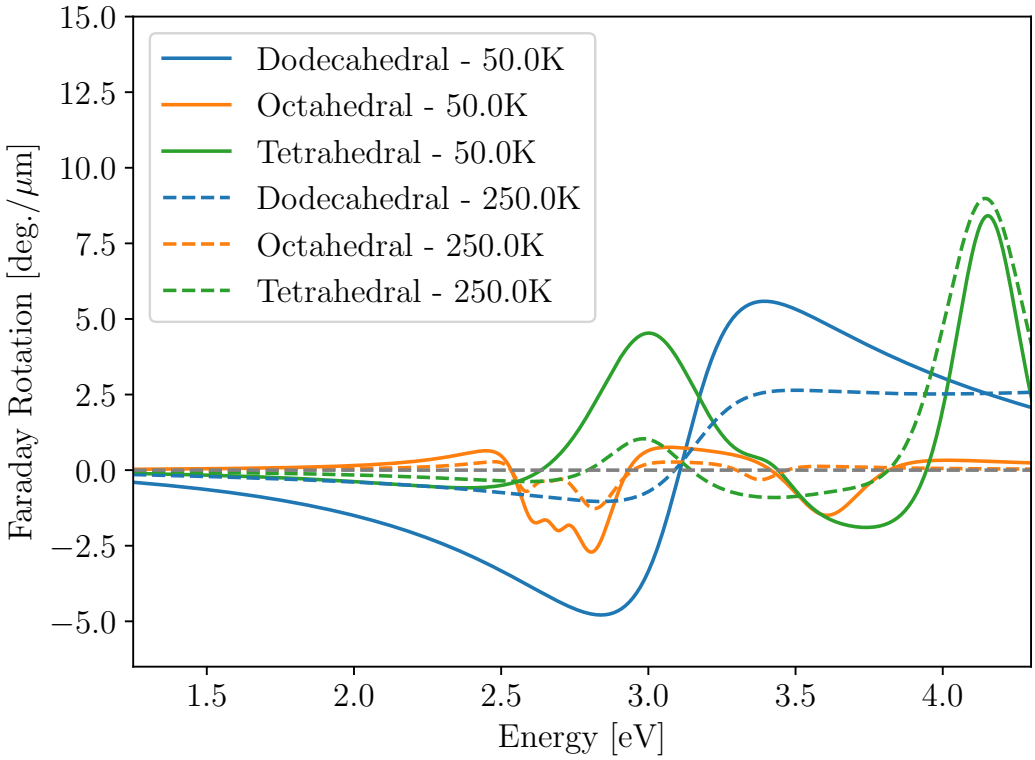

Figure 11.6: Spectral dependence of Faraday effect of individual magnetic sublattices of TbIG film on GGG (111) substrate for 50 K and 250 K.

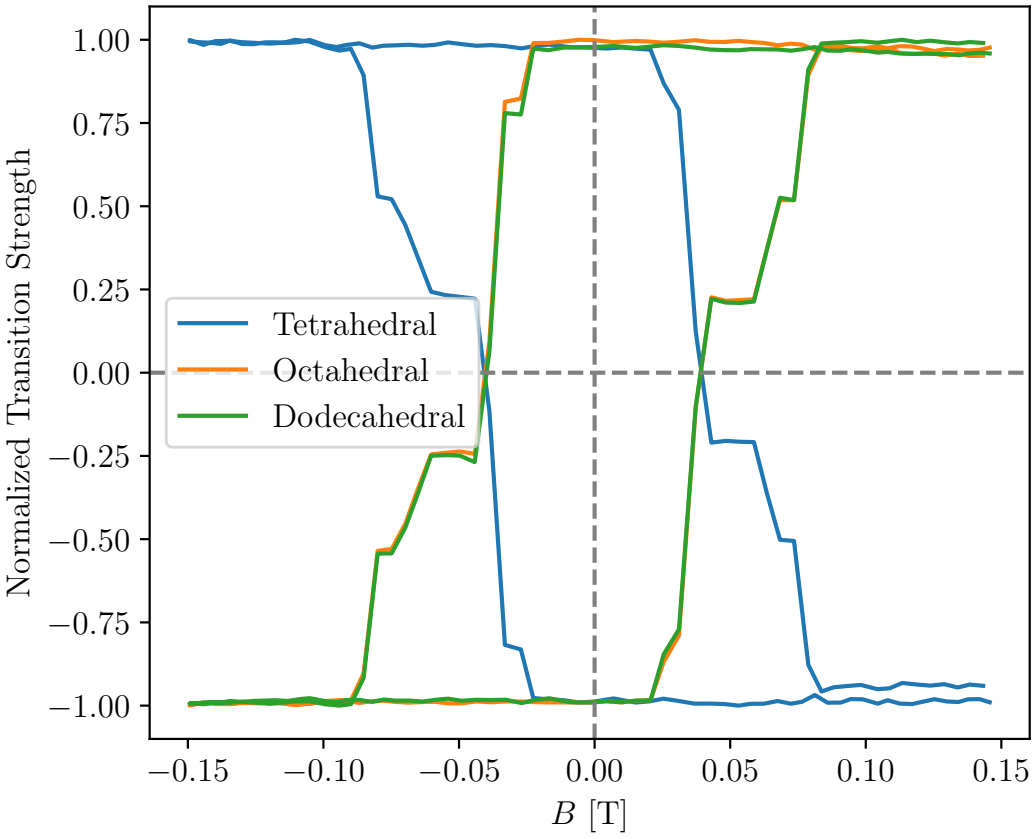

Figure 11.7: Normalized room temperature hysteresis loop of contributions of magnetic sublattices of TbIG film on GGG (111) substrate into Faraday effect.

Part V

Conclusions

In this thesis we studied various ferrimagnetic iron garnets. All the materials were prepared in the form of single, or polycrystalline thin films. The main attention was given to their structural and magnetic properties followed by analysis of optical and magneto-optical response.

$\mathbf{Bi}_x\mathbf{Y}_{3-x}\mathbf{Fe}_5\mathbf{O}_{12}$ on $\mathbf{Gd}_3\mathbf{Ga}_5\mathbf{O}_{12}$

At first, we focused on Bi:YIG films prepared by MOD. This technique allowed the fabrication of Bi:YIG films with up to full substitution of Bi. These samples exhibited high magneto-optical response (FR over 60 deg./μm) scaling with the Bi content. This proved MOD to be a significant candidate for integration of garnets into photonic devices, especially for its scalability and technological simplicity.

$\mathbf{Ce}_1\mathbf{Y}_2\mathbf{Fe}_5\mathbf{O}_{12}$ on $\mathbf{Gd}_3\mathbf{Ga}_5\mathbf{O}_{12}$

The study continued with samples of Ce:YIG films prepared by PLD on GGG substrates with different crystallographic orientations. The structural analysis did not reveal any presence of secondary phases and their magnetic properties were comparable to bulk crystals. Their optical and magneto-optical properties were studied in a broad spectral region from 0.7 to 6 eV. The measurement of optical transmission showed small, but non-zero difference between the films on different substrate orientations. This finding was confirmed by spectral dependencies of diagonal terms of permittivity tensor, ε_1, that were deduced from experimental data measured by spectroscopic ellipsometry. The spectra of Faraday and polar Kerr effects showed strong magneto-optical response in the near IR spectral region caused by intra-ionic transitions of Ce^{3+}. The magneto-optical effect in visible region was similarly to YIG originating from Fe^{3+} in tetrahedral and octahedral sites. The saturated Faraday rotation of -0.58 deg./μm at 0.8 eV (1550 nm) was exceptionally high and exceeded values reported for bulk crystals. The measurements of magneto-optical properties were combined with denoted spectral dependence of ε_1 to calculate off-diagonal elements of the permittivity tensor ε_2. The knowledge of the complete permittivity tensor is crucial for design and calculation of performance of devices using this material. Similar optical and magneto-optical properties were observed in case of ultra-thin (10 nm) films, that were prepared by the same deposition procedure. Lower thickness resulted in weaker tendency of films to form non-magnetic interfacial layer enhancing their properties, especially on GGG (100). Modeling of magneto-optical response with data obtained from thicker films showed, that thinner films contain lower concentration of Ce. The high Faraday rotation and the low optical absorption in the IR region gave the studied films high values of FoM in this part of spectra. The best value of FoM (943 deg./dB) was reached for Ce:YIG film on GGG (111) substrate. This confirmed its suitability for applications in magneto-optical isolators and other photonic devices.

$\mathbf{Ce}_x\mathbf{Y}_{3-x}\mathbf{Fe}_5\mathbf{O}_{12}$ on Si

The films for study of physical properties of Ce:YIG films with various Ce content on Si substrate with intermediate YIG seed layer were deposited using PLD.

The crucial element for formation of garnet structure was found to be low oxygen pressure during the deposition of Ce:YIG layer. Measurement of magnetic properties showed bulk like magnetization with decrease of M_S with increase of Ce content. Values of anisotropy fields suggested contribution of magnetoelastic anisotropy into the magnetic anisotropy; however, the magnetization easy-axis remained in-plane to the films surface. Measurement of magnetic hysteresis loops of Faraday rotation at 0.8 eV (1550 nm) demonstrated linear increase of saturated Faraday rotation with Ce content. Similar trend was observed on spectral dependencies of Faraday rotation measured in the near IR region. In visible region, optical properties of these films showed similar spectral dependence to the single crystal films. The near IR spectral region contains new features causing significantly higher optical absorption resulting in much smaller values of FoM. Even though the FoM was not sufficient for application in telecommunication, their high Faraday rotation makes them good candidates for photonic applications like holographic imaging, that are less sensitive to optical loss.

$\mathbf{Bi}_x\mathbf{Y}_{3-x}\mathbf{Fe}_5\mathbf{O}_{12}$ on Si

Due to the problematic growth of Ce:YIG on Si, deposition of Bi:YIG on this substrate was studied. The optimal deposition conditions for various Bi compositions were found by preparation of films on GGG (100) substrates. Magnetic properties revealed significant increase on coercivity field with increase of Bi content caused by introduction of significantly bigger atoms into the lattice. Magnetic hysteresis loops of Faraday rotation measures at 0.8 eV (1550 nm) confirmed the increase of magneto-optical response with Bi content previously observed at films deposited by MOD. Measurements of spectral dependencies of Faraday rotation showed significant difference in spectral shape in comparison to MOD films. These changes are caused by iron deficiency of samples deposited by PLD that was revealed by measurement of WDS. The shortage of iron causes different occupancy of tetrahedral and octahedral magnetic sublattices. The change of spectral shape of Faraday rotation causes enhancement of its magneto-optical response in the near IR region. It is due to further reaching transitions situated in visible region. Deposition on Si was performed using two crystallization techniques with different arrangement of seed layer. The top-bottom crystallization showed formation of secondary phases due to encapsulation of Bi in the structure that was solved by additional annealing of the film before the deposition of YIG on the top. Magneto-optical response determined by measurement of magnetic hysteresis loops of Faraday rotation showed comparable results for both crystallization techniques and followed the same trends with Bi content observed on singlecrystalline films. Optical properties of all Bi:YIG films acquired from spectroscopic ellipsometry showed excellent optical transmission in near IR region. The difference between samples on Si was found to be shift of the absorption edge. In the case of bottom-up crystallization, the edge is shifted towards higher energies. Therefore, these samples have better values of FoM over the ones prepared with top-down crystallization. The best achieved value of FoM 769 deg./dB significantly exceeds performance of Ce:YIG on Si.

Garnets with perpendicular magnetic anisotropy

The next study aimed for preparation of garnet films with PMA. For this purpose, TmIG, EuIG, and TbIG were chosen. These films prepared by PLD on GGG substrates showed excellent epitaxial quality. RSMs confirmed, that the films remain at thickness of 40 nm fully strained. The magnetic anisotropy was studied by VSM in combination with measurements of magnetic hysteresis loops of Faraday rotation. All samples exhibit at room temperature PMA. With the exception of EuIG on GGG (110) the films have in the direction of magnetization easy-axis square loops with very low coercivity fields of units of mT. Optical response of the samples was measured by spectroscopic ellipsometry and diagonal term of permittivity tensor, ε_1, was denoted using model containing Tauc-Lorentz oscillators. All materials showed similar characteristic spectral features originating from iron crystal field. The TbIG film exhibited shift of the absorption edge towards higher energies. Spectral dependence of Faraday effect of all samples was measured in broad spectral region ranging from 0.7 to 4.3 eV. There was no observable magneto-optical response below 2.4 eV. The upper limit of the measurements was given by significant optical absorption in UV region. The spectrum of TbIG had opposite sign of the effect compared to the other studied materials suggesting its state being at the room temperature above the compensation point. Specific transitions originating from RE elements were observed only in the case of TbIG laying around 3 eV. The main spectral features are coming from iron crystal field. The studied region of magneto-optical response was extended by measurement of spectra of polar MOKE. The differences observed in this case suggest influence of this RE element on occupancy of iron sublattices.

Anisotropy reorientation of $Ce_1Y_2Fe_5O_{12}$

The temperature dependencies of physical properties of Ce:YIG on GGG were studied in the range from 77 K to 300 K. Measurement of XRD scans in this temperature region revealed two types of behavior with their change at 170 K. The most significant was the change of the thermal expansion coefficient that was similar for the film and the substrate at low temperatures, but started to differ above 170 K. This caused significant change of opening angle γ above this point. Measurements of magnetic hysteresis loops of Faraday rotation revealed that this transition temperature is connected with magnetic anisotropy reorientation when magnetization easy-axis turned out-of-plane at the low temperatures. The decrease of temperature was further connected with increase of coercivity field and saturated Faraday rotation. The spectra of Faraday effect for 77 K and 300 K revealed significant increase of magneto-optical response near IR region due to paramagnetic character of Ce^{3+} inter-ionic transitions at these energies. Additional spectral feature was revealed at 1.9 eV originating in iron crystal field.

Magneto-optical behavior near the compensation temperature

The behavior of magneto-optical response near compensation temperature was studied on the sample of TbIG. The measurements of Faraday and polar Kerr rotation at cryogenic temperatures confirmed the paramagnetic character of transitions around 3 eV; however, the compensation temperature was found at 317.8 K,

80 K higher than expected from bulk values. The magneto-optical response exhibited different behavior around this temperature based on the magnetization history. This difference was explained by pinning of magnetic domain walls in the vicinity of the compensation temperature, where the film had nearly antiferromagnetic ordering. Usage of magneto-optical response for determination of the compensation temperature proved to be much more precise than conventional magnetometry due to its sensitivity to local magnetic moments on sublattices rather than net magnetization.

Modeling of magneto-optical spectra

The study concluded with demonstration of magneto-optical modeling of TbIG using microscopic model based on semiclassical approach. The starting model was build upon knowledge from similar garnet systems as well as modeling of optical response. The finalization was done on experimental measurements of spectra of Faraday effect. Data from different temperatures were used to better distinguish character of present transitions. The performance of the final model was shown at cryogenic temperatures as well as near the compensation temperature. The spectral coverage of the model was further extended using off-diagonal element of the permittivity tensor calculated from the measurement of polar MOKE and optical properties. The extended model was used for separation of contribution of individual magnetic sublattices into Faraday effect. Moreover, the ability of model to describe the changes of magnetization was demonstrated on modeling of magnetization reversal. The switching mechanism was found to be propagation of magnetic domain walls rather that tilting of magnetic sublattices.

Bibliography

[1] M. M. Waldrop. The chips are down for Moore's law. *Nature*, 530(7589):144–147, feb 2016.

[2] A. Fert. Nobel Lecture: Origin, development, and future of spintronics. *Reviews of Modern Physics*, 80:1517–1530, Dec 2008.

[3] J. Wunderlich, B.-G. Park, A. C. Irvine, L. P. Zarbo, E. Rozkotova, P. Nemec, V. Novak, J. Sinova, and T. Jungwirth. Spin Hall Effect Transistor. *Science*, 330(6012):1801–1804, dec 2010.

[4] C. Reig, S. Cardoso, and S. Mukhopadhyay. *Giant Magnetoresistance (GMR) Sensors*. Springer-Verlag GmbH, 2013.

[5] C. Yeh. *Applied Photonics*. Academic Press, 2012.

[6] C. Sun, M. T. Wade, Y. Lee, J. S. Orcutt, L. Alloatti, M. S. Georgas, A. S. Waterman, J. M. Shainline, R. R. Avizienis, S. Lin, B. R. Moss, R. Kumar, F. Pavanello, A. H. Atabaki, H. M. Cook, A. J. Ou, J. C. Leu, Y. Chen, K. Asanović, R. J. Ram, M. A. Popović, and V. M. Stojanović. Single-chip microprocessor that communicates directly using light. *Nature*, 528(7583):534–538, dec 2015.

[7] G. Berrettini, A. Simi, A. Malacarne, A. Bogoni, and L. Poti. Ultrafast integrable and reconfigurable XNOR, AND, NOR, and NOT photonic logic gate. *IEEE Photonics Technology Letters*, 18(8):917–919, apr 2006.

[8] Wikipedia contributors. Garnet — Wikipedia, the free encyclopedia, 2020. [Online; accessed 24-February-2020].

[9] J. D. Jackson. *Classical Electrodynamics*. John Wiley & Sons, 1962.

[10] J. A. Stratton. *Electromagnetic Theory (Pure & Applied Physics)*. McGraw-Hill College, 1941.

[11] B. Hecht. *Instructor's Manual for Optics, 5th Edition*. pearson, 2016.

[12] S. Strang. *Linear Algebra and Its Applications*. BROOKS COLE PUB CO, 2005.

[13] Š. Višňovský. Magneto-optical ellipsometry. *Czechoslovak Journal of Physics*, 36(5):625–650, may 1986.

[14] P. Yeh. Optics of anisotropic layered media: a new 4× 4 matrix algebra. *Surface Science*, 96(1-3):41–53, 1980.

[15] W. Borchardt-Ott. *Crystallography: An Introduction*. Springer, 2011.

[16] R. Silber, O. Stejskal, L. Beran, P. Cejpek, R. Antoš, T. Matalla-Wagner, J. Thien, O. Kuschel, J. Wollschläger, M. Veis, T. Kuschel, and J. Hamrle. Quadratic magnetooptic Kerr effect spectroscopy of Fe epitaxial films on MgO(001) substrates.

[17] D. M. Pozar. *Microwave Engineering*. John Wiley and Sons Ltd, 2011.

[18] B. Lax and K. J. Button. *Microwave Ferrites and Ferrimagnetics*. Literary Licensing, LLC, 2012.

[19] G. F. Dionne. *Magnetic Oxides*. Springer US, 2009.

[20] S. Wittekoek, T. J. A. Popma, J. M. Robertson, and P. F. Bongers. Magneto-optic spectra and the dielectric tensor elements of bismuth-substituted iron garnets at photon energies between 2.2-5.2 eV. *Physical Review B*, 12(7):2777–2788, oct 1975.

[21] F. Bertaut and F. Forrat. Structure des ferrites ferrimagnetiques des terres rares. *Comptes Rendus Hebdomadaires Des Seances De L Academie Des Sciences*, 242(3):382–384, 1956.

[22] G. F. Dionne. Determination of Magnetic Anisotropy and Porosity from the Approach to Saturation of Polycrystalline Ferrites. *Journal of Applied Physics*, 40(4):1839–1848, mar 1969.

[23] A. Thavendrarajah, M. Pardavi-Horvath, P. E. Wigen, and M. Gomi. Magnetic properties of sputtered $Bi_3Fe_5O_{12}$. *IEEE Transactions on Magnetics*, 25(5):4015–4017, sep 1989.

[24] F. Bertaut and R. Pauthenet. Crystalline structure and magnetic properties of ferrites having the general formula $5Fe_2O_3 \cdot 3M_2O_3$. *Proceedings of the IEE - Part B: Radio and Electronic Engineering*, 104(5S):261–264, 1957.

[25] R. Pauthenet. Magnetic properties of yttrium and rare earth iron garnets. *Ann. Phys.(Paris)*, 3:424–462, 1958.

[26] W. Zhu and R. W. Vest. Metallo-organic decomposition technology for PZT films in memory applications. *Journal of Materials Processing Technology*, 29(1-3):373–384, jan 1992.

[27] T. Ishibashi, A. Mizusawa, M. Nagai, S. Shimizu, K. Sato, N. Togashi, T. Mogi, M. Houchido, H. Sano, and K. Kuriyama. Characterization of epitaxial $(Y,Bi)_3(Fe,Ga)_5O_{12}$ thin films grown by metal-organic decomposition method. *Journal of Applied Physics*, 97(1):013516, jan 2005.

[28] B. Roas, L. Schultz, and G. Endres. Epitaxial growth of $YBa_2Cu_3O_{7-x}$ thin films by a laser evaporation process. *Applied Physics Letters*, 53(16):1557–1559, oct 1988.

[29] P. Grosseau, A. Bachiorrini, and B. Guilhot. Preparation of polycrystalline yttrium iron garnet ceramics. *Powder Technology*, 93(3):247–251, oct 1997.

[30] J. Li, B. Ramanujam, and R. W. Collins. Dual rotating compensator ellipsometry: Theory and simulations. *Thin Solid Films*, 519(9):2725–2729, feb 2011.

[31] R. M. A. Azzam. Mueller-matrix ellipsometry: a review. In *Polarization: Measurement, Analysis, and Remote Sensing*. SPIE, oct 1997.

[32] H. G. Tompkins and J. N. Hilfiker. *Spectroscopic Ellipsometry*. Momentum Press, 2015.

[33] M. Veis, L. Beran, M. Zahradnik, R. Antos, L. Straka, J. Kopecek, L. Fekete, and O. Heczko. Magneto-optical spectroscopy of ferromagnetic shape-memory Ni-Mn-Ga alloy. *Journal of Applied Physics*, 115(17):17A936, may 2014.

[34] L. Beran, P. Cejpek, M. Kulda, R. Antos, V. Holy, M. Veis, L. Straka, and O. Heczko. Optical and magneto-optical studies of martensitic transformation in Ni-Mn-Ga magnetic shape memory alloys. *Journal of Applied Physics*, 117(17):17A919, may 2015.

[35] C. O. Avci, E. Rosenberg, M. Baumgartner, L. Beran, A. Quindeau, P. Gambardella, C. A. Ross, and G. S. D. Beach. Fast switching and signature of efficient domain wall motion driven by spin-orbit torques in a perpendicular anisotropy magnetic insulator/Pt bilayer. *Applied Physics Letters*, 111(7):072406, aug 2017.

[36] E. R. Rosenberg, L. Beran, C. O. Avci, C. Zeledon, B. Song, C. Gonzalez-Fuentes, J. Mendil, P. Gambardella, M. Veis, C. Garcia, G. S. D. Beach, and C. A. Ross. Magnetism and spin transport in rare-earth-rich epitaxial terbium and europium iron garnet films. *Physical Review Materials*, 2(9), sep 2018.

[37] S. Crossley, A. Quindeau, A. G. Swartz, E. R. Rosenberg, L. Beran, C. O. Avci, Y. Hikita, C. A. Ross, and H. Y. Hwang. Ferromagnetic resonance of perpendicularly magnetized $Tm_3Fe_5O_{12}$/Pt heterostructures. *Applied Physics Letters*, 115(17):172402, oct 2019.

[38] T. Ishibashi, T. Kawata, T. H. Johansen, J. He, N. Harada, and K. Sato. Magneto-optical Indicator Garnet Films Grown by Metal-organic Decomposition Method. *Journal of the Magnetics Society of Japan*, 32(2_2):150–153, 2008.

[39] P. Hansen and J.-P. Krumme. Magnetic and magneto-optical properties of garnet films. *Thin Solid Films*, 114(1-2):69–107, apr 1984.

[40] M. Lang, M. Montazeri, M. C. Onbasli, X. Kou, Y. Fan, P. Upadhyaya, K. Yao, F. Liu, Y. Jiang, W. Jiang, K. L. Wong, G. Yu, J. Tang, T. Nie, L. He, R. N. Schwartz, Y. Wang, C. A. Ross, and K. L. Wang. Proximity Induced High-Temperature Magnetic Order in Topological Insulator - Ferrimagnetic Insulator Heterostructure. *Nano Letters*, 14(6):3459–3465, may 2014.

[41] M. C. Onbasli, T. Goto, X. Sun, N. Huynh, and C. A. Ross. Integration of bulk-quality thin film magneto-optical cerium-doped yttrium iron garnet on silicon nitride photonic substrates. *Optics Express*, 22(21):25183, oct 2014.

[42] S. Mino, A. Tate, T. Uno, T. Shintaku, and A. Shibukawa. Properties of Ce-Substituted Yttrium Iron Garnet Film Containing Indium Prepared

by RF-Sputtering. *Japanese Journal of Applied Physics*, 32(Part 2, No. 7B):L994–L996, jul 1993.

[43] B. Jiang, Z. Zhao, X. Xu, P. Song, X. Wang, J. Xu, and P. Deng. Spectral properties and charge transfer luminescence of Yb^{3+}:$Gd_3Ga_5O_{12}$ (Yb:GGG) crystal. *Journal of Crystal Growth*, 277(1-4):186–191, apr 2005.

[44] W. Wettling, B. Andlauer, P. Koidl, J. Schneider, and W. Tolksdorf. Optical absorption and Faraday rotation in yttrium iron garnet. *Physica Status Solidi (b)*, 59(1):63–70, sep 1973.

[45] S. Visnovsky, N. P. Thuy, J. Stepanek, V. Prosser, and R. Krishnan. Magnetooptical spectra of $Y_3Fe_5O_{12}$ and $Li_{0.5}Fe_{2.5}O_4$ between 2.0 and 5.8 eV. *Journal of Applied Physics*, 50(B11):7466, 1979.

[46] F. J. Kahn, P. S. Pershan, and J. P. Remeika. Ultraviolet Magneto-Optical Properties of Single-Crystal Orthoferrites, Garnets, and Other Ferric Oxide Compounds. *Physical Review*, 186(3):891–918, oct 1969.

[47] S. H. Wemple, S. L. Blank, J. A. Seman, and W. A. Biolsi. Optical properties of epitaxial iron garnet thin films. *Physical Review B*, 9(5):2134–2144, mar 1974.

[48] E. Jakubisova-Liskova, S. Visnovsky, H. Chang, and M. Wu. Optical spectroscopy of sputtered nanometer-thick yttrium iron garnet films. *Journal of Applied Physics*, 117(17):17B702, may 2015.

[49] M. Kucera, J. Bok, and K. Nitsch. Faraday rotation and MCD in Ce doped yig. *Solid State Communications*, 69(11):1117–1121, mar 1989.

[50] G. J. Diercks. Magneto-optical properties of $Y_{3-x-y}Ce_xLa_yFe_5O_{12}$. *IEEE transactions on magnetics*, 31(6):3328–3330, 1995.

[51] L. Bi, J. Hu, P. Jiang, D. H. Kim, G. F. Dionne, L. C. Kimerling, and C. A. Ross. On-chip optical isolation in monolithically integrated non-reciprocal optical resonators. *Nature Photonics*, 5(12):758–762, nov 2011.

[52] T. Goto, M. C. Onbaşlò, and C. A. Ross. Magneto-optical properties of cerium substituted yttrium iron garnet films with reduced thermal budget for monolithic photonic integrated circuits. *Optics Express*, 20(27):28507, dec 2012.

[53] B. Stadler, K. Vaccaro, P. Yip, J. Lorenzo, Yi-Qun Li, and M. Cherif. Integration of magneto-optical garnet films by metal-organic chemical vapor deposition. *IEEE Transactions on Magnetics*, 38(3):1564–1567, may 2002.

[54] Q. Yang, H. Zhang, Q. Wen, and Y. Liu. Effects of off-stoichiometry and density on the magnetic and magneto-optical properties of yttrium iron garnet films by magnetron sputtering method. *Journal of Applied Physics*, 108(7):073901, oct 2010.

[55] S. Sung, X. Qi, and B. J. H. Stadler. Integrating yttrium iron garnet onto nongarnet substrates with faster deposition rates and high reliability. *Applied Physics Letters*, 87(12):121111, sep 2005.

[56] Y. Zhang, C. T. Wang, X. Liang, B. Peng, H. P. Lu, P. H. Zhou, L. Zhang, J. X. Xie, L. J. Deng, M. Zahradnik, L. Beran, M. Kucera, M. Veis, C. A. Ross, and L. Bi. Enhanced magneto-optical effect in $Y_{1.5}Ce_{1.5}Fe_5O_{12}$ thin films deposited on silicon by pulsed laser deposition. *Journal of Alloys and Compounds*, 703:591–599, may 2017.

[57] M. Gomi, H. Furuyama, and M. Abe. Enhancement of Faraday Effect in Highly Ce-Substituted YIG Epitaxial Films by RF Sputtering. *Japanese Journal of Applied Physics*, 29(Part 2, No. 1):L99–L100, jan 1990.

[58] M. Gomi, K. Satoh, and M.Abe. Giant Faraday Rotation of Ce-Substituted YIG Films Epitaxially Grown by RF Sputtering. *Japanese Journal of Applied Physics*, 27(Part 2, No. 8):L1536–L1538, aug 1988.

[59] M. Gomi, H. Furuyama, and M. Abe. Strong magneto-optical enhancement in highly Ce-substituted iron garnet films prepared by sputtering. *Journal of Applied Physics*, 70(11):7065–7067, dec 1991.

[60] Y. Xu, J. H. Yang, and G. Zhang. A theoretical investigation on the strong magneto-optical enhancement in Ce-substituted yttrium iron garnet. *Journal of Physics: Condensed Matter*, 5(47):8927–8934, nov 1993.

[61] M. Veis, E. Lišková, R. Antoš, Š. Višňovský, N. Kumar, D. S. Misra, N. Venkataramani, S. Prasad, and R. Krishnan. Polar and longitudinal magneto-optical spectroscopy of bismuth substituted yttrium iron garnet films grown by pulsed laser deposition. *Thin Solid Films*, 519(22):8041–8046, sep 2011.

[62] T. Kim and M. Shima. Reduced magnetization in magnetic oxide nanoparticles. *Journal of Applied Physics*, 101(9):09M516, may 2007.

[63] S. Higuchi, Y. Furukawa, S. Takekawa, O. Kamada, and K. Kitamura. Magneto-Optical Properties of Cerium-Substituted Yttrium Iron Garnet Single Crystals Grown by Traveling Solvent Floating Zone Method. *Japanese Journal of Applied Physics*, 38(Part 1, No. 7A):4122–4126, jul 1999.

[64] T. Goto, Y. Eto, K. Kobayashi, Y. Haga, M. Inoue, and C. A. Ross. Vacuum annealed cerium-substituted yttrium iron garnet films on nongarnet substrates for integrated optical circuits. *Journal of Applied Physics*, 113(17):17A939, may 2013.

[65] T. Shintaku, A. Tate, and S. Mino. Ce-substituted yttrium iron garnet films prepared on $Gd_3Sc_2Ga_3O_{12}$ garnet substrates by sputter epitaxy. *Applied Physics Letters*, 71(12):1640–1642, sep 1997.

[66] L. Bi, J. Hu, G. F. Dionne, L. Kimerling, and C. A. Ross. Monolithic integration of chalcogenide glass/iron garnet waveguides and resonators for on-chip nonreciprocal photonic devices. In Jean E. Broquin and Gualtiero Nunzi

Conti, editors, *Integrated Optics: Devices, Materials, and Technologies XV*. SPIE, feb 2011.

[67] T. Shintaku. Integrated optical isolator based on efficient nonreciprocal radiation mode conversion. *Applied Physics Letters*, 73(14):1946–1948, oct 1998.

[68] T. Goto, M. C. Onbasli, D. H. Kim, V. Singh, M. Inoue, L. C. Kimerling, and C. A. Ross. A nonreciprocal racetrack resonator based on vacuum-annealed magnetooptical cerium-substituted yttrium iron garnet. *Optics Express*, 22(16):19047, jul 2014.

[69] X. Liang, J. Xie, L. Deng, and L. Bi. First principles calculation on the magnetic, optical properties and oxygen vacancy effect of $Ce_xY_{3-x}Fe_5O_{12}$. *Applied Physics Letters*, 106(5):052401, feb 2015.

[70] H. Béa, M. Bibes, S. Fusil, K. Bouzehouane, E. Jacquet, K. Rode, P. Bencok, and A. Barthélémy. Investigation on the origin of the magnetic moment of $BiFeO_3$ thin films by advanced x-ray characterizations. *Physical Review B*, 74(2), jul 2006.

[71] G. Scott and D. Lacklison. Magnetooptic properties and applications of bismuth substituted iron garnets. *IEEE Transactions on Magnetics*, 12(4):292–311, jul 1976.

[72] M. Chern and J. Liaw. Study of $Bi_xY_{3-x}Fe_5O_{12}$ Thin Films Grown by Pulsed Laser Deposition. *Japanese Journal of Applied Physics*, 36(Part 1, No. 3A):1049–1053, mar 1997.

[73] L. Bi, J. Hu, P. Jiang, H. Kim, D. Kim, M. Onbasli, G. Dionne, and C. A. Ross. Magneto-Optical Thin Films for On-Chip Monolithic Integration of Non-Reciprocal Photonic Devices. *Materials*, 6(11):5094–5117, nov 2013.

[74] M. Chern, F. Lo, D. Liu, K. Yang, and J. Liaw. Red Shift of Faraday Rotation in Thin Films of Completely Bismuth-Substituted Iron Garnet $Bi_3Fe_5O_{12}$. *Japanese Journal of Applied Physics*, 38(Part 1, No. 12A):6687–6689, dec 1999.

[75] M. Inoue, R. Fujikawa, A. Baryshev, A. Khanikaev, P. B. Lim, H. Uchida, O. Aktsipetrov, A. Fedyanin, T. Murzina, and A. Granovsky. Magnetophotonic crystals. *Journal of Physics D: Applied Physics*, 39(8):R151–R161, mar 2006.

[76] M. C. Onbasli, L. Beran, M. Zahradník, M. Kučera, R. Antoš, J. Mistrík, G. F. Dionne, M. Veis, and C. A. Ross. Optical and magneto-optical behavior of Cerium Yttrium Iron Garnet thin films at wavelengths of 200–1770 nm. *Scientific Reports*, 6(1), mar 2016.

[77] P. Pintus, F. Di Pasquale, and J. E. Bowers. Integrated TE and TM optical circulators on ultra-low-loss silicon nitride platform. *Optics Express*, 21(4):5041, feb 2013.

[78] C. Chappert, A. Fert, and F. Nguyen Van Dau. The emergence of spin electronics in data storage. In *Nanoscience and Technology*, pages 147–157. Co-Published with Macmillan Publishers Ltd, UK, aug 2009.

[79] L. Berger. Emission of spin waves by a magnetic multilayer traversed by a current. *Physical Review B*, 54(13):9353–9358, oct 1996.

[80] A. Quindeau, C. O. Avci, W. Liu, C. Sun, M. Mann, A. S. Tang, M. C. Onbasli, D. Bono, P. M. Voyles, Y. Xu, J. Robinson, G. S. D. Beach, and C. A. Ross. $Tm_3Fe_5O_{12}$/Pt Heterostructures with Perpendicular Magnetic Anisotropy for Spintronic Applications. *Advanced Electronic Materials*, 3(1):1600376, dec 2016.

[81] J. W. Weber, T. A. R. Hansen, M. C. M. van de Sanden, and R. Engeln. B-spline parametrization of the dielectric function applied to spectroscopic ellipsometry on amorphous carbon. *Journal of Applied Physics*, 106(12):123503, dec 2009.

[82] J. Ostoréro, M. Escorne, J. Gouzerh, and H. Le Gall. Magnetooptical Properties of Ce-Doped YIG Single Crystals. *Le Journal de Physique IV*, 07(C1):C1–719–C1–720, mar 1997.

[83] T. Mao and J. Chen. Influence of the addition of CeO_2 on the microstructure and the magnetic properties of yttrium iron garnet ceramic. *Journal of Magnetism and Magnetic Materials*, 302(1):74–81, jul 2006.

[84] R. L. Comstock and J. J. Raymond. Magnetostriction of Ytterbium and Cerium in YIG. *Journal of Applied Physics*, 38(9):3737–3739, aug 1967.

[85] D. L. Wood and J. P. Remeika. Effect of Impurities on the Optical Properties of Yttrium Iron Garnet. *Journal of Applied Physics*, 38(3):1038–1045, mar 1967.

[86] K. Ganzhorn, J. Barker, R. Schlitz, B. A. Piot, K. Ollefs, F. Guillou, F. Wilhelm, A. Rogalev, M. Opel, M. Althammer, S. Geprägs, H. Huebl, R. Gross, G. E. W. Bauer, and S. T. B. Goennenwein. Spin Hall magnetoresistance in a canted ferrimagnet. *Physical Review B*, 94(9), sep 2016.

[87] J. Finley and L. Liu. Spin-Orbit-Torque Efficiency in Compensated Ferrimagnetic Cobalt-Terbium Alloys. *Physical Review Applied*, 6(5), nov 2016.

[88] M. Deb, E. Popova, A. Fouchet, and N. Keller. Magneto-optical Faraday spectroscopy of completely bismuth-substituted $Bi_3Fe_5O_{12}$ garnet thin films. *Journal of Physics D: Applied Physics*, 45(45):455001, oct 2012.

List of Figures

List of Tables

Acronyms

AFM Atomic force microscopy. 62, 63

Bi:YIG bismuth doped yittrium iron garnet. 55–57, 76–82, 94, 108, 109, 121, 124

Ce:YIG cerium doped yittrium iron garnet. 57–68, 70–72, 74, 75, 79, 81, 88, 91–95, 108–110, 121–123, 125, 126

EuIG europium iron garnet ($Eu_3Fe_5O_{12}$). 83–90, 110, 125

FoM Figure of Merit. 45, 54, 69, 71, 75, 81, 108, 109, 123, 128

FR Farday rotation. 61, 75, 93, 108, 124

FTIR Fourier-transform infrared spectroscopy. 69

GGG gadolinium galium garnet ($Gd_3Ga_5O_{12}$). 55–71, 76–97, 99, 101, 102, 104–106, 108–110, 121–128

HRXRD high resolution X-ray diffraction. 77, 84, 85, 124, 125

IR infrared. 9, 56, 60, 63, 68–70, 75, 78, 79, 81, 90, 93, 95, 108–110, 122–124, 126

MBE molecular beam epitaxy. 36, 37

MCB magnetic circular birefringence. 25

MCD magnetic circular dichroism. 45, 56, 63, 66, 88, 89, 93, 95, 101, 102, 105, 121–123, 125–127

MLD magnetic linear dichroism. 25

MOD metallo-organic decomposition. 35, 36, 55, 56, 78, 108, 109

MOKE magneto-optical Kerr effect. 55, 56, 62, 63, 66, 68, 69, 86, 89, 95, 97, 98, 100–102, 110, 111, 121, 123

PLD pulsed laser deposition. 36–39, 56, 57, 71, 78, 108–110, 120

PMA perpendicular magnetic anisotropy. 24, 83, 86, 87, 90, 110, 125

RE rare-earth. 7, 35, 85, 88–90, 110

RF radio frequency. 74

RSM reciprocal space map. 42, 85, 86, 91, 110, 120, 125

RTA rapid thermal annealing. 72, 80, 81, 124

TbIG terbium iron garnet ($Tb_3Fe_5O_{12}$). 83–90, 94, 96, 97, 99–106, 110, 111, 125–128

TmIG thulium iron garnet ($Tm_3Fe_5O_{12}$). 83, 85–90, 110, 125

UV ultraviolet. 9, 37, 46, 51, 101–103, 110

VSM vibrating sample magnetometer. 43, 65, 78, 85, 98, 110, 120

WDS wavelength dispersive spectroscopy. 76, 91, 109

XPS X-ray photoelectron spectroscopy. 61, 73, 85

XRD X-ray diffraction. 7, 39, 41, 57, 58, 65, 72, 74, 80, 85, 92, 110, 121, 123, 124

XRR X-ray reflectivity. 57, 83, 91

YIG yttrium iron garnet ($Y_3Fe_5O_{12}$). 6, 7, 34, 35, 37–40, 54–56, 60–62, 71–75, 79, 80, 88, 90, 93, 100, 101, 108, 109, 120, 123, 124, 128

List of Publications

[1] T. Fakhrul, S. Tazlaru, L. Beran, Y. Zhang, M. Veis, and C. A. Ross. Magneto-optical Bi:YIG films with high figure of merit for nonreciprocal photonics. *Advanced Optical Materials*, page 1900056, apr 2019.

[2] K. K. Tikuišis, L. Beran, P. Cejpek, K. Uhlířová, J. Hamrle, M. Vaňatka, M. Urbánek, and M. Veis. Optical and magneto-optical properties of permalloy thin films in 0.7–6.4 eV photon energy range. *Materials & Design*, 114:31–39, jan 2017.

[3] E. Lage, L. Beran, A. U. Quindeau, L. Ohnoutek, M. Kucera, R. Antos, S. R. Sani, G. F. Dionne, M. Veis, and C. A. Ross. Temperature-dependent faraday rotation and magnetization reorientation in cerium-substituted yttrium iron garnet thin films. *APL Materials*, 5(3):036104, mar 2017.

[4] M. C. Onbasli, L. Beran, M. Zahradník, M. Kučera, R. Antoš, J. Mistrík, G. F. Dionne, M. Veis, and C. A. Ross. Optical and magneto-optical behavior of cerium yttrium iron garnet thin films at wavelengths of 200–1770 nm. *Scientific Reports*, 6(1), mar 2016.

[5] E. Jesenská, T. Ishibashi, L. Beran, M. Pavelka, J. Hamrle, R. Antoš, J. Zázvorka, and M. Veis. Optical and magneto-optical properties of $Gd_xFe_{(100-x)}$ thin films close to the compensation point. *Scientific Reports*, 9(1), nov 2019.

[6] Y. Zhang, C.T. Wang, X. Liang, B. Peng, H.P. Lu, P.H. Zhou, L. Zhang, J.X. Xie, L.J. Deng, M. Zahradnik, L. Beran, M. Kucera, M. Veis, C.A. Ross, and L. Bi. Enhanced magneto-optical effect in $Y_{1.5}Ce_{1.5}Fe_5O_{12}$ thin films deposited on silicon by pulsed laser deposition. *Journal of Alloys and Compounds*, 703:591–599, may 2017.

[7] R. Silber, O. Stejskal, L. Beran, P. Cejpek, R. Antoš, T. Matalla-Wagner, J. Thien, O. Kuschel, J. Wollschläger, M. Veis, T. Kuschel, and J. Hamrle. Quadratic magneto-optic Kerr effect spectroscopy of Fe epitaxial films on MgO(001) substrates. *Physical Review B*, 100(6), aug 2019.

[8] M. Zahradník, T. Maroutian, M. Zelený, L. Horák, G. Kurij, T. Maleček, L. Beran, Š. Višňovský, G. Agnus, P. Lecoeur, and M. Veis. Electronic structure of $La_{2/3}Sr_{1/3}MnO_3$: Interplay of oxygen octahedra rotations and epitaxial strain. *Physical Review B*, 99(19), may 2019.

[9] J. Zázvorka, J. Franc, L. Beran, P. Moravec, J. Pekárek, and M. Veis. Dynamics of native oxide growth on CdTe and CdZnTe X-ray and gamma-ray detectors. *Science and Technology of Advanced Materials*, 17(1):792–798, nov 2016.

[10] C. O. Avci, E. Rosenberg, M. Baumgartner, L. Beran, A. Quindeau, P. Gambardella, C. A. Ross, and G. S. D. Beach. Fast switching and signature

of efficient domain wall motion driven by spin-orbit torques in a perpendicular anisotropy magnetic insulator/Pt bilayer. *Applied Physics Letters*, 111(7):072406, aug 2017.

[11] S. Crossley, A. Quindeau, A. G. Swartz, E. R. Rosenberg, L. Beran, C. O. Avci, Y. Hikita, C. A. Ross, and H. Y. Hwang. Ferromagnetic resonance of perpendicularly magnetized $Tm_3Fe_5O_{12}$/Pt heterostructures. *Applied Physics Letters*, 115(17):172402, oct 2019.

[12] E. R. Rosenberg, L. Beran, C. O. Avci, C. Zeledon, B. Song, C. Gonzalez-Fuentes, J. Mendil, P. Gambardella, M. Veis, C. Garcia, G. S. D. Beach, and C. A. Ross. Magnetism and spin transport in rare-earth-rich epitaxial terbium and europium iron garnet films. *Physical Review Materials*, 2(9), sep 2018.

[13] E. J., T. Hashinaka, T. Ishibashi, L. Beran, J. Dušek, R. Antoš, K. Kuga, K. Aoshima, K. Machida, H. Kinjo, and M. Veis. Optical and magneto-optical properties of $Gd_{22}Fe_{78}$ thin films in the Photon Energy Range from 1.5 to 5.5 eV. *Materials*, 9(1):23, jan 2016.

[14] D. Král, L. Beran, M. Zelený, J. Zemen, R. Antoš, J. Hamrle, J. Zázvorka, M. Rameš, K. Onderková, O. Heczko, and M. Veis. Magnetic and magneto-optical properties of $Fe_{75-x}Mn_{25}Ga_x$ Heusler-like compounds. *Materials*, 13(3):703, feb 2020.

[15] E. Jesenska, T. Yoshida, K. Shinozaki, T. Ishibashi, L. Beran, M. Zahradnik, R. Antos, M. Kučera, and M. Veis. Optical and magneto-optical properties of Bi substituted yttrium iron garnets prepared by metal organic decomposition. *Optical Materials Express*, 6(6):1986, may 2016.

[16] L. Beran, P. Cejpek, M. Kulda, R. Antos, V. Holy, M. Veis, L. Straka, and O. Heczko. Optical and magneto-optical studies of martensitic transformation in Ni-Mn-Ga magnetic shape memory alloys. *Journal of Applied Physics*, 117(17):17A919, may 2015.

[17] M. Veis, L. Beran, M. Zahradnik, R. Antos, L. Straka, J. Kopecek, L. Fekete, and O. Heczko. Magneto-optical spectroscopy of ferromagnetic shape-memory Ni-Mn-Ga alloy. *Journal of Applied Physics*, 115(17):17A936, may 2014.

[18] M. Veis, L. Beran, R. Antos, D. Legut, J. Hamrle, J. Pistora, Ch. Sterwerf, M. Meinert, J.-M. Schmalhorst, T. Kuschel, and G. Reiss. Magneto-optical spectroscopy of Co_2FeSi heusler compound. *Journal of Applied Physics*, 115(17):17A927, may 2014.

[19] M. Veis, M. Zahradnik, L. Ohnoutek, L. Beran, M. Kucera, X. Y. Sun, C. Zhang, N. M. Aimon, T. Goto, M. C. Onbasli, D. H. Kim, H. K. Choi, and C. A. Ross. Magneto-optical studies of $SrGa_{0.7}Co_{0.3}O_{3-\delta}$ perovskite thin films with embedded cobalt nanoparticles. *Journal of Applied Physics*, 117(17):17A746, may 2015.

[20] M. Rejhon, V. Dedic, L. Beran, U. N. Roy, J. Franc, and R. B. James. Investigation of deep levels in CdZnTeSe crystal and their effect on the internal electric field of CdZnTeSe gamma-ray detector. *IEEE Transactions on Nuclear Science*, 66(8):1952–1958, aug 2019.